ROMA TRE
UNIVERSITÀ DEGLI STUDI

DOTTORATO DI RICERCA IN
INGEGNERIA CIVILE

XXXI
CICLO DEL CORSO DI DOTTORATO

Titolo della tesi

Smart materials as energy transducers

Dottorando:

Dr. Michele Curatolo

Docente Guida:

Dr. Pietro Prestininzi

Prof. Luciano Teresi

Coordinatore:

Prof. Gianmarco De Felice

Collana delle tesi di Dottorato di Ricerca
In Ingegneria Civile
Università degli Studi Roma Tre
Tesi n°75

"I would like to thank my Ph.D. advisors: Dr. P. Prestininzi and Prof. L. Teresi, who guided and helped me during these three years of studies. For what regards the electrical part in the piezoelectric materials I would like to thank Ing. Mario La Rosa who also helped me to design the experimental setup for the energy harvesting in a fluid flow. I would like to thank Prof. D. P. Holmes for his guidance and for his hospitality during my visiting period at Boston University. Finally, I would like to thank Prof. P. Nardinocchi for her help and advices on the hydrogel osmotic pumps and on the de-hydration of the hydrogel unit cell."

Michele Curatolo

Abstract

In this thesis two types of smart materials are investigated: piezoelectric materials and hydrogels. These materials have the property of transforming a specific energy into another.

In particular, piezoelectric materials are capable of generating an electric potential, hence an electrical power, when strained, while hydrogels are capable of large deformations after the absorption of a solvent. In the case of piezoelectric materials the electrical power can be harvested through a resistive load which has to be accurately chosen to maximize the efficiency of the device. A specific application of such materials is the energy harvesting in a fluid-solid interaction. Indeed, wind and water currents provide free kinetic energy which can be converted using piezoelectric sheets immersed in fluid flows through. This problem involves several physics which are strongly coupled. In this thesis, a specific configuration of a bilayer structure composed of a piezoelectric sheet is investigated both experimentally and numerically. Moreover, some modeling issues of piezoelectric materials and the optimal load resistance are also discussed.

On the other hand, hydrogels are material able to transform a chemical energy into an elastic energy. For this reason, they can be used as actuators which autonomously respond to environment changes. In this thesis, the shape control of hydrogel materials is investigated numerically and analytically. Moreover, since in general the response of hydrogel is slow, two high power mechanisms are described with an experiment and through some numerical simulations. Finally, the problem of residual strains due to the change of chemical conditions in the environment are tackled by means of a theoretical model. A list of submitted and published papers and proceedings included in this thesis are listed in the final chapter.

Contents

List of Figures

List of Tables

List of Abbreviations

PZT	Lead zirconate titanate
FSI	Fluid-structure interaction
PIV	Particle image velocimetry
PVS	Polyvinyl siloxane

Physical Constants

Universal gas constant	$\mathcal{R} = 8.314\,\mathrm{J\,mol^{-1}\,K^{-1}}$
Vacuum permittivity	$k_o = 8.854 \cdot 10^{-12}\ \mathrm{s^4 \cdot A^2 \cdot m^{-3} \cdot kg^{-1}}$

List of Symbols

$\mathcal{B}$	reference configuration of the piezoelectric or structural body	
$\mathcal{T}$	time interval	
$\mathbf{X}$	material point	
t	time	
L	length of the piezoelectric and structural solid	m
W	width of the piezoelectric and structural solid	m
h_p	thickness of the piezoelectric solid	m
$\mathbf{u}$	displacement field of piezoelectric and structural solids	m
$\mathbf{F}$	deformation gradient of piezoelectric and structural solids	
$\mathbf{S}$	reference stress of piezoelectric and structural solids	Pa
$\mathbb{C}$	stiffness tensor of piezoelectric solid	Pa
$\mathbf{E}$	nonlinear strain measure of piezoelectric and structural solids	
$\mathbf{e}$	piezoelectric coupling tensor	$\mathrm{C{\cdot}m^{-1}}$
k_o	vacuum permittivity	
$\mathbf{k}$	piezoelectric relative permittivity tensor	
$\mathbf{E}_{el}$	piezoelectric electric vector field	$\mathrm{V{\cdot}m^{-1}}$
V	piezoelectric electric potential	V
ρ	solid mass density	$\mathrm{kg{\cdot}m^{-3}}$
ρ_p	piezoelectric mass density	$\mathrm{kg{\cdot}m^{-3}}$
ρ_s	substructure mass density	$\mathrm{kg{\cdot}m^{-3}}$
$\mathbf{D}$	electric displacement in the piezoelectric solid	$\mathrm{C{\cdot}m^{-1}}$
$\mathbf{n}$	reference unit normal at the boundary	
ρ_v	free electrical charge	
$\mathbf{F}_e$	external applied force per unit area	Pa
R	electrical load resistance	Ohm
P	electrical power harvested on external load resistance	W
$\bar{P}$	average electrical power harvested on external load resistance	W
A	external force amplitude	$\mathrm{Pa{\cdot}m^{-2}}$
ω	external force pulsation	$\mathrm{rad{\cdot}s^{-1}}$
h_s	thickness of the structural solid	m
H	total thickness of the solid	m
Y_s	Young's modulus of the substructure layer	Pa
ν_s	Poisson ratio of the substructure layer	
τ	non-dimensional time of simulation in the bimorph solid	
f	frequency of the external force applied on the bimorph solid	$\mathrm{s^{-1}}$
ρ_{tip}	tip mass per unit area in the bimorph solid	$\mathrm{kg{\cdot}\ m^{-2}}$
ρ_{el}	electrical load resistance per unit width in the bimorph solid	$\mathrm{Ohm{\cdot}\ m^{-1}}$
L_f	length of the channel in FSI simulations	m
H_f	width of the channel in FSI simulations	m
L_s	length of the structural solid in FSI simulations	m
L_p	width of the piezoelectric solid in FSI simulations	m
D	diameter of the fixed constraint in FSI simulations	m

Ω	computational domain in FSI simulations	
Ω_m	mesh domain in FSI simulations	
Ω_s	computational domain for the uniin FSI simulations	
Ω_{sp}	computational domain for the piezoelectric solid in FSI simulations	
Ω_{ss}	computational domain for the structural solid in FSI simulations	
Ω_{mo}	reference mesh domain in FSI simulations	
$\mathbf{v}_f$	fluid velocity field in FSI simulations	$\mathrm{m{\cdot}s^{-1}}$
p_f	fluid pressure field in FSI simulations	Pa
Γ	fluid stress tensor in FSI simulations	Pa
$\mathbf{T}$	solid actual (Cauchy) stress tensor in FSI simulations	Pa
ω_f	fluid vorticity field in FSI simulations	Pa
μ_f	dynamic fluid viscosity in FSI simulations	Pa·s
ρ_f	fluid mass density in FSI simulations	$\mathrm{kg{\cdot}m^{-3}}$
U	inlet fluid velocity in FSI simulations	$\mathrm{m{\cdot}s^{-1}}$
τ_c	characteristic time in FSI simulations	m
$\mathcal{B}_d$	reference dry configuration of the hydrogel	
X_d	material point of the hydrogel	
$\mathbf{u}_d$	displacement field of the hydrogel	m
c_d	solvent concentration in the hydrogel	$\mathrm{mol{\cdot}m^{-3}}$
Ω	molar volume of the solvent	$\mathrm{m^3{\cdot}mol^{-1}}$
J_d	volume deformation of the hydrogel	
ψ_r	relaxed free density energy of the hydrogel	$\mathrm{J{\cdot}m^{-3}}$
ψ_e	elastic free density energy of the hydrogel	$\mathrm{J{\cdot}m^{-3}}$
ψ_m	mixing free density energy of the hydrogel	$\mathrm{J{\cdot}m^{-3}}$
$\mathbf{S}_d$	reference stress in the hydrogel	Pa
μ	chemical potential in the hydrogel	$\mathrm{J{\cdot}mol^{-1}}$
G_d	elastic shear modulus of the hydrogel	Pa
$\mathcal{R}$	universal gas constant	$\mathrm{J{\cdot}mol^{-1}K^{-1}}$
T	temperature of the hydrogel	K
χ	dis-affinity between polymer and solvent	
$\mathbf{T}$	actual stress in the hydrogel	Pa
p	pressure reaction to the volumetric constraint	Pa
$\mathbf{h}_d$	reference solvent flux	$\mathrm{mol{\cdot}s^{-1}m^{-1}J^{-1}}$
$\mathbf{M}$	mobility tensor of the hydrogel	$\mathrm{mol^2{\cdot}m^{-2}s^{-1}}$
$\mathbf{D}$	diffusivity of the hydrogel	$\mathrm{mol^2{\cdot}m^{-2}s^{-1}}$
μ_{ext}	chemical potential of the bath	$\mathrm{J{\cdot}mol^{-1}}$
μ_e	chemical potential of the bath	$\mathrm{J{\cdot}mol^{-1}}$
λ_o	free swollen stretch	
J_o	free swollen volume deformation	
β	ratio between thickness of layers in a bilayer hydrogel	
α	ratio between elastic shear moduli of layers in a bilayer hydrogel	
Λ_o	swelling induced stretch in a bilayer hydrogel beam	
k	swelling induced curvature in a bilayer hydrogel beam	$\mathrm{m^{-1}}$
F	resultant force in the bilayer hydrogel beam	N
M	moment in the bilayer hydrogel beam	N·m
$\mathbf{a}$	first fundamental form	
$\mathbf{b}$	second fundamental form	
$\bar{\mathbf{a}}$	natural first fundamental form	
$\bar{\mathbf{b}}$	natural second fundamental form	
$\bar{\mathcal{U}}$	non dimensional energy density for non-Euclidean plates	
K	Gaussian curbature	$\mathrm{m^{-2}}$

$\mathcal{C}_d$	reference dry configuration of the cavity in the hydrogel	
p_e	external pressure acting on the hydrogel	Pa
p_i	inner pressure acting on the hydrogel cavity walls	Pa
v_c	cavity volume of the hydrogel	m^3
v_w	water volume in the hydrogel cavity	m^3
$\mathcal{E}$	total potential energy of a sphere with a cavity	J
$\mathbf{F}_g$	relaxed stance or distortion	
$\mathbf{F}_e$	elastic deformation	
J_g	growth volume deformation	
J_e	elastic volume deformation	
$\mathcal{P}_i$	inner working	J
$\mathcal{P}_e$	outer working	J
$\mathbb{C}$	inner remodeling actions	Pa
$\mathbb{B}$	outer remodelling action	Pa
$\mathbb{E}$	Eshelby tensor	Pa
$\mathbb{E}_{mech}$	mechanical part of Eshelby tensor	Pa
$\mathbb{E}_{chem}$	chemical part of Eshelby tensor	Pa

Chapter 1

Introduction

Smart materials are artificial materials that are able to passively and actively respond to external stimuli such as temperature, humidity, stress and much more. For this reason, they are optimized to work as energy transducers which convert one form of energy into another. The transformation of energy is a relevant issue for technological advance. Nowadays, there exist several types of transducers: photoelectric, electromagnetic, electromechanical, chemomechanical and much more. Here, we will focus on two transducers which may be regarded as electromechanical and chemomechanical transducers.

In this thesis, the electromechanical transducer is assumed to be made of piezoelectric material which is a material that develops an electrical potential if strained or develops a strain when an electrical potential is imposed [1]. The applications of such material can be different from simple actuators to sensors. In particular, we will focus on a more novel application of such material which is the energy harvesting on an electrical passive load resistance. Indeed, energy harvesting using piezoelectric materials has been deeply studied over the last decade [1–3]. This technology provides extra sources of electric power which can be used to recharge electronic devices with a limited battery duration or to power other devices. The concept has ecological implications in reducing the chemical waste produced by replacing batteries and monetary gains by reducing maintenance costs. For this reason and not only, in the last years the area of energy harvesting has attracted academic and industry. A piezoelectric sheet generates very low power due to external actions; the main idea is to use such materials in arrays on 2D or 3D arrangements depending on the application [4–6] (see Fig. 1.1). A field of application for piezoelectric materials is the energy harvesting through fluid-solid interactions [6–8]. Indeed, water currents or flows in channels generally induce immersed piezoelectric thin structures to vibrate and generate an electrical power which can be harvested through a load resistance. This is a problem which involves the physics of fluids, solids and electrostatics. In this thesis, a particular configuration of a energy harvester in a fluid flow by means of experiments. The problem is then modeled and implemented in a software with finite element methods. Several modeling problems are analyzed such as the choice of the plane state assumptions in piezoelectric solids and the optimal load resistance to harvest the electrical power.

On the other hand, the chemomechanical transducer in this thesis is assumed to be made of hydrogel like materials. In general hydrogels are composed of a polymer matrix which has an elasticity given by physical, chemical or topological bonds. These materials are permeable and they have the capability of large swelling and deformation due to a solvent absorption [9]. An example of hydrogel materials are wood-like materials which are often considered as heterogeneous anisotropic hydrogels [10]. Recently, these hydrogels were employed as actuators for example in soft robotics [11], in microfluidics [12] and also in an autonomous shading system [13]

which autonomously responds to the change of humidity in the environment (see Fig. 1.2). Often, such systems are realized using bilayer structures which are able to bend significantly due to the change of stimuli.

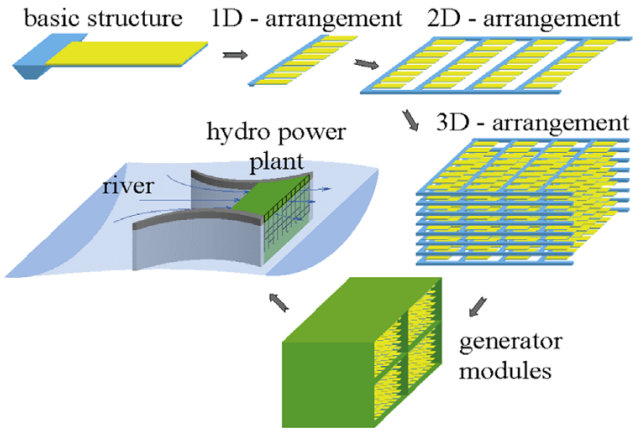

FIGURE 1.1: Energy harvesting through stacks of piezoelectric generator modules in a hydro power plant [5]. Image taken by [5].

In this thesis, we will focus on an alternative method to achieve a bending of a homogeneous hydrogel structure which is realized through different external environmental conditions. Moreover, it is investigated a mechanism to overcome one of the limitations of hydrogels which is the slowness in the response and it is studied another problem of hydrogels which is the presence of residual strains during the change of environmental conditions.

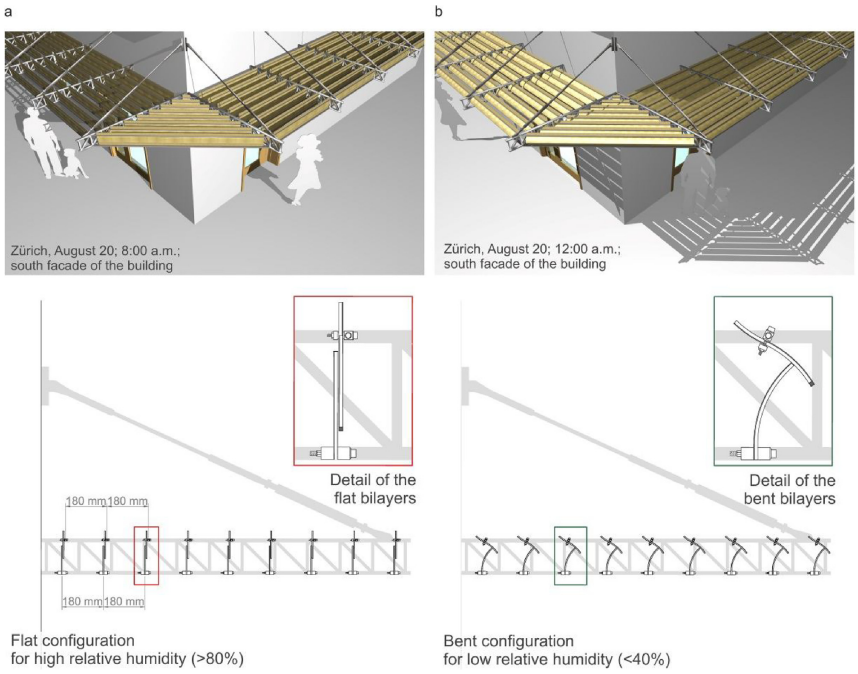

FIGURE 1.2: Autonomous shading system through bilayer wood structures proposed by [13]. The image was taken by [13].

The thesis is composed of two main chapters: a first one where it is described the behavior of piezoelectric materials, their modeling and some applications; a second

one where hydrogels materials are described together with some applications and actual limits or issues.

Chapter 2

Smart materials converting mechanical to electrical energy

2.1 Piezoelectric materials

In this section we briefly describe piezoelectric materials and their modelling framework which is used in the next sections.

Piezoelectric materials are solids composed of particular crystals in which the mechanical and electrical behavior are coupled as described in [1]. These materials exhibit the piezoelectric effect, which is historically divided into two phenomena: the direct and the converse piezoelectric effects. When a piezoelectric material is mechanically deformed, an electric polarization that is proportional to the applied strain is produced. This is called the direct piezoelectric effect and it was discovered by the Curie brothers in 1880. When the same material is subjected to an electric polarization, it deforms and the amount of strain is proportional to the polarizing field. This is called the converse piezoelectric effect and it was deduced mathematically from the fundamental principles of thermodynamics in [14] and then confirmed experimentally by the Curie brothers in the same year. These two effects usually coexist in a piezoelectric material. Therefore in an application where the direct piezoelectric effect is of particular interest (which is the case in vibration-based energy harvesting), ignoring the presence of the converse piezoelectric effect would be thermodynamically inconsistent and generally leads to wrong predictions. The most commonly used piezoelectrics are the piezoelectric ceramics which exhibit much larger coupling compared to natural crystals. The most popular of engineering piezoceramics, PZT (lead zirconate titanate), was developed at the Tokyo Institute of Technology in the 1950s. Nowadays, applications of these materials range from simple actuators to sophisticated energy harvesting devices and cover a wide range of spatial scales [3, 7, 15–19]. In particular, sensors are used in different fields for example in medical implants [20, 21], in chemistry [4] and for structural damage identification [22]. Piezoelectric actuators are used as valves in micropumps [23, 24], for active structural control [25] and in ink jet printers for actuating the ejector [26]. Energy harvesting through piezoelectric materials is applied in broadband random vibrations [27], in vortex-induced vibrations [28] and in vibrations induced by traffic on bridges [29]. The harvested energy is usually used for wireless remote power supply [30] and for recharging batteries [31]. The great influence of electrical scheme and mechanical properties in the dynamical behavior of piezoelectric materials have been studied with theoretical, computational and experimental approaches [32–34].

2.1.1 Modelling of piezoelectric materials

From a modeling point of view, the vast majority of the classical piezoelectric materials are well described by a Kirkhhoff Saint-Venant constitutive relation for the elastic contribute to the free energy and a linear coupling with the electric field [35, 36]. The two-way coupling between electricity and elasticity has been proved to be in accordance with experimental results and optimal values for electrical resistance loads. It is worth noting that some particular electro-mechanical materials, not taken in consideration in this thesis, may need to be modeled within a more general multiphysics framework [37, 38].

Kinematics

The generic problem is set in a 3D space, using the theory of nonlinear elasticity with large displacements. As standard in mechanics, descriptors are defined in a reference configuration of the body $\mathcal{B}$. The motion of the object $f(\mathbf{X}, t)$ is described by the displacement $\mathbf{u}(\mathbf{X}, t)$, a material field defined on $\mathcal{B}$; $\mathbf{X} \in \mathcal{B}$ is a material point, (X, Y, Z) its coordinates and $t \in \mathcal{T}$ an instant of the time interval $\mathcal{T}$. The deformation $\mathbf{F}$ of the body is given by the gradient of motion:

$$\mathbf{F} = \nabla f = \mathbf{I} + \nabla \mathbf{u}. \tag{2.1}$$

Elastic constitutive law

The whole body is assumed to be non-linear elastic; the reference stress $\mathbf{S}$ of a piezoelectric solid $\mathcal{B}$ is given by the Kirchhoff-Saint Venant relation between stress and strain (general form), with a coupling piezoelectric term that describes the backward feedback of an electric vector field $\mathbf{E}_{el}$ on stress:

$$\mathbf{S} = \mathbf{F}\,\mathbf{S}_e, \quad \mathbf{S}_e = \mathbb{C}\,\mathbf{E} - \mathbf{e}^T\,\mathbf{E}_{el}\,; \tag{2.2}$$

where $\mathbb{C}$ and $\mathbf{e}^T$ are respectively the stiffness of the solid and the transpose of the piezoelectric coupling tensor, $\mathbf{E} = 1/2(\mathbf{F}^T\mathbf{F} - \mathbf{I})$ is the nonlinear strain measure (Green-Lagrange strain) with $\mathbf{F}^T$ indicating the transpose of $\mathbf{F}$.

Electric constitutive law

In the case of ordinary ferroelectric ceramics the reference electric displacement $\mathbf{D}$ is assumed to be related linearly with the electric field $\mathbf{E}_{el}$ and the strain $\mathbf{E}$:

$$\mathbf{D} = \mathbf{e}\,\mathbf{E} + k_o\,\mathbf{k}\,\mathbf{E}_{el} \tag{2.3}$$

where k_o is the vacuum permittivity and $\mathbf{k}$ is the second-order tensor of dielectric relative permittivity measured at constant applied stress. Under quasi-static conditions, the electric field $\mathbf{E}_{el}$ can be written as the gradient of a potential, V, such that:

$$\mathbf{E}_{el} = -\nabla V. \tag{2.4}$$

It is worth noting that in general, all piezoelectric materials are anisotropic both from a mechanics and electrical point of view. Indeed, the matrix representation of $\mathbb{C}$, $\mathbf{e}$, $\mathbf{k}$ in a global cartesian base for a classic piezoceramic material generally is:

$$\mathbb{C} = \begin{pmatrix} C_{11} & C_{12} & C_{13} & 0 & 0 & 0 \\ C_{12} & C_{11} & C_{13} & 0 & 0 & 0 \\ C_{13} & C_{13} & C_{33} & 0 & 0 & 0 \\ 0 & 0 & 0 & C_{44} & 0 & 0 \\ 0 & 0 & 0 & 0 & C_{55} & 0 \\ 0 & 0 & 0 & 0 & 0 & C_{55} \end{pmatrix}, \tag{2.5}$$

$$\mathbf{e} = \begin{pmatrix} 0 & 0 & 0 & 0 & 0 & e_{16} \\ e_{21} & e_{22} & e_{23} & 0 & 0 & 0 \\ 0 & 0 & 0 & e_{34} & 0 & 0 \end{pmatrix}, \tag{2.6}$$

$$\mathbf{k} = \begin{pmatrix} k_{11} & 0 & 0 \\ 0 & k_{11} & 0 \\ 0 & 0 & k_{33} \end{pmatrix}. \tag{2.7}$$

The most important anisotropy is in the piezoelectric coupling tensor. Indeed, when compressed in one direction, the piezoelectric generates an electric potential along one specific direction determined by the coupling coefficients in the matrix **e**. In the following sections of the chapter we always consider such tensors with the values indicated in Table 2.1.

TABLE 2.1: Piezoelectric parameters in the global cartesian base.

Symbol	Value	Parameter
$C_{11} = C_{33}$	$1.20 * 10^{11}$[Pa]	stiffness comp. 11
$C_{12} = C_{23}$	$7.51 * 10^{10}$[Pa]	stiffness comp. 12
C_{13}	$7.52 * 10^{10}$[Pa]	stiffness comp. 13
C_{22}	$1.11 * 10^{11}$[Pa]	stiffness comp. 11
$C_{44} = C_{66}$	$2.10 * 10^{10}$[Pa]	stiffness comp. 44
C_{55}	$2.25 * 10^{10}$[Pa]	stiffness comp. 55
$e_{16} = e_{34}$	12.29[C/m]	coupling comp. 16
$e_{21} = e_{23}$	-5.35[C/m]	coupling comp. 21
e_{22}	15.78[C/m]	coupling comp. 22
$k_{11} = k_{33}$	919.1	perm. comp. 11
k_{22}	826.6	perm. comp. 22
ρ_p	7750 $\left[\text{kg} * \text{m}^{-3}\right]$	piezoelectric mass density

Balance laws

State variables of a piezoelectric material are the material vector field $\mathbf{u} = (u, v, w)$, describing the displacement, and the scalar material field V, representing the electric potential on the piezoelectric. The equations of the problem, defined on $\mathcal{B} \times \mathcal{T}$, consist of:
i) the balance of forces for the solid,

$$\operatorname{div} \mathbf{S} = \rho\, \ddot{\mathbf{u}}\,; \tag{2.8}$$

where the upper dot stays for derivative in time, and ρ is the mass density in the solid which in this section is $\rho = \rho_p$ the piezoelectric mass density.
ii) the Gauss law's for the electric field:

$$\operatorname{div} \mathbf{D} = \rho_v\,, \tag{2.9}$$

where ρ_v is the free electric charge density, assumed to be null. The balance laws 2.8, 2.9 are solved with appropriate initial and boundary conditions.

2.1.2 Modeling of energy harvesting using a piezoelectric solid

We model energy harvesting for a piezoelectric plate-like 3D body $\mathcal{B}$ clamped at one end, see Fig. 2.1. With reference to Fig. 2.1 let (o; $\mathbf{g}_1$, $\mathbf{g}_2$, $\mathbf{g}_3$) be an orthonormal reference frame, with the origin o at the position of the fixed constraint, and $\mathbf{g}_3$ leaning on the out of plane direction. The body is subjected to a periodic external force $\mathbf{F}_e$ in horizontal direction $\mathbf{g}_1$ (see Fig. 2.1) within a time interval $\mathcal{T}$ and connected to an external electrical load resistance R. The piezoelectric body has length L, width W and thickness h_p. In this problem, the boundary conditions are assigned on the

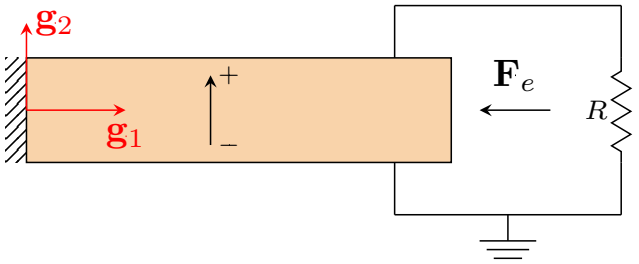

FIGURE 2.1: Plane view of a piezoelectric solid under periodic force oscillations connected to an external electrical load. The vertical black arrow indicates the direction of polarization in the material.

boundaries in the plane showed in Fig. 2.1: top, left, right, bottom, respectively $\partial\mathcal{B}_t$, $\partial\mathcal{B}_l$, $\partial\mathcal{B}_r$, $\partial\mathcal{B}_b$ and on the other boundaries $\partial\mathcal{B}_o$. In particular, the left boundary is assumed insulated from an electrical point of view:

$$\mathbf{D} \cdot \mathbf{n} = 0 \quad \text{on} \quad \partial\mathcal{B}_l \times \mathcal{T} \tag{2.10}$$

and with a fixed constraint:

$$\mathbf{u} = 0 \quad \text{on} \quad \partial\mathcal{B}_l \times \mathcal{T}, \tag{2.11}$$

where $\mathbf{n}$ the outward reference unit normal at the boundary. The right boundary is also assumed to be electrical insulated:

$$\mathbf{D} \cdot \mathbf{n} = 0 \quad \text{on} \quad \partial\mathcal{B}_r \times \mathcal{T} \tag{2.12}$$

and with the external reference force applied:

$$\mathbf{S}\,\mathbf{n} = \mathbf{F}_e = A \sin(\omega\, t)\, \mathbf{g}_1 \quad \text{on} \quad \partial\mathcal{B}_r \times \mathcal{T}, \tag{2.13}$$

where A is the force amplitude and ω its pulsation. The bottom boundary has a reference ground electrical potential:

$$V = 0 \quad \text{on} \quad \partial\mathcal{B}_b \times \mathcal{T}. \tag{2.14}$$

and it is free to deform:

$$\mathbf{S}\,\mathbf{n} = 0 \quad \text{on} \quad \partial\mathcal{B}_b \times \mathcal{T}. \tag{2.15}$$

On the top boundary we impose a voltage $V = \tilde{V}$ satisfying the relation:

$$\int_{\partial\mathcal{B}_t} \dot{\mathbf{D}} \cdot \mathbf{n}\, dA = \frac{\tilde{V}}{R} \quad \text{on} \quad \partial\mathcal{B}_t \times \mathcal{T}, \tag{2.16}$$

and at the same time we impose the condition that it is free to deform:

$$\mathbf{S}\,\mathbf{n} = 0 \quad \text{on} \quad \partial\mathcal{B}_t \times \mathcal{T}, \tag{2.17}$$

where R is the value of electrical external load resistance. Finally, the other boundaries are electrical insulated and free to deform:

$$\mathbf{S}\,\mathbf{n} = 0 \quad \text{and} \quad \mathbf{D} \cdot \mathbf{n} = 0 \quad \text{on} \quad \partial\mathcal{B}_o \times \mathcal{T}. \tag{2.18}$$

Conditions (2.14) and (2.16) deserve some additional comments. First of all, they ensure uniform charge distributions along upper and lower surfaces of both piezoelectric layers, in compliance with the adoption of planar electrodes to collect charges. The effectiveness of such design reveals to be optimal for a "single signed curvature" [34] deformation (excitation of cantilever first mode). Secondly, conditions (2.14) and (2.16) on boundaries do not force uniform potential along $\mathbf{g_1}$ (i.e. $\nabla V \cdot \mathbf{g_1} = 0$) in the bulk of the piezoelectric layers. Using these conditions, we do not explicitly impose uniform electric field along Y as commonly done in other studies [39, 40] and the non-linearity of the system (2.14, 2.16) is enhanced with respect to the width. Moreover, in the current case it is worth noting that the strain tensor $\mathbf{E}$ has components: E_{11}, representing the normal strain in horizontal direction $\mathbf{g}_1$ and E_{22}, E_{33}, representing the normal strains due to the Poisson effect in the directions $\mathbf{g}_2$ and $\mathbf{g}_3$ respectively. The strain component E_{11} during a compression generates a positive electrical polarization in the vertical direction $\mathbf{g}_2$ due to the piezoelectric coefficient e_{21} in Table 2.1. The strains E_{22} and E_{33} generate an electrical polarization in vertical direction $\mathbf{g}_2$ due to the piezoelectric coefficients e_{22} and e_{23} respectively. In particular given values in Table 2.1, during a compression in $\mathbf{g}_1$ direction the polarization induced by E_{22} is positive while the polarization induced by E_{33} is negative and smaller in absolute value to the other contributes.

Balance equations are solved with boundary conditions and null initial conditions. The electrical power harvested on the external electrical load resistance is

oscillating in time (see Fig. 2.2) and measured as:

$$P = \frac{\tilde{V}^2}{R}. \tag{2.19}$$

The average harvested power is given by:

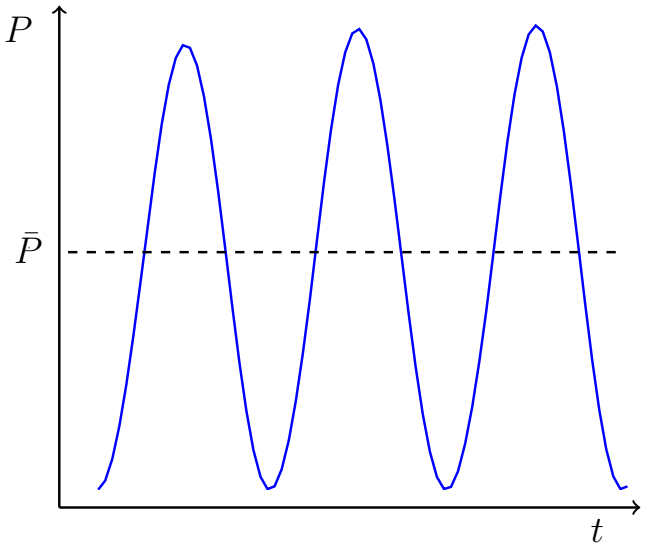

FIGURE 2.2: The piezoelectric generates an oscillatory electrical power which is harvested with an external electrical resistance load.

$$\bar{P} = \frac{1}{t_f - t_o} \int_{t_o}^{t_f} P \, dt, \tag{2.20}$$

where t_f is the final time of simulation and t_o is the initial transient time interval. In particular, $\bar{P}$ can be evaluated for different values of electrical load resistance, force amplitude and pulsation (or frequency). As showed in Fig. 2.3 the average harvested power has an optimum peak at which corresponds an optimal external load resistance. The latter depends on geometry and characteristics of force application. In the case of a sinusoidal axial force. The optimal external load resistance does not depend on the amplitude of the force but only on its frequency as can be seen in Fig. 2.3 and Fig. 2.4. The numerical trends are confirmed by neglecting shear and electrical contributions in the reference stress $\mathbf{S}$, assuming homogeneous solutions of balance equation and using eq. (2.13):

$$E_{11} = \frac{A}{C_{11}} \sin(\omega \, t). \tag{2.21}$$

In this case, the electrical boundary condition (2.16) reads as:

$$\int_{\partial \mathcal{B}_t} e_{21} \dot{E}_{11} + k_o \, k_{22} \, \dot{E}_{el2} \, dA = \frac{\tilde{V}}{R}. \tag{2.22}$$

which can be rewritten assuming a linear variation of the electric potential in the piezoelectric thickness which gives:

$$(A_t \cos(\omega \, t) - k_t \dot{\tilde{V}}) - \frac{\tilde{V}}{R} = 0 \tag{2.23}$$

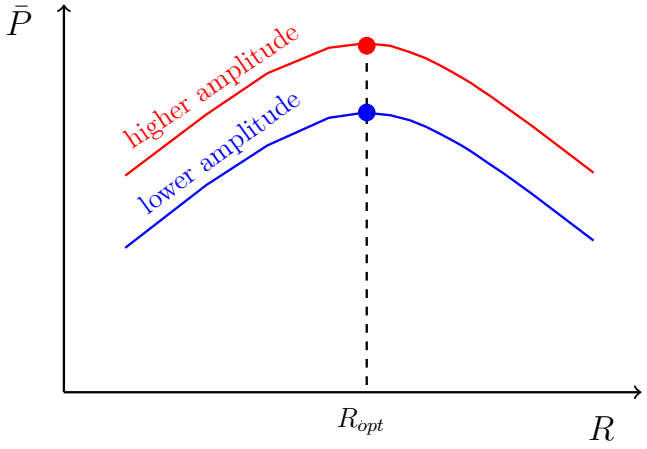

FIGURE 2.3: There is an optimal external electrical load which correspond to the maximum average electrical power harvested. Higher force amplitude induce a higher electrical power harvested; nevertheless the optimal electrical load does not depend on the force magnitude.

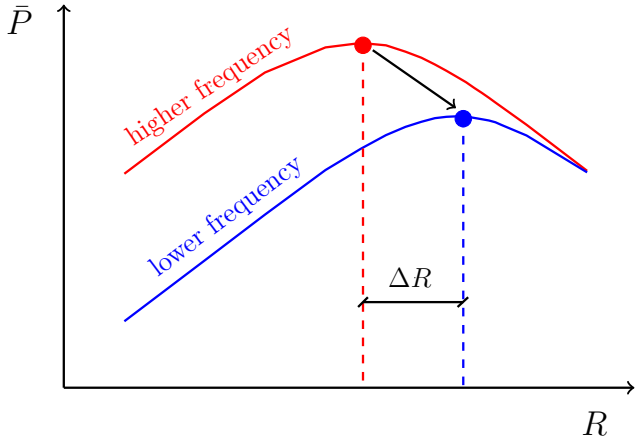

FIGURE 2.4: The optimal external electrical load which absorbs more electrical power is greater at lower force frequencies.

where the parameter A_t depends essentially on the force amplitude and the piezoelectric coefficent and k_t depends on geometric parameters and permittivity:

$$A_t = \frac{W\,L\,A\,\omega\,e_{21}}{C_{11}}, \quad k_t = \frac{W\,L\,k_{22}\,k_o}{h_p}. \tag{2.24}$$

Eq. (2.23) is an ordinary differential equation (ODE) which is solved with respect to the electrical potential $\tilde{V}$:

$$\tilde{V} = \frac{A_t\,R}{1 + k_t^2\,\omega^2\,R^2}\left(\cos(\omega\,t) + k_t\,\omega R\sin(\omega\,t) - \exp\left(-\frac{t}{k_t\,R}\right)\right). \tag{2.25}$$

From eq. (2.25) it is possible to evaluate the average electrical power harvested on the external load resistance using equations (2.19) and (2.20). The value of the optimal load resistance R_{opt} is given by setting the derivative of the average harvested

power $\bar{P}$ with respect to R equal to zero:

$$\frac{\partial \bar{P}}{\partial R} = \frac{A_t^2}{4\,\omega(1+kt^2\,\omega^2\,R^2)^3}\exp\left(-\frac{2\,t_f}{k_t\,R}\right)\bar{P}_f(k_t,\omega) = 0, \qquad \text{with} \quad \bar{P}_f(k_t,\omega) = \bar{P}_{f1} + \bar{P}_{f2} + \bar{P}_{f3}, \tag{2.26}$$

where t_o in (2.20) was assumed to be 0 and:

$$\bar{P}_{f1} = 4\,\omega\,(k_t\,R(\omega^2\,k_t\,R(k_t\,R - t_f) - 1) - t_f),$$

$$\bar{P}_{f2} = -8\,\omega\cos(\omega\,t_f)\exp\left(\frac{t_f}{k_t\,R}\right),(k_t\,R(\omega^2\,k_t\,R(2\,k_t\,R - t_f) - 2) - t_f)$$

$$\bar{P}_{f3} = \exp\left(\frac{2\,t_f}{k_t\,R}\right)\Bigg(-2\,\omega\,(k_t^2\,\omega^2\,R^2 - 1)(t_f + k_t\,R(\omega^2\,k_t\,R\,t_f - 4) - 2\,k_t\,R\cos(2\,\omega\,t_f))$$

$$+(k_t^4\,\omega^4\,R^4 - 6\,k_t^2\,\omega^2\,R^2 + 1)\sin(2\,\omega\,t_f)\Bigg). \tag{2.27}$$

The term in front of $\bar{P}_f(k_t,\omega)$:

$$\frac{A_t^2}{4\,\omega(1+kt^2\,\omega^2\,R^2)^3}\exp\left(-\frac{2\,t_f}{k_t\,R}\right), \tag{2.28}$$

is the unique term which depends on the force amplitude and cannot be zero if $A \neq 0$. This implies that R_{opt} does not depend on the force amplitude but only on geometry parameters, permittivity and force frequency due to $\bar{P}_f(k_t,\omega)$.

2.2 Validity of plane states assumptions in a cantilever piezoelectric bimorph for energy harvesting applications

In this section, we assess the accuracy of plane state assumptions in modelling the bending of bimorph piezoelectric cantilevers since these assumptions are often used to reduce computational costs especially in fluid-structure interaction problems. Reference solutions are obtained by means of fully 3D simulations. We solve a model, compliant with the standard theoretical background, able to deal with large deflections and aimed at estimating the electrical energy harvesting potential. We show that the two assumptions of plane stress and plane strain yield very different results in terms of strain and therefore lead to substantially different estimates of electrical power. The plane stress state is the best approximation of narrow cantilevers, while the plane strain is suited for wide ones. The validity ranges are defined for each of the two, in terms of the generated electrical power. Other aspects are affected by the modelling approach, such as the estimation of maximum deformation and, to a minor extent, of resonance frequencies.

In particular, we focus on a bimorph solid cantilever composed by a brass substructure placed between two piezoelectric layers. Simplified mechanical models have been proposed to study the behavior of these devices subject to external forces. A simplification, with respect to 3D models is represented by 2D models [41] which exploit the pronounced two-dimensionality of the devices motion, induced by their

slender and flat shape. The resort to simplified 2D models is often necessary to reduce the computational time of simulations in large parametric studies or in complex phenomena but it can lead to incorrect predictions due to wrong physical assumptions [39]. The 2D models can be formulated assuming either plane stress [42–44] or plane strain behavior [45, 46]. In [34], the results of numerical simulations of a bimorph beam employing the plane stress hypothesis are compared with experimental results obtaining good agreement in the estimation of electrical power generated by the device. Other models proposed by [42–44] and [46] use either of the two approaches and are not compared with experimental results. As shown in the case of composites structures by [47] the two modelling strategies need to be thoroughly assessed before being used in predictive models. Moreover, the research community working on piezoelectric has a very broad expertise, ranging from electrical to mechanical engineers. This yields possible modeling errors as reported in [39]. Despite the difference between a plane stress and plane strain hypothesis is very well known in classic structural problems [48, 49], to the best of our knowledge, this is the first comparison between these two plane state approaches in the field of piezoelectric materials and we feel that such analysis can be beneficial to researchers and professionals in the field aiming at correctly modeling and designing such devices. Here, we describe an electro-mechanical model capable of catching the key features of piezoelectric devices. The model is able to describe the piezoelectric effect for a wide range of geometries. In our simulations, the single piezoelectric device is modeled as a heterogeneous solid with different constitutive relations for the piezoelectric and the substructure layer. The piezoelectric materials chosen for the simulation are piezo-ceramic PZT-5A, whose features are reported in Table 2.1. The performances of bimorph piezoelectric beams depend on their mechanical characteristics, the features of the applied electrical load, and the external forcing. Due to strong two-way-feedback between the mechanical and the electrical aspects, fully coupled models are mandatory to accurately assess their performance. The optimum operating conditions are comprehensively described by a set of mixed load and forcing characteristics. Performance assessments in this regard have been carried out in [50] and [51].

Here, we highlight the difference between the plane stress and the plane strain hypothesis in terms of harvested electrical power and we compare these results with those from fully three-dimensional simulations. The plane stress state reveals to match reference results for the case of narrow devices, while the plane strain is appropriate for large widths. As we will see, the plane state assumptions unveil the pivotal role of the Poisson ratio in anisotropic and inhomogeneous material and the effect of the fixed constraint. Finally, we also show the existence of an optimal width in terms of harvested electrical power per unit width which can be exploited in the design of efficient piezoelectric devices feeding an electrical resistive load. The paper is organized as follows: in the second section the 3D model and the plane state assumptions are described; in the third one the carried out simulations are introduced and results discussed; conclusions are then drawn.

2.2.1 Modelling of a bimorph solid

We simulate energy harvesting from a vibrating cantilever by solving an electromechanical problem with the Finite Element Method.

Our simulated body is a bimorph cantilever of length L, width W and thickness $H = h_s + 2h_p$, with h_s and h_p respectively the brass substructure and the piezoelectric

layer thickness. The whole body is modeled as a non-linear elastic solid, whose flexural motion is generated by a time-varying distributed load. Such loading scheme resembles the typical situation of flow induced vibrations. With reference to Fig. 2.5 let $(o; \mathbf{g}_1, \mathbf{g}_2, \mathbf{g}_3)$ be an orthonormal reference frame, with the origin o at the position of the fixed constraint, and $\mathbf{g}_3$ leaning on the out of plane direction. The generation of electric power is mainly induced by the compression and extension along $\mathbf{g_1}$. It is worth highlighting that, given the properties in Table 2.1, there are also minor contributions given by deformation along $\mathbf{g_2}$ and $\mathbf{g_3}$, the latter being negative. The piezoelectric layers are connected to a passive electrical resistance load per unit width. A tip mass is added to reduce the resonance frequencies as usually done in experimental tests [34]. We set our problem in 3D, using the theory of nonlinear elasticity with

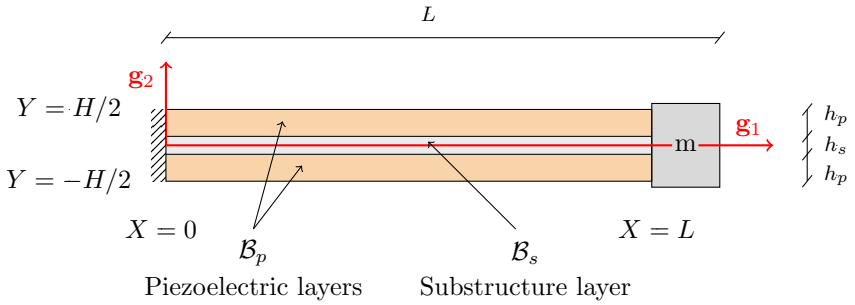

FIGURE 2.5: Reference shape of bimorph cantilever composed by two piezoeletric layers and one substructure with a tip mass m. The geometrical parameters are listed in Table 2.2.

large displacements. As standard in mechanics, we define descriptors in a reference configuration $\mathcal{B}$. Then, let $\mathbf{X} \in \mathcal{B}$ be a material point, (X, Y, Z) its coordinates and $t \in \mathcal{T}$ an instant of the time interval $\mathcal{T}$. The reference computational domain in our model is the union of a piezoelectric and a substructure domain $\mathcal{B} = \mathcal{B}_s \cup \mathcal{B}_p$. The motion of the object $f(\mathbf{X}, t)$ is described by the displacement $\mathbf{u}(\mathbf{X}, t)$, a material field defined on $\mathcal{B}$.

Elastic constitutive law

The whole body is assumed to be non-linear elastic; the substructure is isotropic and the piezoelectric layers $\mathcal{B}_p$ are anisotropic with response given by the Kirchhoff-Saint Venant constitutive relation showed in eq. (2.2); both are homogeneous. The reference stress $\mathbf{S}(\mathbf{X}, t)$ in the substructure layer $\mathcal{B}_s$ is given by a Kirchhoff-Saint Venant constitutive relation (isotropic form):

$$\mathbf{S} = \mathbf{F}\,\mathbf{S}_e, \quad \mathbf{S}_e = \frac{Y_s}{1+\nu_s}\,\mathbf{E} + \frac{Y_s\,\nu_s}{(1+\nu_s)(1-2\,\nu_s)}\,\mathrm{tr}(\mathbf{E})\,\mathbf{I}\,, \tag{2.29}$$

where Y_s, ν_s are respectively the Young and Poisson moduli of the material and $\mathrm{tr}(\mathbf{E})$ the trace of the strain tensor. Moreover, here the solid mass density of balance law (2.8) is $\rho = \rho_s$ for the substructure layer and $\rho = \rho_p$ for the piezoelectric layer

Boundary and initial conditions

We solve the system of equations (2.8, 2.9) in the unknowns $\mathbf{u}$ and V that satisfy given boundary and initial conditions.

In this case, from a mechanics point of view, we apply these boundary conditions:

$$\begin{aligned} &\mathbf{u}(\mathbf{X},t) = \mathbf{0} && \text{at} \quad X = 0\,, \\ &\mathbf{S}(\mathbf{X},t)\mathbf{n} = \mathbf{F}_e \equiv A\sin(2\pi\tau)\, t_s\, \mathbf{g}_2 && \text{at} \quad Y = H/2\,, \\ &\mathbf{S}(\mathbf{X},t)\mathbf{n} = \mathbf{F}_m \equiv \frac{\rho_{\text{tip}}}{H}\,\mathbf{I}\;\ddot{\mathbf{u}}\big|_{x=L} && \text{at} \quad X = L\,, \end{aligned} \tag{2.30}$$

with $\mathbf{n}$ the outward normal to the boundary of the body in the reference configuration.

The first condition in eq. (2.30) mimics the fixed constraint, while the second is the external force applied to the top boundary. The parameter A is the amplitude of the harmonic load, $\tau = t\,f$ is the non dimensional time, with f the force frequency and t_s is a smooth ramp for the initial application of the load $t_s = (1 - exp(-\tau))$. Finally, the third condition in eq. (2.30) represents the effect of an added mass as in Fig. (2.5), where ρ_{tip} is the added mass for unit width placed at the tip of the cantilever.

For what regards the electrical boundary conditions, they depend on the chosen electrical scheme (i.e. either series or parallel connection). In this work we enforce parallel connection between the piezoelectric layers. We don't expect different conclusions if a series connection is instead applied. The parallel condition is realized assigning a reference electrical potential V_{ref} on piezoelectric boundaries in contact with the substructure:

$$V(\mathbf{X},t) = V_{ref} = 0 \quad \forall \mathbf{X} \quad \text{at} \quad Y = \frac{h_s}{2} \quad \text{and} \quad Y = -\frac{h_s}{2}. \tag{2.31}$$

This condition assumes the metallic substructure to be much more conductive than the piezoelectric. On top and bottom boundary surfaces ($Y = \pm H/2$) we impose a voltage $\tilde{V}$ satisfying the relation:

$$\int_{\partial\mathcal{B}_{Y=\pm H/2}} \dot{\mathbf{D}} \cdot \mathbf{n}\, dA = \frac{\tilde{V}}{R} \tag{2.32}$$

where $R = \rho_{\text{el}}\, W$ is the external electrical load resistance and ρ_{el} is the electrical resistance per unit width as shown in Fig.(2.6).

It is worth highlighting that the coupling coefficient e_{21} (see Table 2.1), due to the Poisson normal strain along $\mathbf{g}_3$ (see Fig. 2.6) induces a polarization opposed to the ones generated by normal strains in the other directions, and thus is decremental to the power harvesting. Optimization of geometrical configurations will be the object of a future research.

We assign vanishing initial conditions in terms of displacement and electric potential. Physical model parameters and non-vanishing components in the global cartesian base of $\mathbb{C}$, $\mathbf{e}$ and $\mathbf{k}$ are listed in Tables (2.1,2.2).

Plane stress and plane strain hypothesis

Under plane state hypothesis, the third component of displacement is assumed to be uniform along $\mathbf{g}_3$ direction. The plane stress hypothesis, employed in [34, 42–44] for bimorph piezoelectric beams, is obtained by imposing $S_{e13} = S_{e31} = S_{e23} = S_{e32} = S_{e33} = 0$. Using eq. (2.29), we obtain the condition for the substructure:

$$E_{13} = E_{23} = 0, \quad E_{33} = \frac{E_{11} + E_{22}}{v_s - 1} v_s \tag{2.33}$$

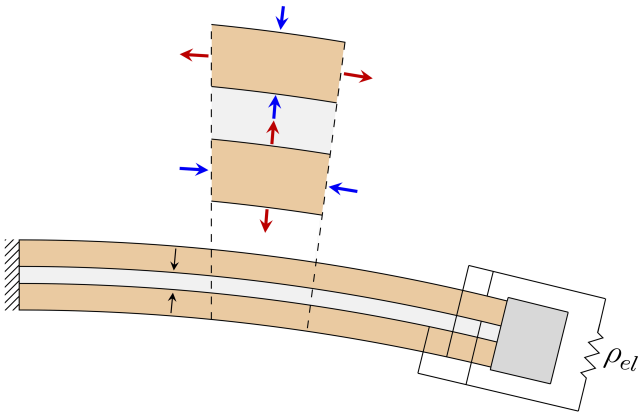

FIGURE 2.6: Poisson effect; during downward bending the top layer is stretched in the X direction (red arrows) while it is compressed in Y direction (blue arrows). The bottom layer behaves conversely. It is important to account for this effect also in the plane out of the paper. The figure also shows the parallel connection of the two piezoelectric layers to an electrical resistive load per unit width ρ_{el}. Black arrows indicate polarization direction in response to deformation of top and bottom layer, respectively.

while using eq. (2.2) we obtain for the piezoelectric layers:

$$E_{23} = 0, \quad E_{13} = \frac{e_{16} E_{el1}}{C_{55}}, \qquad E_{33} = \frac{e_{21} E_{el2} - C_{13} E_{11} - C_{23} E_{22}}{C_{33}}. \tag{2.34}$$

On the contrary, the plane strain condition, used in [46] for beams with $W >> H$, assumes

$$E_{13} = E_{23} = E_{33} = 0. \tag{2.35}$$

Solid Eigenfrequencies

The eigenfrequencies of the system, important to understand the dynamical behavior of the solid, can be estimated considering only the contribute of elastic terms as in [34] and assuming:

$$\mathbf{u} = \hat{\mathbf{u}}(\mathbf{X}) \exp(-j\,\omega\, t) \quad \text{and} \quad \mathbf{F}_e = 0\,, \tag{2.36}$$

where ω is the set of natural pulsations of the beam. The influence of the ratio between the tip mass and the total mass is investigated using the plane state assumptions. The total mass of the beam m_b is evaluated as:

$$m_b = \rho_s\, L\, W\, h_s + 2\rho_p\, L\, W\, h_p. \tag{2.37}$$

Post-processing

The electrical power absorbed by the load resistance is estimated by evaluating using equations (2.19,2.20).

The volume average in the 3D model of the axial strain component along $\mathbf{g}_3$ is evaluated by:

$$\bar{\mathbf{E}}_{33} = \frac{1}{L_p\,(h_s + 2h_p)\,W} \int_{\mathcal{B}} \mathbf{E}_{33}\, dV. \tag{2.38}$$

Finally, the electrical current density in the piezoelectric material is given by $\mathbf{J} = \dot{\mathbf{D}}$. This relation implies that the main contribution to the electrical current density comes from the coupling with the deformation term in the electrical displacement.

2.2.2 Simulations and results

The reference solution for the problem at hand is provided by the numerical integration of the system of equations (2.8, 2.9), together with boundary and initial conditions, on a 3D domain, by means of a Finite Element Method. The simplified 2D models are obtained by solving the same balance laws on a 2D (XY) space, and by enforcing conditions (2.33) and (2.34) for the plane stress, and (2.35) for the plane strain case. In this section we compare results of these two 2D models against the reference 3D solution, in terms of harvested electrical power. Moreover, we investigate some further differences in terms of eigenfrequencies and frequency behavior between the two plane state assumptions.

Validity of modeling plane state assumptions

The validity of each plane state assumption depends on the width W of the solid body. Generally, the plane strain condition is best suited to large bodies, i.e. $W/H >> 1$, while a thin one, $W/H << 1$ is better approximated by a plane stress condition. In Fig. 2.7a we observe the deformation ϵ_{33}, for two different widths in a 3D simulation, along direction $\mathbf{g}_3$ at position $X = L/2$ and $Y = h_s/2 + h_p/2$, i.e. in the upper piezoelectric layer.

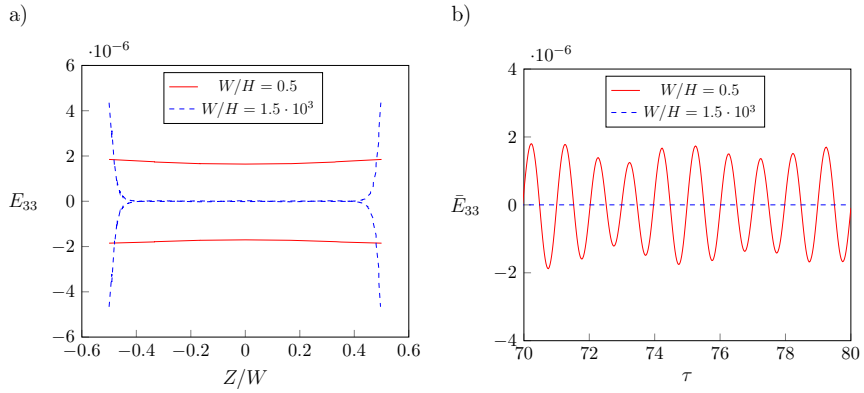

FIGURE 2.7: Results from the 3D model for two different widths $W/H = 0.5$ and $W/H = 1.5 \cdot 10^3$. a) Distribution of strain ϵ_{33} along direction $\mathbf{g}_3$ at position $X = L/2$ and $Y = h_s/2 + h_p/2$ at two different instants. The large beam ($W/H = 1.5 \cdot 10^3$, blue dashed trace) yields $\epsilon_{33} = 0$ almost everywhere, except at the boundaries; on the contrary, the narrow one ($W/H = 0.5$, red solid trace) shows a quasi uniform distribution for ϵ_{33}. b) Volume averaged strain $\bar{\epsilon}_{33}$ vs a time interval τ. $\bar{\epsilon}_{33}$ of wide beams attains much smaller values than for the narrow ones.

The narrow cantilever, namely $W/H = 0.5$, undergoes a quasi-uniform strain E_{33} (which conforms to the plane stress hypothesis); on the contrary, the large cantilever, namely $W/H = 1.5 \cdot 10^3$, has $E_{33} \approx 0$ for the vast majority of the section (which conforms to the plane strain hypothesis), except at the borders, where the body is free to deform and therefore the stress vanishes. With reference to Fig. 2.7b, the time history of the volume average strain $\bar{E}_{33}$ confirms that the larger body is indeed under plane strain conditions. However it is still not clear what the effectiveness of

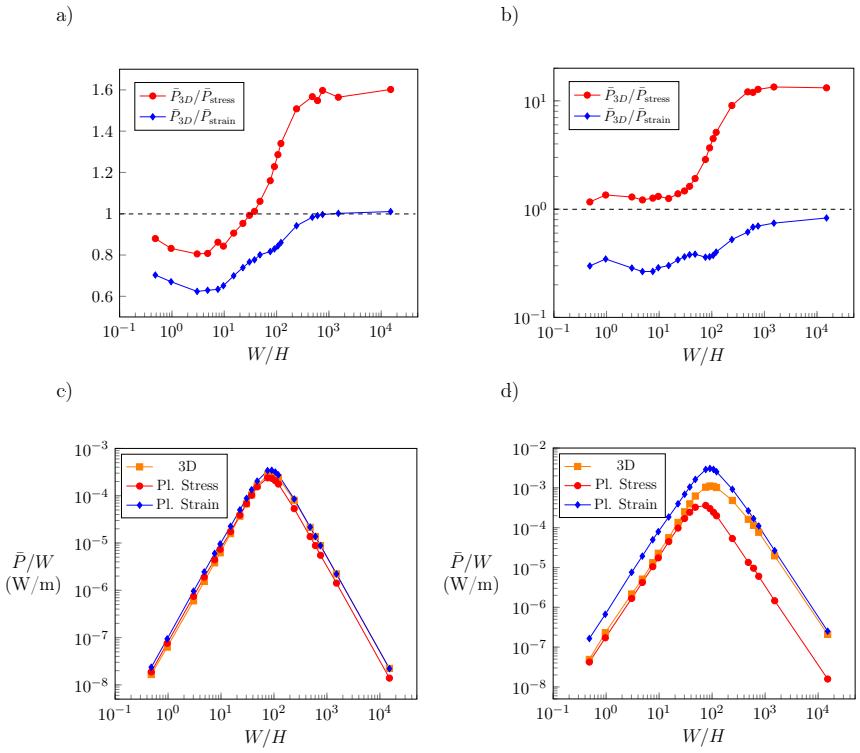

FIGURE 2.8: Top panels: time averaged electrical power $\bar{P}$ of each 2D model, normalized by the reference value provided by the 3D model, plotted against non-dimensional width W/H. Bottom panels: average electrical power per unit width plotted against non-dimensional width W/H for different models; forcing frequency is $f = 30$ Hz a) and c), and $f = 60$ Hz b) and d. External load resistance per unit width is fixed at $\rho_{\text{el}} = 3.15 \cdot 10^5$ Ohm/m; For both forcing frequencies, the plane strain 2D model is in accordance with 3D results for the ratio $W/H > 10^3$; on the contrary, plane stress is closer to 3D results for $W/H < 10$. The bottom panels show that there exists a width producing a maximum electrical power: such condition corresponds to the match between internal and external electrical resistance. Both plane state assumptions fail consistently in the range $10 < W/H < 10^3$, where the power peak is located.

the plane state assumptions is. With this purpose, we performed some simulations using different widths W and a fixed height H and length L for the 3D model. The time averaged electrical power generated by the piezoelectric layers is compared between the two different models with two forcing frequencies, namely $f = 30$ Hz and $f = 60$ Hz, plot a and plot b of Fig. 2.8, respectively. For ratios $W/H > 10^3$ the average electrical power given by the plane strain assumption $\bar{P}_{\text{strain}}$ better approximates the 3D one $\bar{P}_{3D}$, still with an error that can go up to 30% for the higher frequency. On the other hand, for $W/H < 10$ the plane stress hypothesis yields better results

with a maximum error around 30% as well. It is worth recalling that the non-linear dependance of the average electrical power on the width stems from the boundary condition 2.31; hence, the width of the device determines the inner resistance of the generator. This is confirmed by the plots c) and d) of Fig. 2.8 where it is shown that the maximum power is located at the width corresponding to the external electrical resistance load ρ_{el}. We also observe that the peak power estimate provided by the 3D model is not matched by any of the two 2D models.

Further differences between plane state assumptions

The plane state assumptions also yield different results in terms of frequency response at fixed ratio $W/H = 50$. The comparison between the first and second resonance frequencies with the ratio m/m_b is shown in Fig. 2.9. In the analyzed setup, according to modal analysis of eq. (2.36), we change the added mass value that modifies consistently the resonance frequencies for $m < 0.5\, m_b$. Moreover, plane stress hypothesis yields a lower resonance frequency, and this effect becomes more relevant for the second mode. Particularly, for our simulations employing $m/m_b \approx 1.4$ and parameters values listed in Table (2.1, 2.2) we obtain for the first mode the resonance frequencies $f_r \approx 44$ (Hz) and $f_r \approx 47$ (Hz), respectively using the plane stress and the plane strain hypothesis. For what regards plane stress and plain strain hypothesis we carried out two further types of analysis: firstly we varied the electrical load resistance from $R = 10^3$ Ohm to $R = 10^6$ Ohm at fixed external force frequency $f = 30$ Hz (Fig. 2.10a); then we vary the frequency from $f = 30$ Hz to $f = 60$ Hz with $\rho_{el} = 3.15 \cdot 10^5$ Ohm/m (Fig. 2.10b). The variation of frequency highlights a dependence of the first resonant frequency of the device on the modelling assumption: $f_r \approx 45$ Hz for the plane stress model and $f_r \approx 50$ in the case of plane strain.

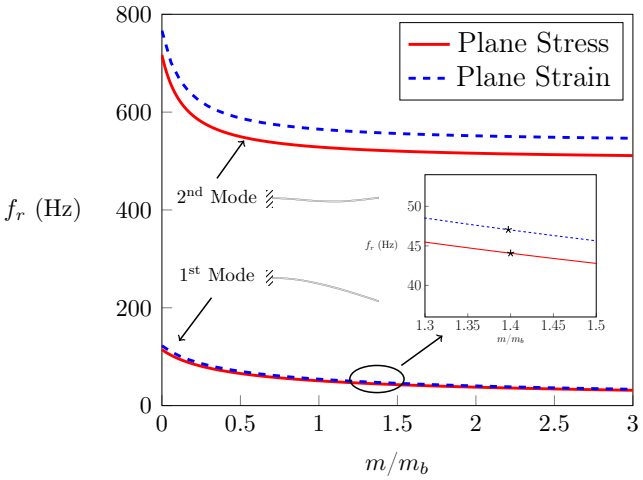

FIGURE 2.9: Effect of added mass on first and second resonance frequencies, with both plane state hypotheses. The resonance frequencies are lower in the plane stress case. The two black stars in the close-up frame indicate the resonance frequencies of the first mode for the device modeled in the following with parameters listed in Tables (2.1,2.2).

The variation of load resistance shows that the maximum power also depends on such assumption, with the plane stress yielding a larger value. Apart from such vertical shift, shape of the power-load curve does not seem to depend on the underlying assumption. The optimum value for the load resistance is slightly different;

this suggests that the mechanical hypothesis on the plane state influences also the electrical counterpart of the result, as stated in the previous section.

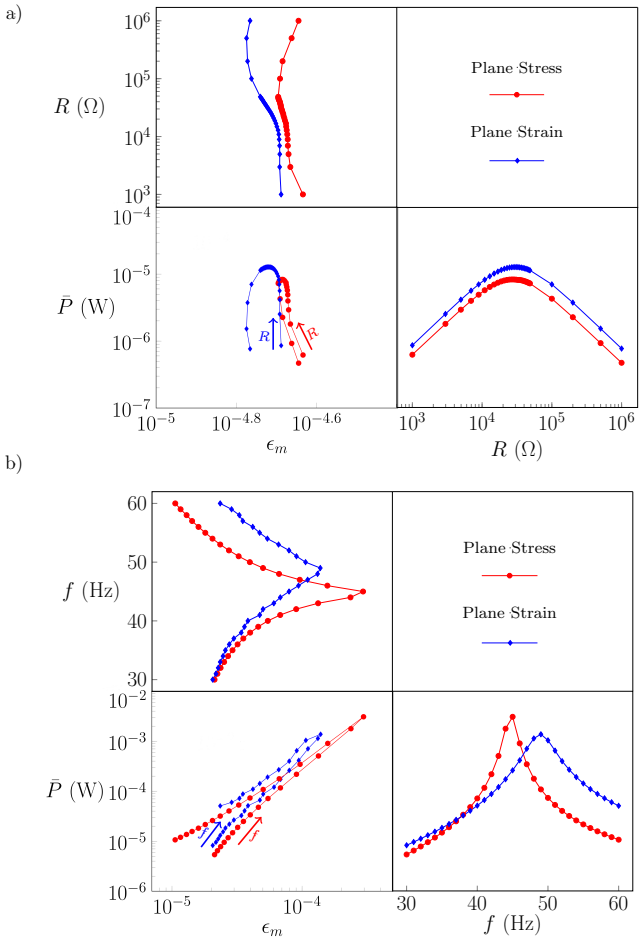

FIGURE 2.10: Plane stress VS plane strain with parallel connection. a) We show average electrical power $\bar{P}$ and maximum strain $\mathbf{E}_m$ with fixed external force frequency $f = 30$ Hz, varying the load resistance from 10^3 to 10^6 Ohm. The maximum average power is developed with $R \approx 3 \cdot 10^4$ Ohm, while the maximum strain is reached with small value of load resistance. b) We show same features with fixed load resistance $R = 10^4$ Ohm, varying the frequency fro 30 to 60 Hz. The plane stress and the plane strain conditions yield different resonance frequencies and this implies different results in terms of both electrical power and maximum strain of the device.

Finally, the analysis in terms of maximum strain ϵ_m for all the time interval of the simulation and the generated power is of paramount importance to accurately predict the range of operativeness of the system. The maximum strain, see Fig. 2.10, has a non-linear dependence on electrical resistance load R. This behavior is the result of the feedback on mechanical properties induced by the external resistive load. This opens up the possibility to design a device with tunable mechanical properties. Moreover, the plane state assumption yields very different results in terms of maximum strain. With reference to Fig. 2.11, employing the plane stress modelling, with $f = 60$ Hz and $A = 7.5$ kPa, leads to a substantial underestimation of the maximum deformation, thus exposing the device to the possibility of structural failure. By contrast, in this case, the fracture threshold given by [52] is exceeded by the 3D model

and also by the 2D model with the plane strain assumption.

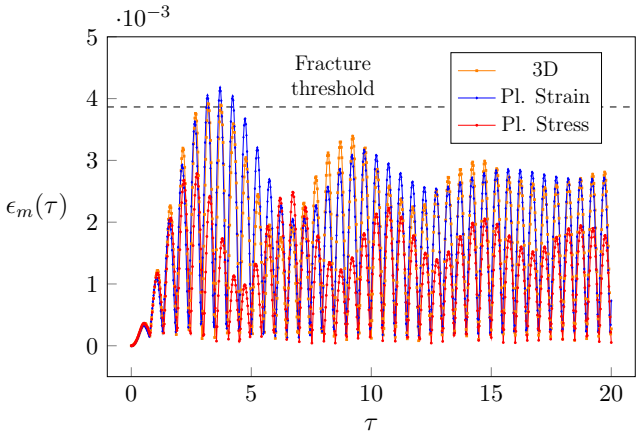

FIGURE 2.11: Comparison between maximum strain over time for different models. Results at fixed external force frequency $f = 60$ Hz, $\rho_{el} = 3.15 \cdot 10^5$ Ohm/m and force amplitude $A = 7.5$ kPa. The fracture threshold is exceeded by the 3D and plane strain model for this case while the plane stress assumption underestimate the maximum deformation.

TABLE 2.2: Key model and material parameters of the bimorph solid.

Symbol	Value	Parameter
L	5.08 [cm]	solid length
W	3.18 [cm]	solid width
h_p	0.026 [cm]	piezoelectric layer
h_s	0.014 [cm]	substructure layer
Y_s	$1.05 * 10^{11}$[Pa]	Young's modulus
ν_s	0.3	Poisson number
ρ_s	9000 $[\mathrm{kg} * \mathrm{m}^{-3}]$	substructure mass density
ρ_{tip}	571.8 $[\mathrm{kg/m}^2]$	tip mass
A	50.0 $[\mathrm{N/m}^2]$	load amplitude
m_b	0.085 [kg]	beam total mass
ρ_{el}	$3.15 * 10^5$ [Ohm/m]	electrical resistance
ρ_p	7750 $[\mathrm{kg} * \mathrm{m}^{-3}]$	piezoelectric mass density

In this work we assess the validity of two alternative plane state assumptions for the modelling of piezoelectric cantilevers often employed for energy harvesting. While there are modelling scenarios which require the resort to such simplified 2D models, extreme attention must be paid to the underlying assumptions, especially when the models are employed to predict power performance. Indeed the two hypothesis are here demonstrated to be good approximations of the real 3D system only in specific ranges of width-to-height shape ratio of the piezoelectric device. More specifically, the plane stress assumption better approximates the reference solution in the range $W/H < 10$. By contrast, the plane strain condition yields results

closer to 3D solution for ratios $W/H > 10^3$. Between these two thresholds both assumptions fail, and such disagreement is relevant in view of the fact that the power peak of the analyzed device falls in this range. Such power peak, here estimated assuming a simple resistive load, results by the match between the external load and the internal resistance of the piezoelectric device, the latter being largely over (or under) estimated in broad ranges of the above mentioned shape ratio. Marginal differences are also reported in the estimation of resonance frequencies which, however, could represent a misleading datum for an optimized design of energy harvesting devices. Finally, employing the plane stress modelling would lead to a substantial underestimation of the maximum allowable deformation, thus exposing the device to possibility of structural failure.

2.3 Fluid flow induced vibrations of a piezoelectric cantilever unimorph and energy harvesting

One of the most studied areas in piezoelectric materials is the use of the piezoelectric effect to convert ambient vibration into useful electrical energy. An example of such application is the energy harvesting through piezoelectric materials in a flowing fluid [7, 8]. Fluid flow has the potential to provide significant mechanical energy input for piezoelectric harvesters. However, the efficient conversion of the bulk kinetic energy of a steady and uniform flow into time-dependent elastic energy in the piezoelectric structure remains a significant challenge. Moreover, the modeling of such multiphysics problem has still to be fully investigated and requires advanced numerical tools which can be tackled with COMSOL Multiphysics. In this section, we focus on the generation of electrical power through a piezoelectric solid immersed in a channel using an inverted configuration of the solid with respect to the flow, similarly to [8]. The solid is a non-homogeneous bilayer solid, clamped at one end on a fixed circular constraint. The solid is composed of two layers; one is piezoelectric (PZT 5-A) while the other has a structural function and enables the generation of electrical power by the piezoelectric layer. Experiments were carried out in the Hydraulics Lab at University of Roma Tre with the help of Ing. Mario La Rosa for what regards the engineering of the electrical setup. Experimental results, which are later described together with the experimental setup, are compared with numerical simulations.

2.3.1 Experimental setup and results

Energy harvesting through a piezoelectric sheet immersed in a fluid flow in a channel is investigated by means of an experimental setup (see cartoon of Fig. 2.12 and actual setup in Fig. 2.13). The fluid flow has inlet velocity U, which is reached using two electrical water pumps and measured indirectly with an electronic rate of flow gauge. The device measures a rate of flow Q which is related to the inlet velocity by:

$$U = \frac{Q}{W_c\, T_c}, \tag{2.39}$$

where $W_c = 0.81$ m is the fixed channel width and T_c is the water height level just before the position of the experimental setup.

The experimental setup consists of a fixed aluminum cylinder of diameter 2.6 cm where it is clamped one end of a structural steel sheet with size 11 cm $\times$5 cm $\times$0.01 cm attached (using a biphasic glue) to a piezoelectric sheet. The steel sheet has

Young's modulus 210 GPa measured through a load test and by the first frequency of the transversal vibration.

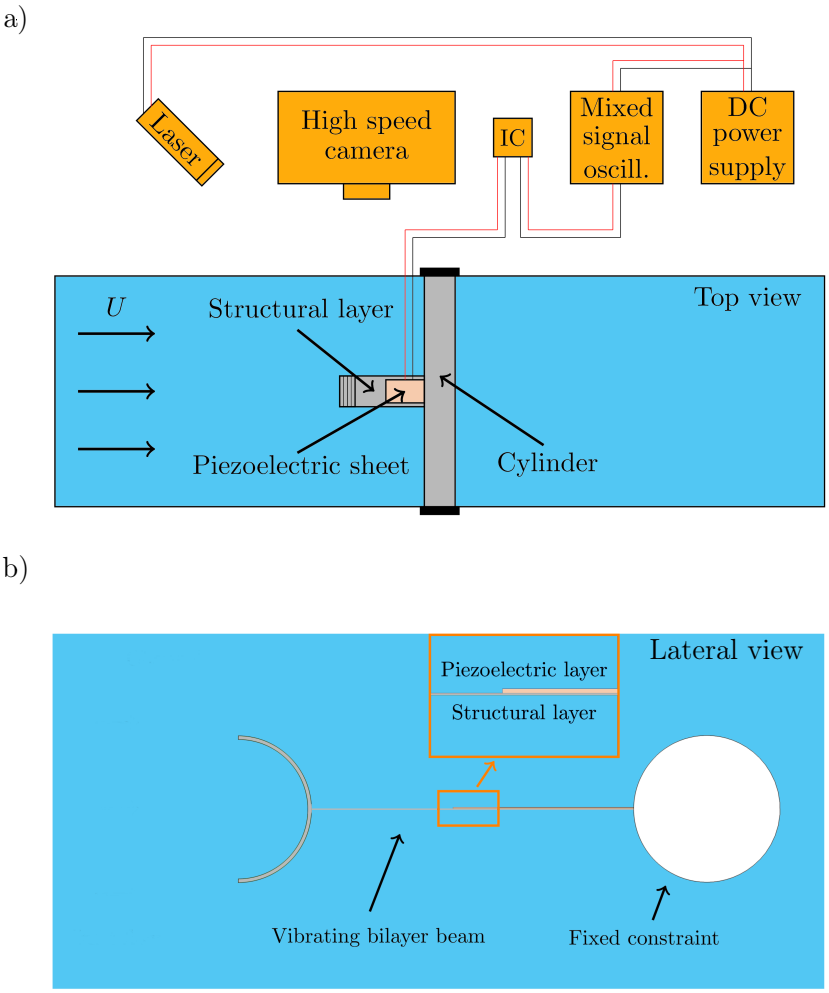

FIGURE 2.12: Cartoon of the experimental setup for energy harvesting. a) Top view of the setup which consists of a channel with a fluid inlet velocity U and a fixed cylinder with a clamped bilayer structure composed of a structural and a piezoelectric layer. b) Lateral view of the setup; the bilayer structure has a half cylinder which increases vibrations.

The piezoelectric sheet is the DuraAct Patch P-876-A12 made by Physik Instrumente which is a laminated structure consisting of a piezoceramic PZT-5A plate, electrodes and polymer materials. The elastic and electric properties of such solid are listed in Table 2.1. Moreover, the piezoelectric sheet is manufactured with a bubble-free injection method and the polymer coating simultaneously serves as a mechanical preload as well as an electrical insulation since the piezoceramic and the electrodes have to be immersed in water. The piezoelectric sheet has an operating voltage between -100 V and 400 V and size: 6.1 cm $\times$3.5 cm $\times$0.02 cm. Two twisted insulated electrical wires connected to the piezoelectric sheet transmit the generated electrical potential to a variable external load resistance (from 1 kOhm to approximately 5 MOhm) which is put outside the channel and not in contact with water. It is worth noting that, a double constraint was inserted in the experimental setup to avoid a too huge deformation of the bilayer structure which over a critical velocity

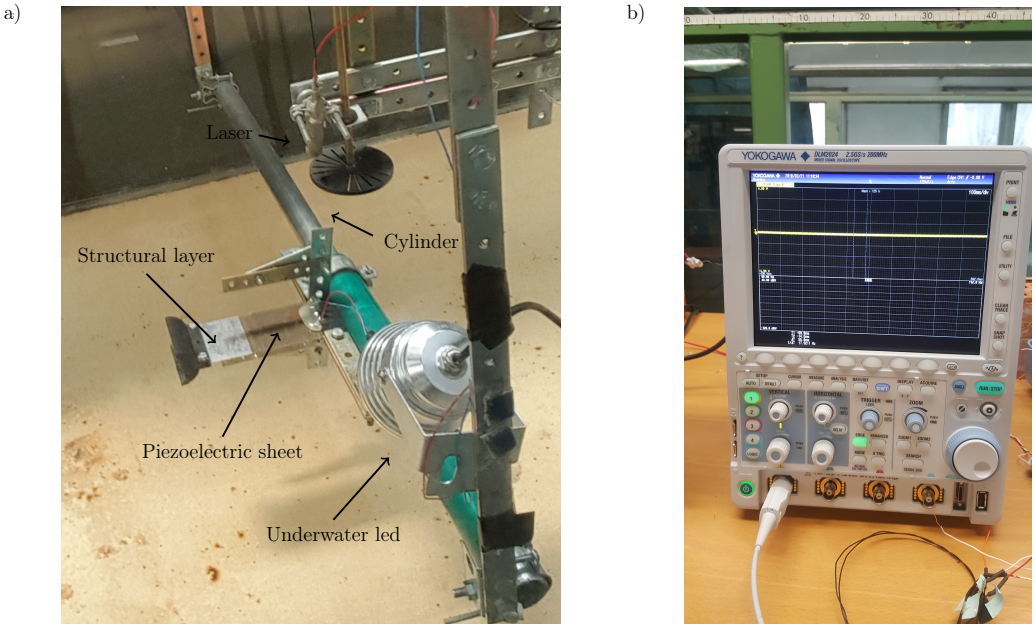

FIGURE 2.13: Actual experimental setup for energy harvesting. a) View of the experimental setup in the channel: a bilayer structure, a cylinder, an underwater led and a laser. b) The mixed signal oscilloscope used to measure the electrical potential generated by the piezoelectric sheet.

may induces a steady bent shape as observed in [8]. Experiments were analyzed through the following devices:

- A mixed signal oscilloscope Yokogawa DLM2024 2.5 GS/s 200 MHz
- A differential probe Yogogawa 700924
- A laser
- A high speed camera
- An underwater led

In particular, the mixed oscilloscope (see Fig. 2.13b) was powered by a DC power supply and the differential probe was connected on one end to the oscilloscope itself and on the other end to the external variable load resistance extremities. Due to the fluid flow and the presence of the half cylinder the bilayer oscillates (see Fig. 2.14) and generates an electrical potential which is measured with the differential probe (see Fig. 2.14 bottom). Images of the bilayer structure are obtained through a high speed camera which has a time resolution of 2000 frames per second. Using expression in eq. (2.19) it is possible to evaluate the harvested electrical power over time which is showed in Fig. 2.15 for the inlet fluid velocity $U = 0.8$ m/s. Then, shifting the electrical load resistance from 1 kOhm to 4 MOhm it is possible to evaluate the average harvested electrical power for two different inlet velocities $U = 0.8$ m/s (red dots) and $U = 1.1$ m/s (orange dots), see Fig. 2.16. The average harvested power has a maximum similarly to figures Fig. (2.3, 2.4). The optimal load resistance changes with the inlet fluid velocity; in particular it is found $R_{opt} = 45$ kOhm for $U = 0.8$ m/s and $R_{opt} = 200$ kOhm for $U = 1.1$ m/s. The transversal vibration frequency of the bilayer structure is evaluated through image analysis and through a fast Fourier

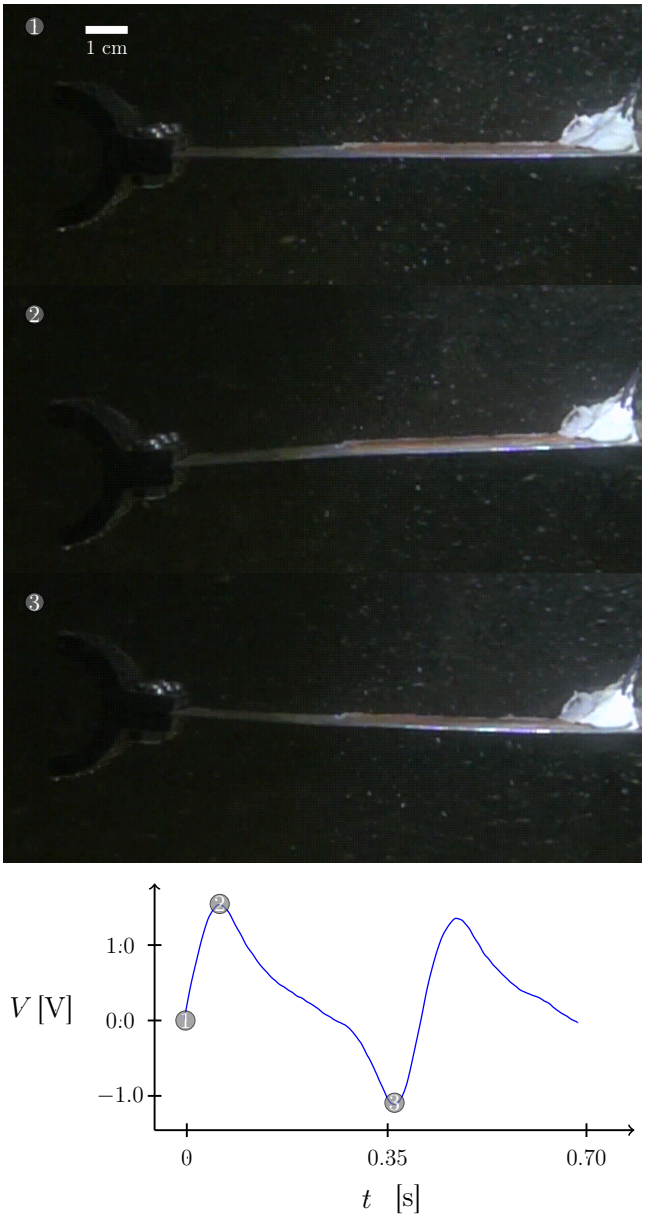

FIGURE 2.14: Video frames of the experiment with the inlet fluid velocity $U = 0.8$ m/s. The bilayer structure oscillates periodically due to the fluid flow. The deformation of the piezoelectric sheet generates an electrical potential on the external load resistance which is measured with the mixed signal oscilloscope.

transform of the electrical potential signal on the external load resistance. The fast Fourier transform allows to find the main frequency of the bilayer vibration which for the inlet fluid velocity $U = 0.8$ m/s is 2.6 Hz and for $U = 1.1$ m/s is 1.4 Hz. Indeed, at $U = 1.1$ m/s the bilayer vibrates at lower frequencies since the critical inlet fluid velocity is exceeded but the solid still oscillates due to the presence of the constraints showed in Fig. 2.13. The lower frequency induces a large optimal load resistance as shown in Fig. 2.16. Since, the optimal load resistance changes with the inlet fluid velocity a resistive matching circuit is required to maximize the harvested electrical power. This, may be object of further investigations as well as the analysis of the fluid field with the laser and the particle image velocimetry (PIV).

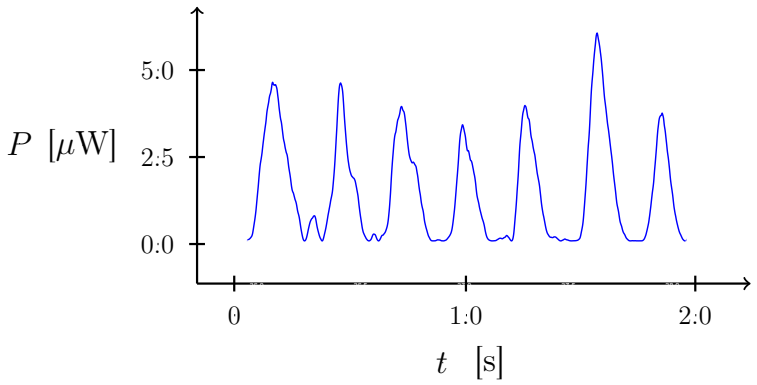

FIGURE 2.15: Harvested electrical power on load resistance over time in the experiment with inlet fluid velocity $U = 0.8$ m/s.

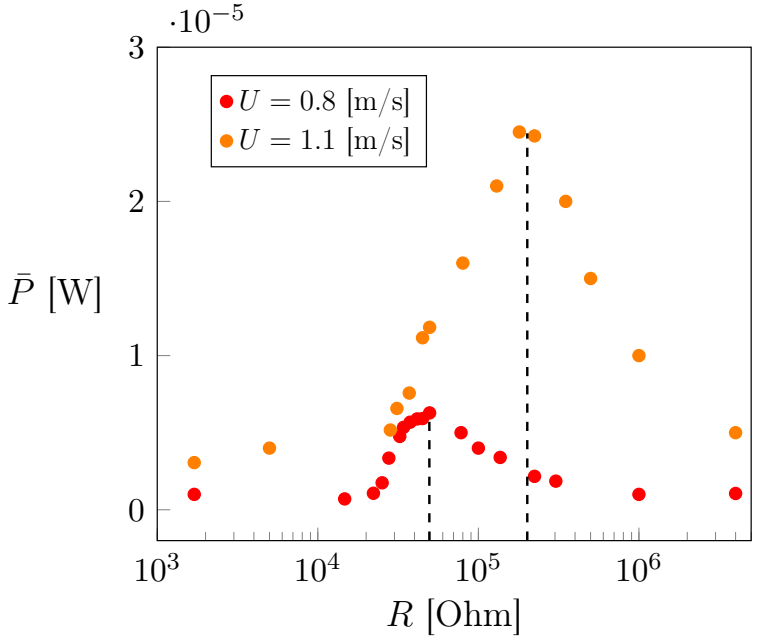

FIGURE 2.16: The average electrical power is evaluated for different values of the electrical load resistance R and for two inlet fluid velocities $U = 0.8$ m/s (red dots) and $U = 1.1$ m/s (orange dots). The optimal load resistance changes with different inlet velocities in accordance to the fact that the force frequency acting on the piezoelectric device changes as well.

2.3.2 Modelling of a piezoelectric cantilever immersed in a fluid flow

The problem is investigated using a numerical model which gives as result the electrical power harvested on the external electrical load resistance. In the model, we use the fluid-structure interaction (FSI) package of COMSOL together with the electrostatics and electric circuit packages. In particular, large deformations of the solid are effectively described through the moving mesh and the remeshing features of COMSOL as in [53, 54]. The advantage of numerical simulations easily allows parametric studies for different sizes of the half cylinder and for different inlet velocities to optimize the energy harvesting device. It is worth noting that in this case the multiphysics approach is necessary as some relevant informations about the energy harvesting just arise by the coupling between different physics.

The model is solved in a bi-dimensional (2D) space using a orthonormal reference frame (o, $\mathbf{e}_1$, $\mathbf{e}_2$) and coordinates (X,Y), with o the origin and $\mathbf{e}_1$ leaning on the horizontal axis of symmetry of the channel. The computational domain Ω is the union of a solid domain Ω_s, assumed as reference configuration, and a mesh domain Ω_m, (see, Fig. 2.17) which represents the domain occupied by the fluid at any instant t of the time interval $\mathcal{T}$. In particular, the solid domain is composed of a piezoelectric solid Ω_{sp} which, when deformed, develops an electrical field and a structural solid Ω_{ss} which has a half cylinder shape to improve vibrations and does not generate any electrical field. The piezoelectric solid is the PZT-5A which was already used in the previous simulations and in the performed experiments. The elastic effect of the polymer material which insulates the piezoceramic in the experiments is neglected in the model. Moreover, the Young's modulus of the half cylinder at the end of the structure in the simulations is assumed the same of the steel since it is thick and its deformation could be neglected.

The balance equations for the solid are written with respect to Ω_s (material, or Lagrangian formulation), while those for the fluid are written with respect to Ω_m (Arbitrary Eulerian-Lagrangian (ALE) formulation [55]). The channel has height H_f and length L_f, the piezoelectric solid has a length L_p and thickness h_p, and the structural solid has length L_s and thickness h_s. Both solids are clamped to a circular fixed constraint of diameter D (the white colored circle in Fig. 2.16). State variables of the model are the material vector field $\mathbf{u}_s$, describing the displacement of the solid, the vector field $\mathbf{v}_f$, representing the velocity of the fluid, the material scalar field V, describing the electric potential in the piezoelectric solid and the vector field $\mathbf{u}_m$, describing the mesh displacement with respect to the mesh domain Ω_{mo} which is regenerated at each remeshing. The equations of the problem consist of two equations for the fluid, the balance of forces and the conservation of mass, one for the solid, the balance of forces, one additional for the piezoelectric solid, the Gauss's Law and a last one for the mesh displacement in the mesh domain usually taken as a Poisson's like equation [56]:

$$
\begin{aligned}
\rho_f \dot{\mathbf{v}}_f + \rho_f (\nabla \mathbf{v}_f)(\mathbf{v}_f - \dot{\mathbf{u}}_m) &= \operatorname{div} \Gamma \quad \text{in } \Omega_m \times \mathcal{T}, \\
\operatorname{div} \mathbf{v}_f &= 0 \quad \text{in } \Omega_m \times \mathcal{T}, \\
\rho_s \ddot{\mathbf{u}}_s &= \operatorname{div} \mathbf{S} \quad \text{in } \Omega_s \times \mathcal{T}, \\
\operatorname{div} \mathbf{D} &= 0 \quad \text{in } \Omega_{sp} \times \mathcal{T}, \\
\operatorname{div}(\mathbb{A} \nabla \mathbf{u}_m) &= 0 \quad \text{in } \Omega_{mo} \times \mathcal{T}.
\end{aligned}
\tag{2.40}
$$

The upper dot indicates the time derivative, ∇ the nabla operator, div the divergence operator, ρ_f the fluid mass density, Γ the fluid stress, ρ_s the solid mass density, $\mathbf{S}$ the solid reference stress, $\mathbf{D}$ the electric displacement of the piezoelectric solid and $\mathbb{A}$ the Winslow operator [56]:

$$(\mathbb{A}\nabla \mathbf{u}_m)_{ij} = A_{ijhk}(u_m)_{h,k}. \tag{2.41}$$

The fluid is assumed incompressible and linearly viscous with dynamics viscosity

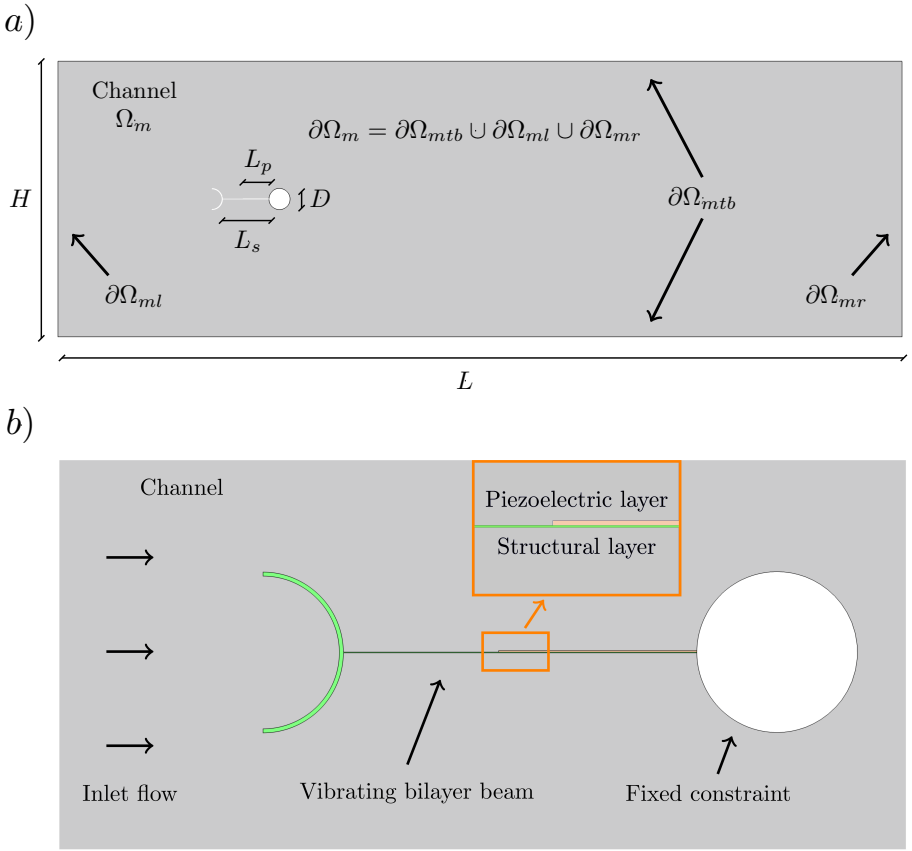

FIGURE 2.17: a) Initial geometry of the model with the boundaries of the channel where some boundary conditions are applied. The gray colored domain represents the fluid. b) Zoom of the initial geometry close to the solid. The green domain is the structural solid and the orange domain is the piezoelectric solid which is connected to an external electrical load resistance not shown in the figure.

μ_f; its stress Γ is given by:

$$\Gamma = -p_f \mathbf{I} + \mu_f(\nabla \mathbf{v}_f + (\nabla \mathbf{v}_f)^T), \tag{2.42}$$

where p_f is the fluid pressure and $\mathbf{I}$ is the identity matrix. Both structural and piezoelectric solid are assumed to be linear elastic:

$$\mathbf{S} = \mathbf{F}\,\mathbf{S}^e, \tag{2.43}$$

with $\mathbf{F} = \mathbf{I} + \nabla \mathbf{u}_s$ the deformation gradient and with stress response $\mathbf{S}^e$ given by eq. (2.29) for the structural solid Ω_{ss} and by eq. (2.2) for the piezoelectric solid Ω_{sp}. In the structural solid, Y_s and ν_s are respectively the Young's modulus and the Poisson ratio of the material. In the piezoelectric solid $\mathbb{C}$ is the stiffness tensor, $\mathbf{e}$ is

the piezoelectric coupling tensor and $\mathbf{E}_{el} = -\nabla V$ is the electric field. Parameters of the geometry and the fluid are indicated in Table (2.3), while parameters of the solids and the non-zero components of $\mathbb{C}$ and $\mathbf{e}$ are indicated in Table (2.1). Finally, the electric displacement in the piezoelectric solid is given by eq.(2.3). System of equations (2.40) is supplemented with boundary and initial conditions; $\partial\Omega_{sm}$ is the interface between the solid body and the fluid, where FSI boundary conditions are posed:

$$\mathbf{T}\,\mathbf{n} = -\Gamma\,\mathbf{n}\,, \quad \mathbf{v}_f = \dot{\mathbf{u}}_m = \dot{\mathbf{u}}_s \quad \text{on } \partial\Omega_{sm} \times \mathcal{T}, \tag{2.44}$$

with $\mathbf{n}$ normal to the solid boundary and $\mathbf{T} = \mathbf{S}(\mathbf{F}^*)^{-1}$ the Cauchy stress in the solid; on the boundaries of the channel $\partial\Omega_m$ we assign a no-moving condition for the mesh:

$$\mathbf{u}_m = 0 \quad \text{on } \partial\Omega_m \times \mathcal{T}, \tag{2.45}$$

Nevertheless, on the channel boundaries we assign additional conditions. In particular, on the top and bottom boundaries of the channel $\partial\Omega_{mtb}$ we assign a no slip wall condition:

$$\mathbf{v}_f = 0 \quad \text{on } \partial\Omega_{mtb} \times \mathcal{T} \tag{2.46}$$

and on the left boundary of the channel $\partial\Omega_{ml}$ we assign a horizontal inlet fluid velocity condition:

$$\mathbf{v}_f = (1 - \exp(-t/\tau_c))Ug(Y)\,\mathbf{e}_1 \quad \text{on } \partial\Omega_{ml} \times \mathcal{T}, \tag{2.47}$$

with τ a characteristic time, U the steady inlet velocity and $g(Y)$ the vertical profile of the inlet flow:

$$g(Y) = \frac{(Y - H/2)(Y + H/2)}{(-H^2/4)}. \tag{2.48}$$

Finally, on the right boundary of the channel $\partial\Omega_{mr}$ we assign a outlet condition:

$$p_f = 0 \quad \text{on } \partial\Omega_{mr} \times \mathcal{T}. \tag{2.49}$$

At the interface between the piezoelectric solid and the structural solid $\partial\Omega_{spb}$ we assign a null reference electrical potential $V = 0$, while on the top boundary of the piezoelectric solid $\partial\Omega_{spt}$ we assign a potential $V = \tilde{V}$ such that it holds:

$$\int_{\partial\Omega_{spt}} \dot{\mathbf{D}} \cdot \mathbf{n}\; ds = \frac{\tilde{V}}{R} \tag{2.50}$$

where R is the external electrical load resistance. The left and right boundaries of the piezoelectric solid $\partial\Omega_{spl}$ are assumed to be insulated from an electrical point of view:

$$\mathbf{D} \cdot \mathbf{n} = 0 \quad \text{on } \partial\Omega_{spl} \times \mathcal{T}. \tag{2.51}$$

On the interface between the solid and the fixed circular constraint $\partial\Omega_{sc}$ the displacement of the solid is null:

$$\mathbf{u}_s = 0 \quad \text{on } \partial\Omega_{sc} \times \mathcal{T}. \tag{2.52}$$

Finally, we assign homogeneous initial conditions. All parameters of the model are listed in Tables (2.1, 2.3). Reynolds number of simulations is approximately 10^5.

2.3.3 Simulations and results

By solving system eq. (2.40) together with boundary and initial conditions, using data of Tables (2.1, 2.3), we obtain large deformations of the solid due to the fluid kinetics energy which is converted into elastic energy of the solid. In Fig. 2.18, fluid pressure and vorticity fields over a region of the domain are observed at different instants. The vorticity field is evaluated by taking the third component of the curl of

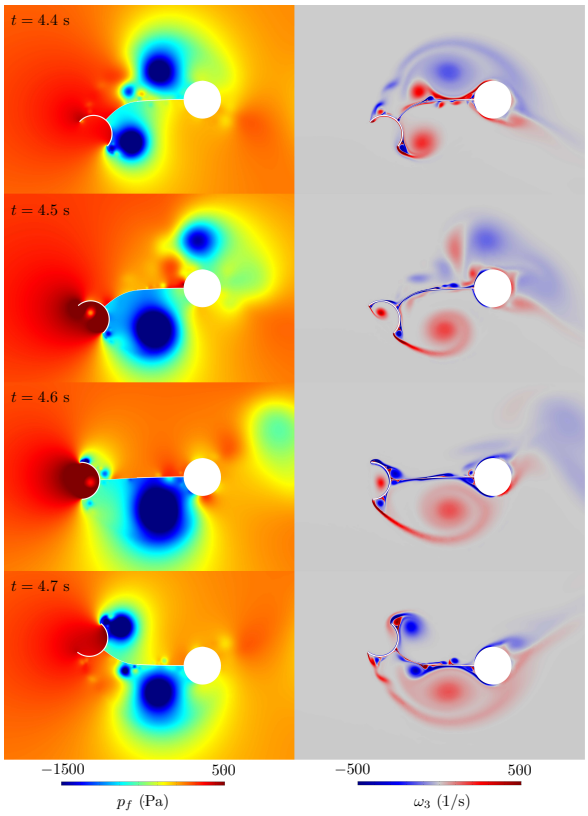

FIGURE 2.18: Pressure and vorticity fields at different instants. The solid exhibits large deformations which are described by the moving mesh and the remeshing features.

the fluid velocity:

$$\omega_f = (\nabla \times \mathbf{v}_f) \cdot \mathbf{e}_3. \tag{2.53}$$

In particular, a large circular vortex (see Fig. 2.19) is created by the presence of the half cylinder. The latter is essential to increase vibrations of the solid and harvest more electrical power in such configuration. The pressure profile over a horizontal cut line below the solid shows a traveling wave which is not compensated by the pressure above the solid itself. This pressure difference induces a deformation which can be measured through the vertical displacement at the tip of the solid (see Fig. 2.20a). The displacement, after a transient state due to the evolution of the inlet profile over time, reaches a stationary oscillatory behavior. The frequency of oscillations is evaluated through a frequency spectrum based on the fast Fourier transform algorithm and showed in Fig. 2.20b for different inlet fluid velocities. The vibration amplitude increases with the inlet fluid velocity as showed in experimental results [8]. Moreover, also the vibration frequency reasonably increases with the inlet fluid velocity; in particular, we obtain $f = 1.4$ [Hz] and $f = 1.6$ [Hz], respectively for $U = 0.5$ [m/s] blue curve and $U = 1.0$ [m/s] red curve. It is worth noting, that

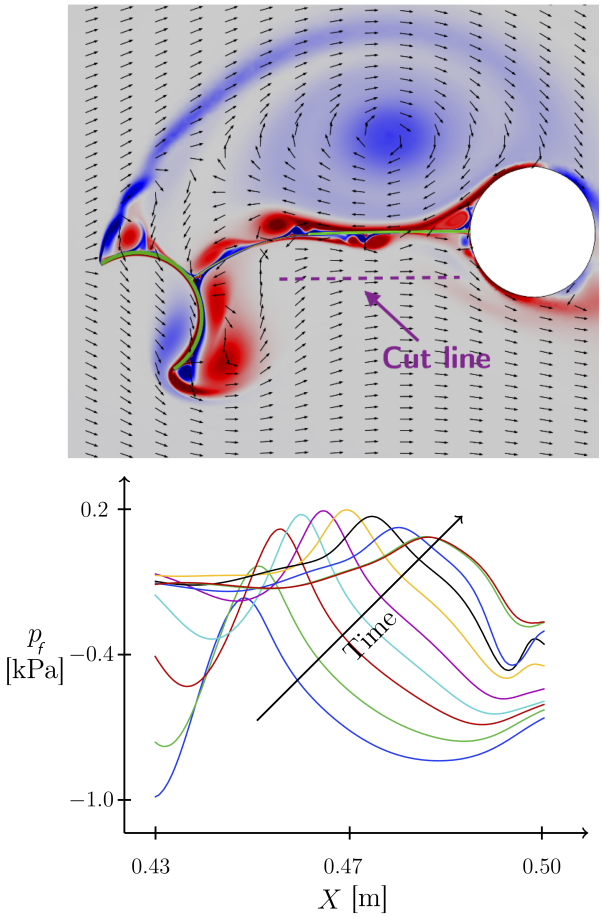

FIGURE 2.19: Top: Zoom of vorticity field and cut line where the pressure is evaluated at different instants. Bottom: Pressure is evaluated at different instants on the cut line showed in the top image. The pressure moves forward like a wave and induces large deformations of the solid.

these latter results may go against the experimental results which showed a lower frequency of the solid vibration at a higher velocity. However, the lower frequency observed in the experiments is due to the fact that the critical fluid velocity was reached and the double geometric constraint (which was not inserted in the model) had a primary role in the origin of a low frequency vibration mode.

The elastic energy of the piezoelectric solid is transformed into electrical energy and harvested through an external electrical load resistance. The harvested electrical power over time is showed in Fig. 2.20 and evaluated by expression in eq (2.19). The average harvested electrical power is approximately 0.5 [mW/m] which is in agreement with classical experimental results [3, 34] and with results of experiments carried out. It is worth noting, that the optimal electrical resistance load, which maximize the harvested electrical power, was not investigated through numerical means. Indeed, in this case, the optimal electrical resistance load depends on the vibration frequency of the solid and therefore changes with the inlet fluid velocity as demonstrated in Fig. 2.19. This is quite important in order to design a resistive matching circuit which optimize the energy harvesting [57].

A further improvement of the model may be represented by the use of RANS-based turbulence models which could describe more effectively the fluid flow and its interaction with the solid.

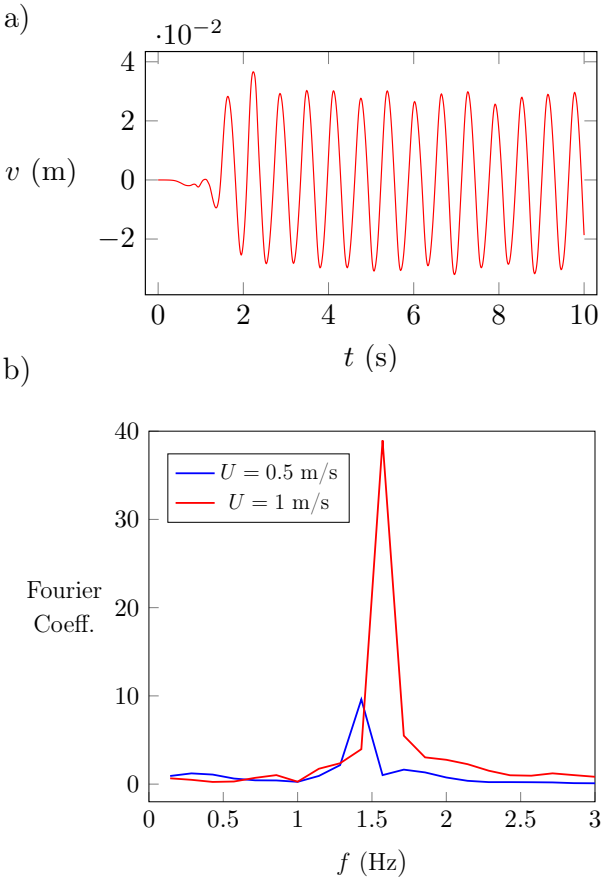

FIGURE 2.20: Vertical displacement of the solid evaluated at the free tip and its frequency spectrum. a) A stationary oscillatory movement is obtained after a transient state. b) The frequency spectrum of the vertical displacement for two different inlet fluid velocities $U = 0.5$ [m/s] blue curve and $U = 1.0$ [m/s] red curve. The peaks represent the frequencies of solid vibration.

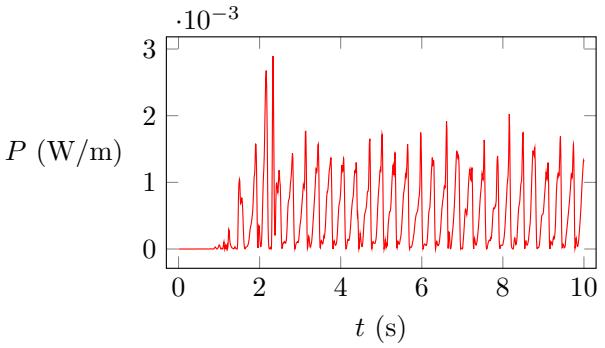

FIGURE 2.21: Harvested electrical power on load resistance over time. After the transient state, the harvested average electrical power is steady and not null.

TABLE 2.3: Geometry of the model and fluid physical parameters

Symbol	Value	Parameter
L_f	2 [m]	channel length
H_f	0.65 [m]	channel height
L_s	0.11 [m]	length of structural solid
L_p	0.061 [m]	length of piezoelectric solid
h_s	$1 \cdot 10^{-4}$ [m]	structural layer thickness
h_p	$2 \cdot 10^{-4}$ [m]	piezoelectric layer thickness
D	0.05 [m]	fixed constraint diameter
ρ_f	1000 $[\mathrm{kg} * \mathrm{m}^{-3}]$	fluid mass density
μ_f	10^{-3} [Pa $*$ s]	dynamic fluid viscosity
U	1 $[\mathrm{m} * \mathrm{s}^{-1}]$	fluid inlet velocity
τ_c	1 [s]	characteristic time
ρ_s	7800 $[\mathrm{kg} * \mathrm{m}^{-3}]$	solid mass density
Y_s	10^{11} [Pa]	Young's modulus
ν_s	0.3	Poisson ratio
R	10^4 [Ohm]	electrical load resistance

Chapter 3

Smart materials converting chemical to mechanical energy

3.1 Hydrogel materials

Hydrogels are materials made of polymer chains linked with bonds called also cross-links which give an elasticity to the material. The main feature of hydrogels is the capability of large swelling and deformation due to the solvent absorption. The latter process generally ends with a final steady state characterized by a chemical equilibrium between hydrogels and environment that yields an increase of the hydrogel initial volume depending mainly on the elastic stiffness, temperature and dis-affinity between polymer and solvent. Indeed, the polymer chains are able to absorb other type of molecules from the external environment by literally "stretching" themselves. In these materials, physics, chemistry and mechanics are coupled in one single problem. This strong interaction between different fields lets arise also peculiar phenomena such as collapses, instabilities, unexpected volume transitions and phase coexistences that have been intensively studied for decades by the scientific community [9, 58–62]. These materials can be designed to be responsive with respect to different kind of stimuli such as chemical, electrical or thermal stimuli. In the common case, during swelling and de-swelling chemical energy is converted into mechanical energy which can be used to realize: soft machines [11] muscles-like actuators [63], microfluidic actuators [12], valves [64] and micropumps [65]. In particular, the focus of this thesis will be on the conversion of chemical energy intended as the absorption or release of a liquid by a solid body due to a change of the environment humidity or of the content of solvent.

3.1.1 Modelling of hydrogels

The starting point is the multiphysics model presented and discussed in Ref. [66] and successively refined in Ref. [67], where the buckling dynamics of a solvent–stimulated and stretched elastomeric sheet are investigated. The physical processes associated with swelling and de–swelling are described within the limits of a nonlinear field theory which views water–polymer mixture as a homogenized continuum body, allowing for a mass flux of the solvent [68–71]. The mathematical modelling is derived from first principles: the principle of null working and the conservation of the water mass deliver the balance equations of forces and solvent concentration, respectively; the dissipation principles select the admissible constitutive processes.

Kinematics

We introduce a *dry-reference state* $\mathcal{B}_d$ of the gel, and denote with $X_d \in \mathcal{B}_d$ a material point and with $t \in \mathcal{T}$ an instant of the time interval $\mathcal{T}$. Our multiphysics model of gel has two state variables: the displacement field $\mathbf{u}_d(X_d, t)$ ($[\mathbf{u}_d]$=m), which gives the actual position x, at time t, of the point X_d as $x = X_d + \mathbf{u}_d(X_d, t)$[1], and the molar water-concentration per unit dry volume $c_d(X_d, t)$ ($[c_d]$ =mol/m^3). One of keys of the general model is the volumetric constraint coupling the two state variables:

$$J_d = \det \mathbf{F}_d = \hat{J}_d(c_d) = 1 + \Omega c_d \,, \tag{3.1.1}$$

where $\mathbf{F}_d = \mathbf{I} + \nabla \mathbf{u}_d$ is the deformation gradient and Ω is the molar volume of the solvent ($[\Omega]$ = m^3/mol). The constraint (3.1.1) implies that any change in volume of the gel is accompanied by uptake or release of solvent. This in turn entails that the actual volume-element dv of the body is related to its dry volume-element dV_d through the water concentration c_d, by the formula

$$\frac{dv}{dV_d} = J_d = \hat{J}_d(c_d) = 1 + \Omega c_d \,. \tag{3.1.2}$$

Stress and chemical potential

The constitutive equation for the stress $\mathbf{S}_d$ ($[\mathbf{S}_d]$=Pa = J/m^3) at the dry configuration $\mathcal{B}_d$, henceforth termed dry–reference stress, and for the chemical potential μ ($[\mu]$=J/mol) are derived from a relaxed version of the Flory–Rehner thermodynamic model [72, 73]. It is based on a free energy ψ per unit dry volume which depends on $\mathbf{F}_d$ through an elastic component ψ_e, and on c_d through a polymer–water mixing energy ψ_m: $\psi = \psi_e + \psi_m$. The relaxed free–energy ψ_r includes the volumetric constraint:

$$\psi_r(\mathbf{F}_d, c_d, p) = \psi_e(\mathbf{F}_d) + \psi_m(c_d) - p(J_d - \hat{J}(c_d)) \,. \tag{3.1.3}$$

The pressure p represents the reaction to the volumetric constraint, which maintains the volume change J_d due to the displacement equal to the one due to solvent absorption or release $\hat{J}(c_d)$. Key features of ψ (or ψ_r) are the following: (**i**) ψ is a density per unit volume of the dry polymer; (**ii**) the elastic contribution ψ_e hampers swelling; (**iii**) the mixing contribution ψ_m favors swelling. The constitutive equations for the stress $\mathbf{S}_d$ and the chemical potential μ come from dissipation issues and prescribe that

$$\mathbf{S}_d = \hat{\mathbf{S}}_d(\mathbf{F}_d) - p\,\mathbf{F}_d^\star \quad \text{and} \quad \mu = \hat{\mu}(c_d) + p\,\Omega \,, \tag{3.1.4}$$

with

$$\hat{\mathbf{S}}_d(\mathbf{F}_d) = \frac{\partial \psi_e}{\partial \mathbf{F}_d} \,, \quad \hat{\mu}(c_d) = \frac{\partial \psi_m}{\partial c_d} \,, \quad \text{and} \quad \mathbf{F}_d^\star = J_d\,\mathbf{F}_d^{-T} \,. \tag{3.1.5}$$

Typically, the Flory–Rehner thermodynamic model prescribes a neo-Hookean elastic energy ψ_e and a polymer–water mixing energy ψ_m:

$$\psi_e(\mathbf{F}_d) = \frac{G_d}{2}(\mathbf{F}_d \cdot \mathbf{F}_d - 3) \,, \quad \psi_m(c_d) = \frac{\mathcal{R}T}{\Omega}\, h(c_d) \,, \tag{3.1.6}$$

with

$$h(c_d) = \Omega\, c_d \log \frac{\Omega\, c_d}{1 + \Omega\, c_d} + \chi\, \frac{\Omega\, c_d}{1 + \Omega\, c_d} \,, \quad [h] = 1 \,, \tag{3.1.7}$$

[1] Or, equivalently, through the corresponding position vectors: $\mathbf{x} = X_d + \mathbf{u}_d(X_d, t)$.

G being the shear modulus of the dry polymer, $\mathcal{R}$ the universal gas constant, T the temperature, and χ the Flory parameter. Their physical units are $[G_d]$=J/m^3, $[\mathcal{R}]$ =J/(K mol), $[T]$ = K. The non dimensional Flory parameter χ, called dis-affinity, is specific of each water–polymer pair. The parameter χ may possibly depend on temperature and deformation; these dependence are important when temperature–driven volume transition in hydrogels is studied, as in Refs. [62, 74, 75].

From (3.1.4 , 3.1.5) and (3.1.6, 3.1.7) we obtain the constitutive equations for the dry-reference stress $\hat{\mathbf{S}}_d(\mathbf{F}_d)$ and for chemical potential $\hat{\mu}(c_d)$; this latter can be rewritten in terms of J_d by exploiting the volumetric constraint (3.1.1):

$$\begin{aligned} &\hat{\mathbf{S}}_d(\mathbf{F}_d) = G_d\,\mathbf{F}_d\,, \\ &\hat{\mu}(c_d) = \hat{\mu}(J_d) = \mathcal{R}\,T\Big(\log\frac{J_d-1}{J_d} + \frac{1}{J_d} + \frac{\chi}{J_d^2}\Big)\,. \end{aligned} \tag{3.1.8}$$

The actual stress (Cauchy) $\mathbf{T}$ is then given by the constitutive term $\hat{\mathbf{T}}(\mathbf{F}_d)$ minus the pressure term

$$\mathbf{T} = J_d^{-1}\mathbf{S}_d\,\mathbf{F}_d^T = \hat{\mathbf{T}}(\mathbf{F}_d) - p\,\mathbf{I}\,, \tag{3.1.9}$$

with $\hat{\mathbf{T}}(\mathbf{F}_d) = G_d/J_d\,\mathbf{B}$, and $\mathbf{B} = \mathbf{F}_d\,\mathbf{F}_d^T$.

Solvent flux

A key element in the transient swelling and de–swelling processes is the solvent flux; here, we assume the following prescription for the reference solvent flux $\mathbf{h}_d$, $[\mathbf{h}_d]$=mol/(m^2 s),

$$\mathbf{h}_d = \mathbf{h}_d(\mathbf{F}_d, c_d, p) = -\mathbf{M}(\mathbf{F}_d, c_d)\nabla(\hat{\mu}(c_d) + p\,\Omega)\,. \tag{3.1.10}$$

which is consistent with the dissipation principle, provided that the mobility tensor $\mathbf{M}(\mathbf{F}_d, c_d)$ is positive definite; $[\mathbf{M}]$=mol^2/(s m J). Among the many admissible representations for the mobility, here we assume $\mathbf{M}$ to be isotropic, and diffusion always to remain isotropic during any process. This is a largely shared assumptions (see Refs. [68, 70, 71], and Ref. [66] for a full discussion on the representations of $\mathbf{M}$ different from the isotropic one), and linearly dependent on c_d. We have:

$$\mathbf{M}(\mathbf{F}_d, c_d) = \frac{D}{\mathcal{R}T}\,c_d\mathbf{C}_d^{-1}\,, \quad \mathbf{C}_d = \mathbf{F}_d^T\mathbf{F}_d\,, \tag{3.1.11}$$

with D ($[D]$=m^2/s) the diffusivity. Using $\mathbf{m}$ to denote the outward unit normal, $q_s = -\mathbf{h}_d\cdot\mathbf{m} > 0$ is a positive boundary source, that is, an inward flux.

The Initial-Boundary Value problem

The model is based on a system of bulk equations, describing the balance of forces and the balance of water concentration, coupled through the volumetric constraint (3.1.1), and the constitutive equations (3.1.8): on $\mathcal{B}_d\times\mathcal{T}$

$$0 = \mathtt{div}\,\mathbf{S}_d \quad \text{and} \quad \dot{c}_d = -\mathtt{div}\,\mathbf{h}_d\,, \tag{3.1.12}$$

with a dot denoting the time derivative and div the divergence operator. Equations (3.1.12) must be complemented with mechanical boundary conditions on the traction

$\mathbf{t}$ and/or displacement $\bar{\mathbf{u}}_d$:

$$\begin{aligned} \mathbf{S}_d\,\mathbf{m} &= \mathbf{t}\,, \quad \text{on } \partial_t\mathcal{B}_d \times \mathcal{T}\,, \\ \mathbf{u}_d &= \bar{\mathbf{u}}_d\,, \quad \text{on } \partial_u\mathcal{B}_d \times \mathcal{T}\,; \end{aligned} \tag{3.1.13}$$

and with chemical boundary conditions on solvent source q_s and/or concentration c_s:

$$\begin{aligned} -\mathbf{h}_d \cdot \mathbf{m} &= q_s\,, \quad \text{on } \partial_q\mathcal{B}_d \times \mathcal{T}\,, \\ c_d &= c_s\,, \qquad\quad \text{on } \partial_c\mathcal{B}_d \times \mathcal{T}\,. \end{aligned} \tag{3.1.14}$$

Notation $\partial_s\mathcal{B}_d$ with $s = t, u, q$ or c in the above equations denotes the portion of the boundary of $\mathcal{B}_d$ where traction $\mathbf{t}$, displacement $\bar{\mathbf{u}}_d$, solve source q_s, and concentration c_s are prescribed, respectively. Finally, the model is completed by the initial conditions for the state variables $\mathbf{u}_d$ and c_d:

$$\mathbf{u}_d = \mathbf{u}_{do}\,,\ c_d = c_{do}\,, \quad \text{on } \mathcal{B}_d \times \{0\} \tag{3.1.15}$$

Free swollen states

Hydrogel theory is able to predict free swollen states of hydrogels which are immersed into a bath of assigned chemical potential $\mu_{\text{ext}} = \mu_{\text{e}}$. In particular, these states are assumed to be stress-free $\mathbf{S}_d = 0$ and isotropic: $\mathbf{F}_d = \lambda_o\,\mathbf{I}$. Under these conditions, equations in (3.1.4) prescribe:

$$\mathcal{R}T\left(\log\frac{\lambda_o^3 - 1}{\lambda_o^3} + \frac{1}{\lambda_o^3} + \frac{\chi}{\lambda_o^3}\right) + \frac{G_d}{\lambda_o}\Omega = \mu_{\text{ext}}, \tag{3.1.16}$$

where λ_o identifies the uniform swelling ratio corresponding to a given shear modulus G_d once the external chemical potential μ_{ext} and the Flory parameter χ have been fixed. When $\lambda_o >> 1$ (that is, $1/\lambda_o << 1$), Eq. (3.1.16) can be approximated, by estimating the leading order term in the asymptotic expansion up to $O(1/\lambda_o^8)$, as

$$\lambda_o = \left(\frac{1/2 - \chi}{G_d}\right)^{1/5}, \tag{3.1.17}$$

corresponding to $\mu_{\text{ext}} = 0$

3.2 Shape control of hydrogels and osmotic pumps

The shape of hydrogels can be controlled through the composition of the hydrogel material or through not homogeneous boundary conditions. In particular, in the first case, expansion and bending can be obtained using materials composed of two layers with different stiffness. In this section we focus on the second case and we realize steady curved shapes from homogeneous hydrogel flat structure which are in contact with two environments at different chemical conditions. We numerically investigate the behavior of beam-like and plate-like structures during the transient state, which realize osmotic pumps. Through numerical experiments, we determine the relationship between the difference in the chemical potentials at the top and bottom of a beam and the curvature of the bent beam as well as the Gaussian curvature of a spherical cap morphed from a flat plate. We also propose an approximate modelling of both the beam and the plate, to evaluate explicitly that relationship and

show the good agreement between those formulas and the outcomes of the numerical simulations.

Hydrogels swell and contract in response to a wide range of environmental stimuli and, due to their properties, have been intensively studied as one of the most promising materials for multifunctional devices. On one side, there is a great choice both in the type of stimuli to employ and in the arrangements of material and geometric properties [76]. On the other side, the ability of hydrogels to elastically undergo large deformations and bifurcations widens the spectrum of attainable configurations and effects.

Bending strategy is one of the programming strategies that can be used for planning the morphing based on out-of-plane bending of hydrogel–based slender structures.

In thin hydrogel structures arranged in the form of composites which combine constituents with physical or chemical properties different one from each other, shape changes are triggered by the differential swelling of the constituents, combined with an interplay between geometry and mechanics, which may also involve stability issues. As for the bi-metal thermostats studied by Timoshenko, the curvature of a hydrogel–based bilayer strip can be programmed; in the latter case, through the control of the swelling ratios, which originate from different polymer composition [77–79]. Moreover, also complex shape transformations can be programmed by including additional control parameters into the programming strategy, such as oriented fiber fields which make anisotropic the material response of the hydrogels [80].

An alternative strategy to realize bending in hydrogel structures is based on a non–homogenous exposure of a homogeneous structure to an activation stimulus, as experienced in Ref.[81, 82]. This strategy allows to realize a transient gradient in swelling as the diffusion of the solvent inside the material takes time. As the diffusion is completed, a uniform swelling is attained through the material thickness, and bending is inhibited.

We implemented a different strategy, considering a homogeneous hydrogel structure which is in contact at its top and bottom faces with two environments at different chemical conditions, and is not permeable at its edges. Water diffuses into the hydrogel according to the opposite of the gradient of the chemical potential, so realizing an osmotic pump. Assuming that the chemical conditions of the two environments stay unchanged, diffusion never stops; at the steady state, a uniform water flux is attained through the material thickness, and a bent shape with uniform curvature is got. Homogeneous hydrogel beam–like structures realize curved shapes, whereas plate–like structures morph into spherical caps.

We numerically investigate the behavior of the beam-like and plate-like pumps during the transient state by means of a finite element implementation of the mathematical model. Through a series of numerical experiments, we determine the relationship between the difference in the chemical potentials at the top and bottom of the structure and the curvature of the bent beam as well as the Gaussian curvature of the spherical cap. We also propose an extension of the beam-like model presented by one of the Authors in Ref.[77], to evaluate explicitly that relationship and show the good agreement between those formulas and the outcomes of the numerical simulations. Finally, inspired by the geometrical issues presented in Ref.[83], and following the idea proposed in Ref.[84], we also evaluate the elastic energy corresponding to the spherical configuration attained by the plate and evaluate explicitly the Gaussian curvature of the spherical cap as the minimum of that energy. The comparison with the numerical outcomes shows that, when the difference in the chemical potentials

at the top and bottom of the structure is not too high, the explicit and the numerical solutions are in good agreement.

3.2.1 Swelling and de-swelling cycles

We are interested in steady solutions of the problem (3.1.12), that is, such that $\mathtt{div}\,\mathbf{h}_d = 0$, corresponding to constraints and load free boundaries, that is, $\mathbf{t} = \mathbf{0}$ on $\partial\mathcal{B}_d \times \mathcal{T}$, and induced by swelling paths. The goal is to investigate the relationship between the curving of an initially flat and dry hydrogel structure and the change in the environmental conditions around it.

We start considering a thin hydrogel structure $\mathcal{B}_d$, represented as a beam in its stress-free and dry state embedded into a dry environment in the cartoon in Fig. 3.1 (Fig. 3.1, top left). We change the chemical conditions of the environment by controlling the chemical potential on the bottom and top of the structure whereas assuming impermeable edges. So, the hydrogel may go from its flat dry to a flat fully wet state (Fig. 3.1, bottom right), when it is assumed as completely embedded in a homogeneously hydrated environment. Likewise, we can identify two curved steady states when the hydration conditions of the environment at the top and bottom of the beam are different (Fig. 3.1, top right and bottom left). In the last cases, the beam works as a pump draining water from the wet to the dry face of the beam.

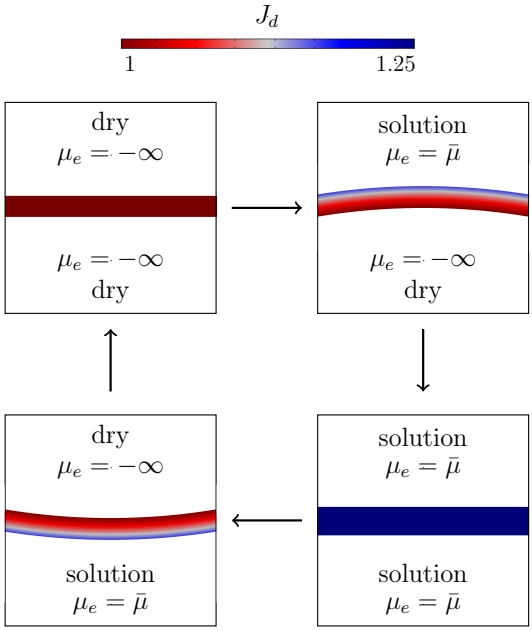

FIGURE 3.1: Cycle of hydration and de–hydration of a gel: a homogeneous straight beam is embedded in a dry environment (top left panel); due a change in the bath in contact with the top of the beam, it swells and attains a steady bent state (top left panel); a further change in the bath induces further swelling and a steady straight state is got (bottom right panel); a last change in the bath determines a swelling which brings the beam at a steady bent state with curvature opposite (bottom left panel). Colour code refers to J_d values. We assumed: $G_d = 10^8$Pa and $\bar{\mu} = 0$.

The modelling of the experiment is based on the theoretical background illustrated in the previous section. Key elements of the computational implementation are the tackling of the chemical boundary conditions (3.1.14), which also involve the assignment of an external chemical potential μ_e. Firstly, as it is not possible to control either the solvent source q_s at the surface or the surface concentration c_s, as is done in real experiments, we control the chemical potential μ_e of the bath. Equation (3.1.4), when evaluated at the boundary $\partial\mathcal{B}_c$, relates c_s to μ_e. It is a highly non–linear equation which cannot be solved explicitly for c_s. On the other hand, the control of the state variable c_s, through the equation $(3.1.14)_2$, forces the surface flux source q_s to be viewed as a unknown a priori reaction. The a posteriori evaluation of q_s yields poor approximations and suggested to us the following integral implementation of the boundary conditions ((3.1.14)):

$$0 = \int_{\partial_c\mathcal{B}_d} [\,\hat{\mu}(c_s) + p\,\Omega - \mu_e\,] \cdot \tilde{c}_s\,, \tag{3.2.18}$$

$$0 = \int_{\partial_c\mathcal{B}_d} [\,(c_d - c_s)\,\tilde{q}_s + q_s\,(\tilde{c}_d - \tilde{c}_s)\,]\,, \tag{3.2.19}$$

which enforce the constraint $c_d = c_s$ by considering q_s as an additional state variable, having the role of a Lagrange multiplier, and provides a better numerical evaluation of the boundary source q_s.

In the following analysis, some of the physical quantities are fixed and get the values shown in Table 3.1:

TABLE 3.1: Numerical values of the parameters

Parameter	Symbol and value
Dis-affinity	$\chi = 0.4$
Molar volume	$\Omega = 1.8 \times 10^{-5}\ \mathrm{m}^3/\mathrm{mol}$
Diffusivity	$D = 10^{-9}\ \mathrm{m}^2/\mathrm{s}$
Temperature	$T = 293\mathrm{K}$
length	$l = 1\mathrm{cm}$

3.2.2 Beam-like pumps

We consider a beam–like body whose aspect ratio is $h/l = 0.1$, being h its thickness and width and l its length. The surface boundary $\partial\mathcal{B}$ is composed by a top $\partial\mathcal{B}_t$ and a bottom $\partial\mathcal{B}_b$ permeable surfaces and by the edges which are not permeable: $q_s = 0$. We start from a dry state which is also stress-free and induce a swelling process through a change in the external conditions on the top surface. The corresponding steady state is a curved beam with constant curvature which works as a pump draining water from the top to the bottom surface. We assume to have infinite reservoirs in contact with the top and bottom surfaces; hence, we do not deal with any problems induced by the pump effect on a confined volume of water (see Ref.[85] for a detailed analysis of this kind of effects).

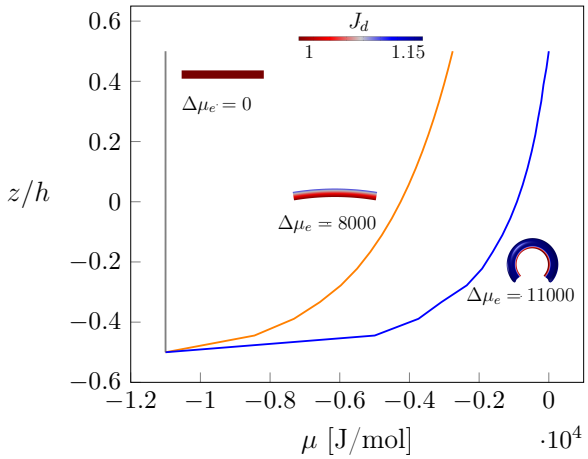

FIGURE 3.2: Pattern of the chemical potential μ across the thickness of the beam for different values of $\Delta\mu_{\text{ext}}$: higher $\Delta\mu_{\text{ext}}$ steeper the pattern and more bent the beam (see the insets). Colour code refers to values of J_d. We assumed: $G_d = 10^5$Pa.

Anyway, the analysis of the steady curved state shows a few interesting characteristics. As first, the driving force of the process is the mismatch $\Delta\mu_{\text{e}} = \Delta\mu_{\text{ext}} = \mu^t_{\text{ext}} - \mu^b_{\text{ext}}$ between the chemical potential's values at the top and bottom surfaces. We observe as increasing the mismatch makes the pattern of the chemical potential μ across the beam thickness steeper and steeper (Fig. 3.2). Moreover, due to the non uniformity of the deformation field across the thickness and to the constitutive equations (3.1.10) and (3.1.11), the pattern of μ across the thickness of the beam is never linear, as it is sometimes assumed in Literature [86].

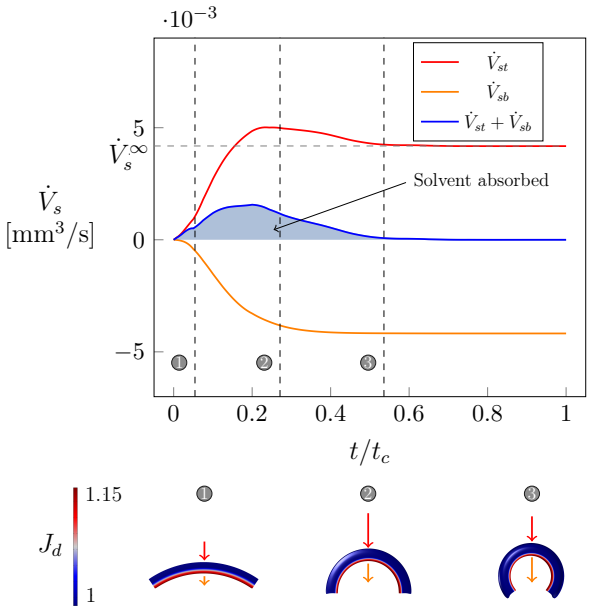

FIGURE 3.3: Amount of water crossing the top ($\dot{V}_{st}$) and bottom ($\dot{V}_{sb}$) surface per unit of time (solid red and orange lines) and absorbed into the beam (grey area) along the process. After a time $t < 0.6t_c$ the process is steady: the ingoing and outgoing fluxes are equal. We assumed: $G_d = 10^5$Pa.

Secondly, the intensity of the pump, which can be measured by the amount of water crossing the top or the bottom surface per unit of time

$$\dot{V}_s = \int_{\partial\mathcal{B}_t} q_s dA_d\,, \quad [\dot{V}_s] = m^3/s\,, \tag{3.2.20}$$

varies along the process. Fig. 3.4 shows as along the transient the two quantities are not the same: the ingoing (solid red line) and outgoing (solid orange line) fluxes are always opposite in sign at the top and bottom surfaces, respectively and, at any time t, the difference between the two quantities delivers the amount of water absorbed by the beam (grey area). At the steady state, the two fluxes are equal and the amount of absorbed water is zero; hence, the beam works just as an osmotic pump draining water from the top to the bottom. In representing the transient process (Fig. 3.4), it has been introduced a characteristic time t_c as $t_c = ((l+2h)/3)^2/D$ to evidence the duration of the transient part of the process with respect to the full time interval $t = t_c$.

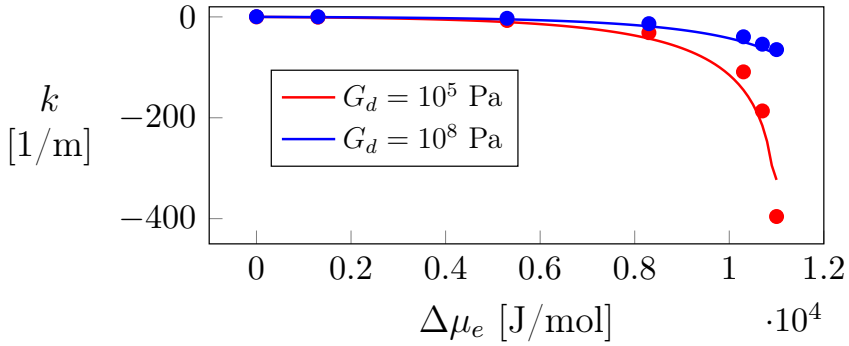

FIGURE 3.4: Beam curvature κ versus the mismatch $\Delta\mu_{\text{ext}}$ are represented as red and blue circle, depending on the value of the shear modulus. Red and blue solid lines represent the beam curvature corresponding to the same shear moduli as delivered by the explicit analysis presented in Section 3.2.4.

Finally, the steady configuration attained by the beam is characterized by a constant curvature which can be measured in terms of the mismatch $\Delta\mu_{\text{e}}$. Fig. 3.4 shows as higher is the mismatch, higher is the beam curvature (red and blue circles). Moreover, it also shows as softer beam (red circles) realizes higher curvature than stiffer beam (blue circles). Red and blue solid lines in Fig. 3.4 represent the beam curvature corresponding to the same shear moduli corresponding to red and blue circles, as delivered by the explicit analysis presented in Section 3.2.4. As the chemical potential in the numerical results is not strictly quadratic for a large mismatch $\Delta\mu_{\text{e}}$, a small discrepancy is observed the explicit expression.

3.2.3 Plate-like pumps

We consider a plate–like body whose aspect ratio is $h/l = 0.1$, being l the length of plate's sides, having the edges which are not permeable and the top $\partial\mathcal{B}_t$ and bottom $\partial\mathcal{B}_b$ faces which are permeable surfaces. We start from a dry state which is also stress-free and induce a process like the one described for the beam-like body. At the steady state, the flat sheet is dome-shaped, characterized by an almost constant Gaussian curvature K, and drains water from the top to the bottom surface.

The Gaussian curvature of the curved surface is represented in Fig. 3.5 (top panel) in terms of the mismatch $\Delta\mu_{\text{ext}}$ through the mean value $\bar{K}$ on the middle surface of the plate (blue circles) and the value $K^\star$ at the middle point of the middle plane (red diamonds). The two values are very close up to certain values of $\Delta\mu_{\text{ext}}$; then, they start going far one from each other and the difference between $\bar{K}$ and $K^\star$ increases with $\Delta\mu_{\text{ext}}$. Indeed, for large $\Delta\mu_{\text{ext}}$ we have a large stretching of the middle plane and the Gaussian curvature takes extremely high values on the boundary of the dome-like shape, which also loses its spherical symmetry, as Fig. 3.5 (bottom panel) shows through a colour code corresponding to the local value of K. The solid line in Fig. 3.5 (top panel) corresponds to the explicit solution presented in Section 3.2.4. At the steady state, the plate realizes shows a gradient of chemical potential μ across the thickness going from the bottom value (μ^b_{ext}, red) to the top value (μ^t_{ext}, blue) (Fig. 3.5 (middle panel)).

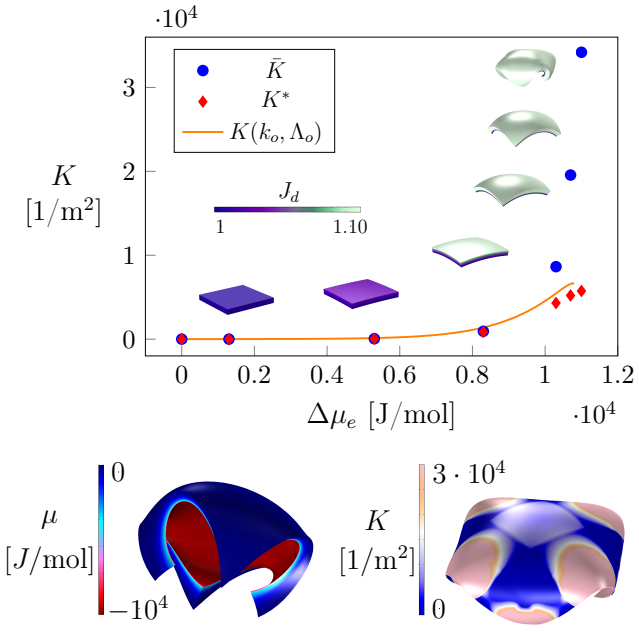

FIGURE 3.5: Steady curved shape of a square plate. We assumed: $G_d = 10^5$Pa.

3.2.4 Steady bending in homogeneous hydrogel beams and plates

We propose an approximate analysis of the steady solutions of the stress–diffusion problem of the homogeneous hydrogel beam borrowed from the study proposed for bilayered beams embedded in a homogeneous bath in Ref. [77] (see also Refs. [78, 79, 87]). Therein, bending was induced by embedding into a bath of assigned chemical potential $\mu_e = 0$ a bilayer beam made by two layers of different materials: the ratio $\beta = h_t/h$ between the thickness of the top layer and the beam thickness and the ratio $\alpha = G_t/G_b$ between the shear moduli of the two layers played a key role in the analysis. Only the longitudinal deformation λ of the beam was taken into account in the description of the bent state. It was multiplicatively decomposed in an uniform free–swelling ratio that would take place if the part were free from the rest of the beam and a further elastic component. In particular, the uniform free–swelling components of each part were determined from the appropriate mechano–chemical equilibrium equations as if the beam was made of two independent layers

free to swell as much as they like, according to the shear modulus. On its side, the elastic deformations resulted from the multiplicative decomposition once the global compatibility of the bending deformation has been ensured. These latter determined internal stresses corresponding, in the absence of external forces, to null forces and torques on each cross section of the beam. The analysis delivered a Timoshenko–like formula for the swelling-induced curvature κ of the beam axis, as well as a formula for the swelling-induced stretch Λ_o of the beam axis.

In the present problem, we have a homogeneous beam whose steady state is curved and characterized by a hydration level which isn't uniform across the thickness. As it is expected, the chemical potential is not homogeneous neither linear along the thickness (see Fig. 3.2), going from the value μ^b_{ext} at the bottom to the value μ^t_{ext} at the top. As described by the cartoon in Fig. 3.6, we identify two layers of thickness $h_t = \beta h$ (top layer) and $h_b = (1-\beta)h$ (bottom layer) where the chemical potential is constant and equal to the top and bottom values, respectively, by introducing the piecewise constant function

$$\mu_{cst}(x_3) = \begin{cases} \mu^t_e & \text{for} \quad h/2 - \beta h < x_3 < h/2 \\ \mu^b_e & \text{for} \quad -h/2 < x_3 < h/2 - \beta h \end{cases}$$

being $x_3 = 0$ the geometrical beam axis. The value of the parameter β which determine the two layers's thicknesses comes from the following identity

$$\int_{\mathcal{B}_d} \frac{\mu}{\Omega} dV = \frac{\mu^t_e}{\Omega} V_t + \frac{\mu^b_e}{\Omega} V_b \,, \tag{3.2.21}$$

being $V_t = \beta h L w$ and $V_b = (1-\beta) h L w$ the volumes of the top and bottom layer, respectively. Identity (3.2.21) says that the amount of work required to move all the volume of solvent from the top to the bottom face in the actual beam (left hand-side of identity (3.2.21)) is equal to the work done in the beam once assumed the chemical potential separately homogeneous in the two layers identified by the parameter β (right hand-side of identity (3.2.21))[2].

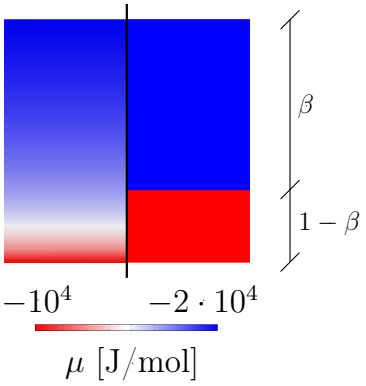

FIGURE 3.6: Chemical potential μ changes across the thickness from the bottom value μ^b_{ext} (red) to the top value μ^t_{ext} (blue) (left side of the cartoon). This distribution is replaced by one that is piecewise constant (right side of the cartoon).

[2]It is identified with the corresponding volume of the beam occupied by the solvent.

It can be written as

$$\int_{-h/2}^{h/2} \mu(x_3) dx_3 = \mu_e^t \beta\, h + \mu_e^b (1-\beta)\, h\,. \tag{3.2.22}$$

Inspired by the numerical results, we explicitly represent $\mu(x_3)$ by a quadratic function of x_3 as

$$\mu(x_3) = \mu_0 + x_3\mu_1 + x_3^2\mu_2\,, \tag{3.2.23}$$

in terms of the three scalars μ_0, μ_1, and μ_2 to be determined in such a way that

$$\mu(h/2) = \mu_e^t \quad \text{and} \quad \mu(-h/2) = \mu_e^b\,. \tag{3.2.24}$$

Moreover, being the solvent flux $\mathbf{h}_d = q\mathbf{e}_3$ constant, with $\mathbf{e}_3$ the unit vector indicating the vertical direction, we also set

$$q(h/2) = q(-h/2) = \bar{q}\,. \tag{3.2.25}$$

From equations (3.1.10) and (3.1.11), we get

$$q(x_3) = -\frac{D}{RT}\,\frac{c_d(x_3)}{\lambda_3^2(x_3)}\mu'(x_3)\,, \tag{3.2.26}$$

with λ_3 the stretch in direction $\mathbf{e}_3$. Equation (3.2.25) delivers

$$\left(\frac{c_d}{\lambda_3^2}\mu'\right)_{h/2} = \left(\frac{c_d}{\lambda_3^2}\mu'\right)_{-h/2}\,. \tag{3.2.27}$$

We assume that $\lambda_3(h/2) = \lambda_{ot}$ and $\lambda_3(-h/2) = \lambda_{ob}$, with $\lambda_{ot} = \lambda_{ot}(G, \mu_e^t)$ and $\lambda_{ob} = \lambda_{ob}(G, \mu_e^b)$ the swelling ratios which satisfy the equations:

$$\frac{G\Omega}{\lambda_{oi}} + RT\left(\log\left(1 - \frac{1}{(\lambda_{oi})^3}\right) + \frac{1}{(\lambda_{oi})^3} + \frac{\chi}{(\lambda_{oi})^6}\right) = \mu_e^i\,, \tag{3.2.28}$$

with $i = t, b$. Moreover, it also holds: $1 + \Omega c_d(h/2) = (\lambda_{ot})^3$, and $1 + \Omega c_d(-h/2) = (\lambda_{ob})^3$. With this, equation (3.2.27) prescribes the following further condition

$$\mu'(h/2) = C_o\,\mu'(-h/2)\,, \tag{3.2.29}$$

being

$$C_o = \frac{(\lambda_{ot})^2((\lambda_{ob})^3 - 1)}{(\lambda_{ob})^2((\lambda_{ot})^3 - 1)}\,. \tag{3.2.30}$$

this last condition is added to the first two conditions given by Eq. (3.2.24) allows to determine the unknown coefficients μ_i with $i = 0, 1, 2$. With this, Eq. (3.2.21) allows to determine β as

$$\beta = \frac{2 + C_o}{3(1 + C_o)}\,. \tag{3.2.31}$$

From now on, we view the homogeneous beam as a bilayer beam whose layers of thickness $h_t = \beta h$ and h_b are swollen up to a level determined by the chemical potential μ_e at the top and bottom face, as equation (3.1.16) prescribes: precisely, we have $\mu = \mu_e^t$ and $\mu = \mu_e^b$ in the top and bottom layer, respectively (see Fig. 3.6). As in Ref.[77], we assume that the longitudinal deformation $\lambda(x_3) = \Lambda_0(1 + x_3\Lambda_0\kappa)$ of the beam can be viewed as the product of the free-swelling ratio due to the hydration

level and an elastic component which deliver internal stresses. So, given the free-swelling ratios λ_{ot} and λ_{ob} above introduced, the corresponding elastic deformations $\lambda_{et} = \lambda\lambda_{ot}^{-1}$ and $\lambda_{eb} = \lambda\lambda_{ob}^{-1}$ are determined from the multiplicative decomposition in terms of Λ_o and κ.

Then, assuming zero out–of–plane stresses, the corresponding longitudinal stresses σ_t and σ_b on the cross–sections of the top and bottom layers, respectively, are evaluated as

$$\sigma_t(x_1, x_3) = 3G_d(\lambda(x_1, x_3)\lambda_{ot}^{-1} - 1)\,, \tag{3.2.32}$$

for $(h/2 - \beta h) < x_3 < h/2$; and

$$\sigma_b(x_1, x_3) = 3G_d(\lambda(x_1, x_3)\lambda_{ob}^{-1} - 1)\,, \tag{3.2.33}$$

for $-h/2 < x_3 < (h/2 - \beta h)$, where, due to the material incompressibility, $3G_d$ identifies the corresponding Young modulus.

We looked for free–swelling solutions of the gel beam problem: under no external loads, the resultant $F(\lambda_{ob}, \lambda_{ot})$ of the stresses and the resultant moment $M(\lambda_{ob}, \lambda_{ot})$ of the stresses on the gel beam have to be identically null, that is, it holds

$$F(\lambda_{ob}, \lambda_{ot}) = 0 \quad \text{and} \quad M(\lambda_{ob}, \lambda_{ot}) = 0\,. \tag{3.2.34}$$

Equations (3.2.34) deliver a linear systems of two equations in Λ_0 and $\Lambda_1 = \kappa\Lambda_0^2$ where, differently from the situation studied in Ref.[77], the parameter β is not geometrically but thermodynamically determined. Moreover, being the two layers of the beam made of the same material, the ratio α between the shear moduli of the two layers is 1 and the bending is driven by the mismatch $\Delta\mu_{\text{ext}}$. The solution delivers the beam stretching Λ_0 and curvature κ as the following functions

$$\Lambda_0 = \Lambda_0(\lambda_{ot}, \lambda_{ob}, \beta) \quad \text{and} \quad \kappa = \kappa(\lambda_{ot}, \lambda_{ob}, \beta)\,, \tag{3.2.35}$$

explicitly represented:

$$\Lambda_0(\lambda_{ot}, \lambda_{ob}, \beta) = (\beta^4\lambda_{ot}^3 + (\beta-1)^4\lambda_{ob}^3 + \beta(1-\beta)a(\beta)\lambda_{ob}^2\lambda_{ot} + \beta(1-\beta^3)\lambda_{ob}\lambda_{ot}^2)D(\lambda_{ot}, \lambda_{ob}, \beta)^{-1}$$

$$\Lambda_1(\lambda_{ot}, \lambda_{ob}, \beta) = -6\beta(\beta-1)\lambda_{ob}\lambda_{ot}(\lambda_{ob} - \lambda_{ot})(hD(\lambda_{ot}, \lambda_{ob}, \beta))^{-1}$$

$$\kappa(\lambda_{ot}, \lambda_{ob}, \beta) = \frac{\Lambda_1(\lambda_{ot}, \lambda_{ob}, \beta)}{\Lambda_0(\lambda_{ot}, \lambda_{ob}, \beta)}\,, \tag{3.2.36}$$

and

$$D(\lambda_{ot}, \lambda_{ob}, \beta) = \beta^4\lambda_{ot}^2 + (\beta-1)^4\lambda_{ob}^2 + \beta(1-\beta)d(\beta)\lambda_{ob}\lambda_{ot}, \tag{3.2.37}$$

where we set $a(\beta) = 3 + \beta(\beta-3)$ and $d(\beta) = 2\beta^2 - 2\beta + 4$. Given the relations

$$\mathcal{R}\,T\Big(\log\frac{\lambda_{om}^3 - 1}{\lambda_{om}^3} + \frac{1}{\lambda_{om}^3} + \frac{\chi}{\lambda_{om}^6}\Big) + \frac{G_d\Omega}{\lambda_{om}} = \mu_{\text{ext}}^m\,, \tag{3.2.38}$$

($m = b, t$), between the free-swelling stretches λ_{ot} and λ_{ob} and the top and bottom chemical potential μ_{ext}^t and μ_{ext}^b, and fixed μ_{ext}^b, equations (3.2.35, 3.2.36, 3.2.39 , 3.2.40) deliver $\Lambda_0(G_d, \Delta\mu_{\text{ext}})$ and $\kappa(G_d, \Delta\mu_{\text{ext}})$. Fixed the value $\mu_{\text{ext}}^b = -11000$ J/mol, the beam curvature is so evaluated starting from the value $\Delta\mu_{\text{ext}} = 0$ corresponding to $\mu_{\text{ext}}^t = -11000$ J/mol. It is represented by the solid lines in Fig. 3.4 for $G_d = 10^5$ Pa (red) and $G_d = 10^8$ Pa (blue); it can be appreciated the good agreement between

the explicit and the numerical solution which is excellent for values of $\Delta\mu_{\text{ext}}$ not too much high.

3.2.5 Cutting a beam out of the plate

As last step, we propose an explicit formula delivering the Gaussian curvature of the plate-like pump at the steady state. In this case, the body is modeled within the setting of non-Euclidean plates as a shell with its first and second natural fundamental forms. The first and second fundamental forms $\mathbf{a}$ and $\mathbf{b}$ contain all the information about lateral distances between points and local curvature, respectively; the natural forms $\bar{\mathbf{a}}$ and $\bar{\mathbf{b}}$ represent the lateral distances and curvatures that would make the sheet locally stress-free, and they are determined by the specific stimulus which in this case is the mismatch $\Delta\mu_{\text{ext}}$. Due to the differential isotropic expansion of the two layers due to the swelling, the lateral distances would like to stretch by a_o while the midplane would like to bend with a curvature b_o in every direction, and $\bar{\mathbf{a}}$ and $\bar{\mathbf{b}}$ have the following form:

$$\bar{\mathbf{a}} = a_o^2 \begin{pmatrix} 1 & 0 \\ 0 & 1 \end{pmatrix} \quad \text{and} \quad \bar{\mathbf{b}} = b_o \begin{pmatrix} 1 & 0 \\ 0 & 1 \end{pmatrix} . \tag{3.2.39}$$

It is not usually possible for a sheet to realize both natural forms, due to the Gauss-Codazzi-Mainardi equations, and this is the case of our plate which has to match different planes across the thickness which would like to swell according to a different value of the chemical potential. However, as a beam is able to adopt its natural shape with longitudinal axis stretch and curvature equal to Λ_0 and κ, respectively, without any need of satisfying additional constraints, we proceed by cutting a beam from the plate disk and by measuring its deformed shape. This will provide a straightforward way to evaluate the natural stretch and curvature of the disk [83, 84]:

$$a_o = \Lambda_0(G_d, \mu^b_{\text{ext}}, \Delta\mu_{\text{ext}}) , \quad b_o = \kappa(G_d, \mu^b_{\text{ext}}, \Delta\mu_{\text{ext}}) . \tag{3.2.40}$$

Assuming as usual for non-Euclidean plates, a Kirchhoff-Love energy density, the energy of the plate can be written as

$$\begin{aligned} \bar{\mathcal{U}} = &\int (\text{tr}(\mathbf{a} - \bar{\mathbf{a}})^2 + \text{tr}^2(\mathbf{a} - \bar{\mathbf{a}}))\sqrt{\bar{\mathbf{a}}}\, \text{d}A \\ &+h^2 \int (\text{tr}(\mathbf{b} - \bar{\mathbf{b}})^2 + \text{tr}^2(\mathbf{b} - \bar{\mathbf{b}}))\sqrt{\bar{\mathbf{a}}}\, \text{d}A , \end{aligned}$$

being $\bar{\mathcal{U}} = 8\mathcal{U}(1-\nu^2)/Eh$, E and μ the Young and Poisson moduli, and $\mathbf{a}$ and $\mathbf{b}$ the first and second fundamental forms of the midsurface of the deformed plate, respectively. We follow Ref.[84] and assume a metric with constant Gaussian curvature in Gaussian normal coordinates (see also Ref.[88]); we also assume that $\nu \simeq 1/2$ and $E \simeq 3G_d$. So, the total dimensionless energy for the square disk of side l is

$$\bar{\mathcal{U}} = \frac{1}{9} L^4 \Lambda_0^{-2} \int r^4 dA + h^2 A \Lambda_0^{-2} (L - \kappa)^2 , \tag{3.2.41}$$

being Λ_0 and κ given by the equation (3.2.35), and L the principal curvature of the sphere. Following Ref.[84], we also assumed that the Gaussian curvature can be approximated as

$$K = \det \mathbf{b} / \det \mathbf{a} \simeq \frac{L^2}{\Lambda_o^4} . \tag{3.2.42}$$

Minimization of the total energy $\bar{\mathcal{U}}$ with respect to L yields

$$\bar{L}^3 + \gamma^4(\bar{L} - \bar{\kappa}) = 0\,, \tag{3.2.43}$$

being $\bar{L} = Lh$, $\bar{\kappa} = \kappa h$, and

$$\gamma^4 = \frac{h^4}{\mathcal{S}^4}\,, \quad \mathcal{S}^4 = \frac{2}{9}\frac{1}{A}\int r^4 dA\,. \tag{3.2.44}$$

Moreover, it holds:

$$A = l^2\,, \quad \mathcal{S}^4 = \frac{56}{405}l^4\,, \quad \gamma^4 = \frac{405}{56}\frac{h^4}{l^4}\,. \tag{3.2.45}$$

Equation (3.2.43) can be solved explicitly and delivers $\bar{L} = \bar{L}(\kappa)$. From there, using the equation (3.2.42), we get

$$K = K(\Lambda_0, \kappa)\,, \tag{3.2.46}$$

which can be ultimately expressed in terms of the mismatch $\Delta\mu_{\text{ext}}$ using the equations (3.2.35, 3.2.36, 3.2.39 , 3.2.40). In Fig. 3.5, we represented the function $K(\Delta\mu_{\text{ext}})$, corresponding to a fixed value of $G_d = 10^8$ Pa. The agreement with the mean values of K as well as with the Gaussian curvature at the middle of the plate is good if the mismatch $\Delta\mu_{\text{ext}}$ does not grow too much. Indeed, for large $\Delta\mu_{\text{ext}}$ we have: (1) $\bar{K}$ and $K^\star$ differs a lot due to the large values attained by the Gaussian curvature on the corner of the plate; (2) the stretching of the mid-surface increases and the approximation (3.2.42) does not hold any more.

3.3 High power mechanisms and hydrogels

One of the main limits of hydrogels is the slowness of the diffusion process which depends on hydrogel size and often results in a low power mechanism [89]. In order to overcome such limitation which confines the applications of hydrogels, in this section we describe two power leverages which transform the low power mechanism into a a high power mechanism. The key to build a power leverage is the presence of a breaking factor which rapidly releases the energy stored in a system with a low power mechanism. The breaking factor can be realized using physics, chemistry or mechanics.

3.3.1 A high power mechanism through swelling and adhesion

In this subsection, it is briefly described a high power mechanism of a polyvinyl siloxane (PVS) solid, see Fig. 3.7, obtained through the competition between swelling and adhesion. The experiment was performed by myself at Boston University at the Mechanics of Slender Structures Lab under the supervision of Prof. D. P. Holmes; the solid is obtained by pouring into an acrylic mold the mixed Zhermack polyvinyl siloxane (PVS) elite double 32 base and catalyst. The liquid mixture solidifies in approximately 10 minutes and then it is removed from the acrylic mold. The PVS solid has a Young's modulus of approximately 1 MPa measured through a Instron Machine with a tensile test of a dog bone like shape. The shape of the solid is a beam of size $5 \times 1 \times 0.1$ cm, which is clamped at the right end with a glue on an acrylic substrate. A syringe filled with solvent Sigma Aldrich Hexane is used to wet the body from below on the acrylic substrate. The solvent diffuses into the solid and allows the storage of elastic energy in the beam in a slow dynamics which lasts for approximately 4 minutes. The produced bending works against the adhesion forces which take the beam in contact with the substrate. The breaking factor, which suddenly releases the stored elastic energy, is the rapid fracture of a thin layer of adhesive at the left of the beam. The compensation between the two effects, adhesion and swelling, realizes a self actuated catapult which throws a small weight of about 20 g more than 20 cm away from the object. The high acceleration of the beam is a fast dynamics and lasts for less than 1 seconds. Later on, due to the evaporation of the solvent, the solid turns back flat and ready to be reused after approximately 20 minutes. This latter phase is also often called relaxation and depends on the velocity of solvent evaporation which is in general more slow than the absorption velocity. The experiment was really hard to consistently reproduce due to the very complex interaction between the different physics of swelling and adhesion. Moreover, a further complication to the understanding of such mechanism is represented by the fast evaporation of the solvent which cannot be controlled quantitivaly. For this reason, an alternative high power mechanism is investigated in the next subsection.

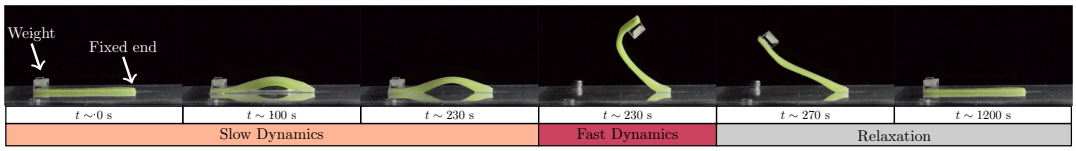

FIGURE 3.7: High power mechanism in a PVS beam clamped at right end. A syringe is used to wet the body on the acrylic substrate. The breaking factor is due to the compensation between the two effects: swelling and adhesion.

3.3.2 A high power mechanism through water cavitation

In this subsection, it is described and investigated a high power mechanism observed in small plants and obtained through water cavitation. Cavitation is the phase transition liquid-to-vapor which happens in water under negative pressure, that is, under tension, and at constant ambient temperature. It has been firstly studied, as of great interest, in some industrial contexts such as marine propellers [90], and petroleum industry [91]. Then, cavitation rheology has been studied with the aim to both determining the elastic modulus within a soft material through the quantification of the pressure dynamics of a growing cavity within the soft solid [92] and investigating the elasticity and fracture behavior of swollen polymer networks induced by cavitation [93].

In the last years, cavitation occurring in microscopic confinements has received great attention, being one of the processes exploited in nature to realize shooting mechanisms as prey capture, defense, and reproduction tools [94, 95]. Understanding the working principles of biological shooting mechanisms can drive the design of artificial shooting mechanisms realizing fast acceleration mechanisms. In medicine, high–speed shooting mechanisms can be implemented in endovascular treatments of calcified occlusions, the realization of pick-and-place applications as well as of high accuracy tools for biopsies [96].

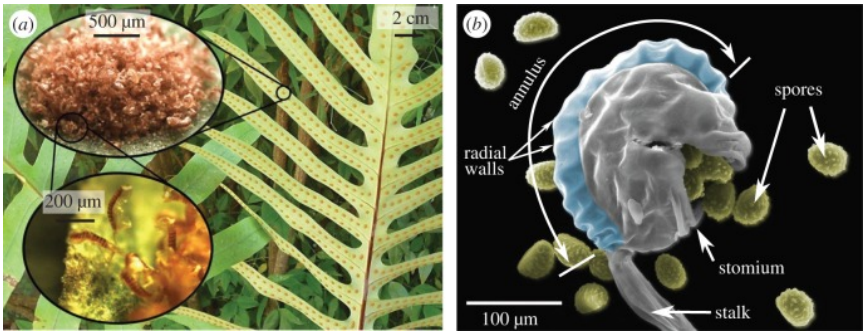

FIGURE 3.8: Fern sporangium is a small plant composed of cubic unit cells filled with water. The fern sporangium uses a high power mechanism to disperse the spores. Image taken by [97].

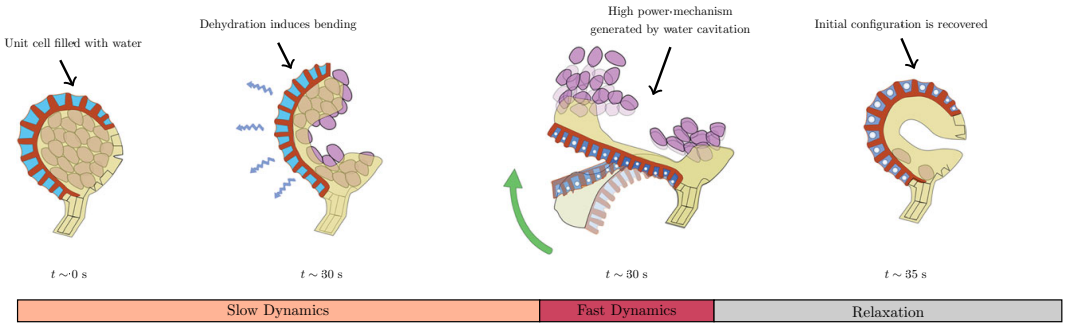

FIGURE 3.9: Due to the dehydration process, a slow mechanism starts: the water within the cavities is put in tension and the walls of the cavities undergo a not-homogeneous deformation process. When a threshold value of the water pressure is attained, water cavitation breaks the coupled mechanism and the elastic energy stored is rapidly released. Adapted image taken by [97].

In Ref. [94], the dynamics of spontaneous or triggered cavitation inside water–filled micro–cavities of a hydrogel have been studied through the analysis of the stability of water under tension in experiments at constant tension and controlled humidity (see also references therein). Water-filled micro-cavities are the elementary units of fern sporangium which uses the cavitation induced by evaporation of the water to realize the shooting mechanism allowing for seeds dispersal, see Fig. 3.8. This shooting mechanism, described and discussed in Ref. [95], is composed of two phases: a slow opening phase driven by water evaporation which ends when cavitation pressure is attained within the micro-cavities; a fast closing phase triggered by water cavitation, see Fig. 3.9. The dynamics of the fern sporangium has been deeply studied, following optically the opening and closing of sporangia, computing the deformations of the annulus during the two phases, and interpreting the dynamics in terms of a one-dimensional beam model which is shown to finely capture the characteristics of the motion.

Results in Ref. [97] highlight the importance of the precise tuning of the parameters which allow the lepto sporangium to work as a catapult. Likewise, it is important to discuss and investigate through appropriate models the role of the key geometrical and material parameters allowing for the attainment of cavitation pressure in water-filled micro-cavities of a hydrogel. To do it, the de-hydration process of a hydrogel cavity, initially filled with water, exposed to air has to be modeled. The model has to take into account the pumping induced by the difference in chemical potential inside and outside the cavity, as well as the suction effect realized by the cavity walls during the evaporation phase.

Actually, few studies are available which combine the fully nonlinear and transient mechanics of hydration and de-hydration processes with the extreme deformations which characterize hydrogels behavior. The problem has been addressed in Ref. [98], with reference to a hydrogel sphere which swell once embedded in a water bath and shrink once taken out of the bath. Some of the Authors have been involved in the investigation of hydration and dehydration processes in hydrogels for many years, and have elaborated a multiphysics model to describe such phenomena from a dynamics point of view which has been successfully tested in different situations [66, 67, 99].

Here, we deal with the following model experiment: a free-swollen hydrogel, having a cavity filled with water, is pulled out from the bath and exposed to air. The difference in chemical potential drains the water out of both cavity and gel walls, and a drying process begins. We study the dynamics of the dehydration process, identifying a transient phase dominated by an *inflatable-balloon* deformation mode, followed by a phase dominated by a *suction effect*, which determines highly not homogeneous deformation modes of the hydrogel. This phase triggers negative pressures into the cavity up to the typical values of water cavitation. This latter strongly depends on the geometry of the cavity, as well as on the shear modulus of the hydrogel. An analysis of the factors allowing to get cavitation pressure inside the cavity is proposed, to allow for precise tuning of the key geometrical and material parameters.

The time–dependent stress–diffusion problem described above allows to investigate both hydration and dehydration, which cause swelling and de–swelling, respectively. The latter process has received little attention in the Literature, even if it can induce noteworthy phenomena as the one we are studying here. Let us start by considering an ideal experiment. A dry hydrogel $\mathcal{B}_d$, with an inner cavity $\mathcal{C}_d$, is

immersed into a water bath in absence of constraints and loads, and kept there until both the hydrogel walls and the cavity are completely filled with water[3] At this point, the hydrogel is in a steady, stress-free state $\mathcal{B}_o$, with cavity $\mathcal{C}_o$; it is then taken out of the bath and exposed to air: dehydration begins, and water is expelled from both the cavity and the gel walls (Fig. 3.10).

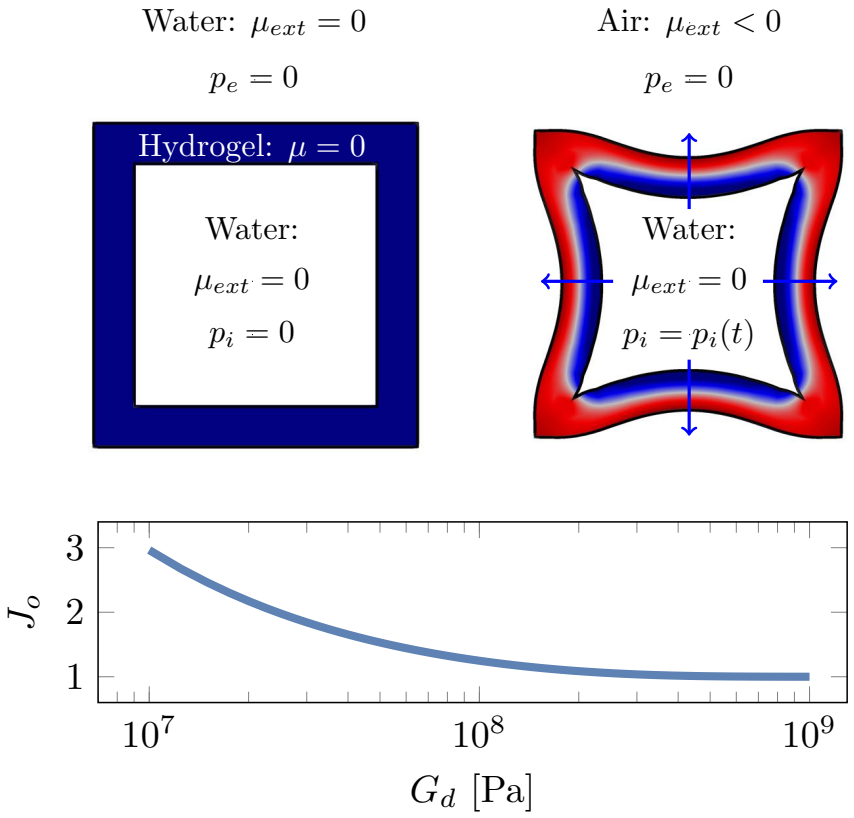

FIGURE 3.10: Top: A hydrogel cube with a cavity sits into a bath, in a free-swollen, steady state; the cavity is completely filled with water (left). The same hydrogel is pulled out and exposed to air: dehydration begins and water is pumped out of the cavity by the difference in chemical potential. As water content of the cavity reduces, the walls experience a suction pressure which yields an inward bending (right). Bottom: Free-swelling volume J_o versus shear modulus G_d for an external chemical potential $\mu_{\text{ext}} = 0\,\text{J/mol}$ (see Table 3.2 for parameters value).

3.3.3 Modelling dehydration

Here, we are interested in the dynamics of the dehydration process, that is, in describing the actual configuration of the gel $\mathcal{B}_\tau$, and of its cavity $\mathcal{C}_\tau$, during the time evolution:

$$\underbrace{\mathcal{B}_d\,,\,\mathcal{C}_d}_{\text{dry-reference state}} \quad \rightarrow \quad \underbrace{\mathcal{B}_o\,,\,\mathcal{C}_o}_{\text{free-swollen state}} \quad \rightarrow \quad \underbrace{\mathcal{B}_\tau\,,\,\mathcal{C}_\tau}_{\text{dehydration dynamics}} \tag{3.3.47}$$

[3]We can imagine cube, with a cubic cavity, and a cut open face; the cube is immersed into a bath until it is fully swollen. Then, the cut is sealed, and the swollen cube, with its cavity filled with water is put in open air and let dehydrate.

As well described in Literature (see Refs. [95–97]), the volume of the cavity has to match the volume of the water it contains: as water is pumped out, the volume of the cavity reduces, a suction pressure develops, and the hydrogel walls slowly bend inward. Correspondingly, elastic energy is stored into the walls. The suction effect, due to the water incompressibility, yields a negative pressure in the water, that is, a tension; eventually, if water tension reaches a critical value (in the range minus $9 \sim 20$ MPa) relative to the ambient pressure, cavitation can occurs: the formation of vapor bubbles in the cavity suddenly increases the volume occupied by water, yielding a jump of the suction pressure: hydrogel walls quickly release all the elastic energy previously stored. This whole process can be viewed as a power amplifier: chemical energy is used to slowly increase the elastic energy of the gel, a low-power process; then, this elastic energy is rapidly converted in kinetic energy and dissipated, a high-power process. This point of view has been illustrated in Ref.[95] and largely reviewed in Ref.[96]; water cavitation is the breaking factor that switches the slow process to the fast one. Being interested in dehydration, we consider as initial configuration the swollen, stress-free, steady state $\mathcal{B}_o$: with zero loads, no constraints, and an external chemical potential $\mu_{\text{ext}} = \mu_{\text{ext}}$, the mechanical and chemical balance laws prescribe $\mathbf{S}_d = \mathbf{0}$, $\mu = \mu_{\text{ext}}$, and yield a uniform deformation $\mathbf{F}_d = \mathbf{F}_o = \lambda_o \mathbf{I}$. The stretch λ_o is characterized by the value μ_{ext} of the bath's chemical potential and yields relation showed in equation (3.1.16). The relationship between λ_o (or $J_o = \lambda_o^3$) and G_d given by the equation (3.1.16) is represented for $\mu_{\text{ext}} = 0$ in Fig. 3.10 (bottom); it shows as the initial conditions change, depending on the shear modulus of the hydrogel, once all the other parameters have held fixed. Equation (3.1.16) is also used to set the initial conditions (3.1.15) specific to our problem[4]:

$$\mathbf{u}_o = (\lambda_o - 1)\, x\,, \quad c_d = c_{do} = \frac{J_o - 1}{\Omega}\,, \quad \text{on } \mathcal{B}_{\text{d}} \times \{0\}\,. \tag{3.3.48}$$

The deformation from $\mathcal{B}_o$ to the actual state $\mathcal{B}_t$ is then described by the deformation gradient $\mathbf{F} = \mathbf{F}_d\, \mathbf{F}_o^{-1}$.

As regards mechanical boundary conditions, we consider a steady uniform pressure p_e on the external boundary $\partial_e \mathcal{B}_d$, and a time-varying pressure p_i on the internal boundary $\partial_i \mathcal{B}_d = \partial \mathcal{C}_d$, with $\partial \mathcal{C}_d$ the boundary of the cavity; in terms of reference stress, we have

$$\begin{aligned} \mathbf{S}_d\, \mathbf{m} &= -p_e\, \mathbf{F}_d^{\star}\, \mathbf{m}\,, \quad \text{on } \partial_e \mathcal{B}_d \times \mathcal{T}\,, \\ \mathbf{S}_d\, \mathbf{m} &= -p_i\, \mathbf{F}_d^{\star}\, \mathbf{m}\,, \quad \text{on } \partial \mathcal{C}_d \times \mathcal{T}\,. \end{aligned} \tag{3.3.49}$$

The external pressure p_e describes the effect of the atmospheric pressure, and we assume as base value $p_e = 0$ Pa. The internal pressure $p_i = p_i(t)$ is a key element in our problem, and arises as reaction to the volumetric coupling between the water volume $v_w = v_w(t)$, and the cavity volume $v_c = v_c(t)$. As water flows out of the cavity it must hold

$$v_c(t) = v_w(t) \tag{3.3.50}$$

at each instant $t \in \mathcal{T}$, until cavitation. The global constraint (3.3.50) is enforced by adding a term to the total relaxed free-energy ψ_r:

$$\text{Potential Energy} = \int_{\mathcal{B}_d} \psi_r\, dV - p_i\, (v_c - v_w)\,; \tag{3.3.51}$$

thus, p_i can be viewed as the Lagrange multiplier enforcing the constraint (3.3.50).

[4]The initial condition for $\mathbf{u}_d$ assumes that the cubic region $\mathcal{B}_d$ is centered at the origin.

The cavity volume v_c depends on the actual configuration of the gel, described by the displacement $\mathbf{u}_d$, and can be evaluated as

$$v_c(t) = \int_{\mathcal{C}_t} dv = \frac{1}{3}\int_{\partial\mathcal{C}_t} x \cdot \mathbf{n}\, da = \frac{1}{3}\int_{\partial\mathcal{C}_d} (X_d + \mathbf{u}_d) \cdot \mathbf{F}_d^\star\, \mathbf{m}\, dA_d\,. \tag{3.3.52}$$

On the other hand, the water volume v_w equals the initial water content v_{wo}, minus the volume $v_w^i(t)$ of water outflown through the inner boundary, that is, that has left the cavity during the time interval $(0, t)$:

$$v_w(t) = v_{wo} - v_w^i(t)\,. \tag{3.3.53}$$

The initial water content equals the initial cavity volume $v_{co} = v_c(0)$, and is given by (3.3.52), evaluated at time $t = 0$:

$$v_{wo} = v_{co} = v_c(0) = \frac{1}{3}\int_{\partial\mathcal{C}_d} (X_d + \mathbf{u}_o) \cdot \mathbf{F}_o^\star\, \mathbf{m}\, dA_d\,. \tag{3.3.54}$$

To evaluate the volume v_w^i of the water that has left the cavity, we have at our disposal its time-rate $\dot{v}_w^i$ as $q_s = -\mathbf{h}_d \cdot \mathbf{m}$ measures the water flux entering the gel through the boundary. It follows

$$\dot{v}_w^i(t) = \int_{\partial\mathcal{C}_d} q_s\, dA_d = -\int_{\partial\mathcal{C}_d} \mathbf{h}_d \cdot \mathbf{m}\, dA_d\,. \tag{3.3.55}$$

Eventually, by time-integrating $\dot{v}_w^i(t)$, with initial condition $v_w^i(0) = 0$, yields the function $v_w^i(t)$. It is worth noting that both v_c and v_w depend on the state of the gel, that is, on the two state variables $\mathbf{u}_d$, c_d, which were coupled as a consequence of (3.1.1). Hence, the new global constraint (3.3.50) adds a further coupling, through the inner pressure p_i.

As regards the chemical boundary conditions, we use different values for the external chemical potential μ_{ext}, at the inner and the outer boundary of the gel:

$$\mu_{\text{ext}} = \mu_w \text{ on } \partial\mathcal{C}_d\,, \quad \text{and} \quad \mu_{\text{ext}} = \mu_a \text{ on } \partial_e\mathcal{B}_d\,, \tag{3.3.56}$$

being $\mu_w = 0$ J/mol a constant value at the surface in contact with water, and $\mu_a = \mu_a(t)$ a time varying value at the surface being exposed to air (see Fig. 3.7, top). The hypothesis of a constant μ_{ext} on $\partial\mathcal{C}_d$ holds until the inner pressure can be considered low. Indeed, $\mu_{\text{ext}} = p_i\Omega \approx 0$ on $\partial\mathcal{C}_d$ for $10^7 < G_d < 10^8$. To model the transient time interval during which the outer boundary condition changes from water to air, we assume the following time law for μ_a:

$$\mu_a(t) = \mu_o + (\mu_\infty - \mu_o)(1 - \texttt{exp}[-\texttt{log}\,2\,(t/T_c)])\,, \tag{3.3.57}$$

with $\mu_o = 0$ J/mol, corresponding to Relative Humidity (RH) equal to 1, and $\mu_\infty \ll \mu_o$, corresponding to RH $\ll 1$; T_c is the time needed to go from μ_o to $(\mu_o + \mu_\infty)/2$. In our numerical experiments we use the following values of the materials parameters:

TABLE 3.2: Numerical values of the parameters

Parameter value	IS Units	Description
$\Omega = 1.8 \cdot 10^{-5}$	m^3/mol	water molar volume;
$\chi = 0.2$	1	dis-affinity;
$D = 10^{-9}$	m^2/s	diffusivity;
$\mu_\infty = -2000$	J/mol	chemical potential for air ($J_\infty \simeq 1$);
$Tc = 500$	s	time to switch wet-to-dry;
$T = 293$	K	ambient temperature.

3.3.4 Dehydration dynamics

We consider as dry-reference $\mathcal{B}_d$ a cube with side length l, having a cubic cavity $\mathcal{C}_d$ at its center with side length $l - h$, so that the gel walls have thickness $h/2$.

To discuss dehydration dynamics we introduce the following volume ratios, whose time behavior is shown in Fig. 3.11:

- $v_w^i(t)/v_{co}$ water through the inner boundary;
- $v_w^e(t)/v_{co}$ water through the external boundary;
- $v_g(t)/v_{co}$ gel volume: $v_g = \int_{\mathcal{B}_d} J_d \, dV$;
- $v_w(t)/v_{co}$ water content of the cavity.

We also remember that water flux is measured with respect to the gel, that is, positive values of v_w^i and v_w^e represent water entering the gel.

Let $t_c = h^2/4D$ be the characteristic time of the diffusion problem. At early times, that is for $t/t_c << 1$, when hydrogel begins to release water from the external walls towards the environment, we have the highest gradients of chemical potential. The small, steep, ramp at the beginning of the curve $v_w^e(t)/v_{co}$ (yellow line) corresponds to a large negative flux (water exits from the walls); during the same time interval, the water entering the gel from the cavity is much smaller, $\|v_w^i(t)/v_{co}\| \ll \|v_w^e(t)/v_{co}\|$, the water content in the gel decreases very fast, and so does the gel volume, $v_g(t)/v_{co} < 1$ (steep initial ramp of the green line); meanwhile, the cavity volume remains almost unchanged, $v_w(t)/v_{co} \simeq 1$ (red line).

As a consequence, the inner pressure p_i increases up to a maximum positive value (Fig. 3.11, top panel), and we observe a sort of inflatable–balloon effect of the cavity which is especially visible under certain conditions, as we are discussing in the next subsection.

The pink region in Fig. 3.11 and 3.12, labeled I, identifies this phase of the dehydration, characterized by a positive inner pressure p_i and the inflatable–balloon deformation mode. This mode is represented with a cartoon in Fig. 3.12 (bottom panel, left), where coloring corresponds to the value of $J = J_d/J_o$, the ratio between the current and the free-swollen volume of the hydrogel.

After this initial transient, when $t/t_c > 1$, the gel volume $v_g(t)/v_{co}$ remains almost constant, see green line in Fig. 3.11, as the water entering into the gel from the cavity (blue line) is equal to water exiting the gel from the external boundary (yellow line).

The gray region in Fig. 3.11 and 3.12, labeled II, identifies the second phase of the dehydration, during which the inner pressure p_i has negative values, thus yielding the suction effect. During this phase, the hydrogel walls bend inwards, and the

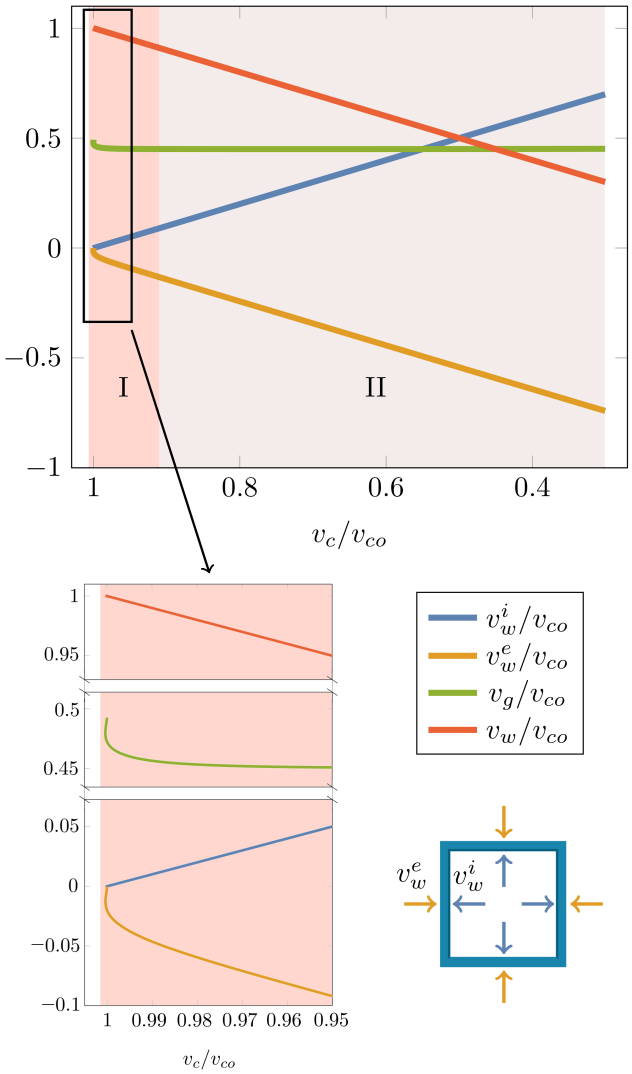

FIGURE 3.11: Top: Volume ratios of different quantities versus the dimensionless cavity volume v_c/v_{co}: volume of water crossing the internal boundary, v_w^i/v_{co} (blue); volume of water crossing external boundary v_w^e/v_{co} (yellow); gel volume v_g/v_{co} (green); water content of the cavity v_w/v_{co} (red). We set: $G_d = 10^8$Pa, $h = 0.0025$m, $l = 0.02$m; at $t = 0$, cavity volume is twice the gel volume.

water inside the cavity undergoes tension; this effect is represented with a cartoon in Fig. 3.12 (bottom panel, right).

3.3.5 Flow rates

A better view of the dehydration process can be obtained through the analysis of the fluxes and the pressure versus the cavity volume, as shown in Fig. 3.13; here phase I is larger than phase II, due to the smaller value of the shear modulus that has been used ($G_d = 10^7$ Pa) with respect to the one used for Fig. 3.12 to better discuss the process.

It can be noticed that the external flow rate $\dot{v}_w^e$ (yellow line) begins with a very high negative value: a lot of water exits from the gel towards the external; at the same time, the internal flow rate $\dot{v}_w^i$ (blue line) has a much smaller negative value:

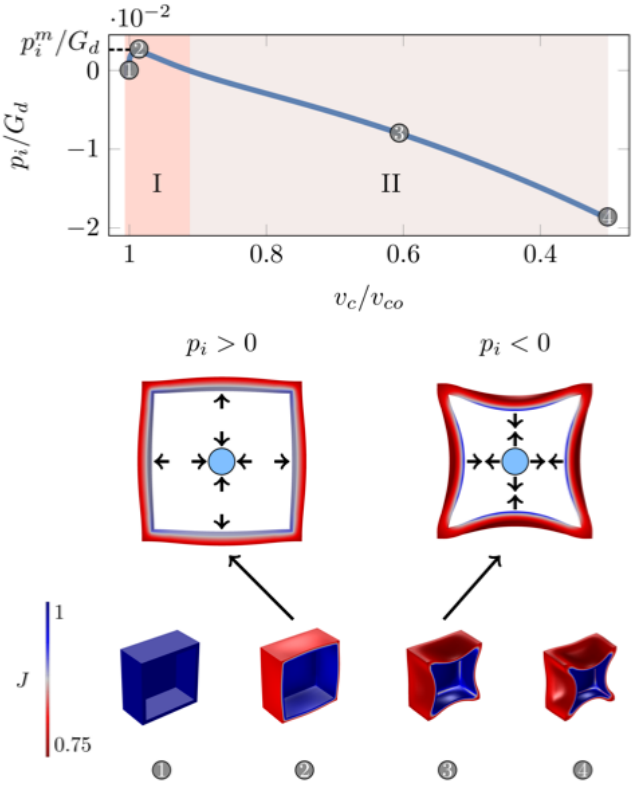

FIGURE 3.12: Top: Dimensionless inner pressure p_i/G_d versus cavity volume v_c/v_{co}; cavity pressure changes sign from positive in phase I to negative in phase II. At point 2, the pressure has its maximum, denoted as p_i^m. Middle: Gel configurations under positive (left) and negative (right) inner pressure. Bottom: Gel configurations at the four points $1-2-3-4$ highlighted in the top plot; coloring according to the gel-volume variation J. We set: $G_d = 10^8$ Pa, $h = 0.0025$ m, $l = 0.02$ m.

few water exits from the gel towards the cavity. Pressure (green dashed line) is positive and the inflatable–balloon effect takes place; when the two flow rates approach the same absolute value, $\|\dot{v}_w^e\|/\|\dot{v}_w^i\| \to 1$, the inner pressure crosses the zero value and becomes negative: the suction effect begins.

The cartoon at the bottom of Fig. 3.13 shows four different configurations corresponding to the points reported in the above plot. Configuration 1: very early times; $\dot{v}_w^e < \dot{v}_w^i < 0$; hydrogel walls are releasing water towards both the external environment and the inner cavity; pressure is positive and inflation begins. Configuration 2: early times; $\dot{v}_w^e < 0 < \dot{v}_w^i$; water exits from the cavity and from the external boundary, while $p_i > 0$; inflation persists. Configuration 3: flow rate are almost equal, but opposite in sign: $\|\dot{v}_w^e\|/\|\dot{v}_w^i\| \to 1$; pressure is almost zero. Configuration 4: inward flow rate from the cavity remains slightly higher than the outward flow rate to the external environment; $|\dot{v}_w^i| > |\dot{v}_w^e|$; pressure becomes negative; suction begins.

All in all, the flow rate from the cavity $\dot{v}_w^i$ depends on the geometrical characteristic of the cubic sample. In particular, our cube with edge length $= l$ and walls thickness $= h/2$, has external faces with area $A_e = l^2$, and cavity faces with area $A_c = (l-h)^2$; the ratio $a_\beta = A_e/A_c$ has a key role. Given the slenderness ratio $\beta = h/l$, it holds $a_\beta = 1/(1-\beta)^2$. We tested values for $\beta \in (1/8, 1/2$, that is, from thin wall and large cavity ($\beta \sim 1/8$), to thick wall and small cavity ($\beta \sim 1/2$), yielding a_β in the range $(1.3, 4)$. As expected, see Fig. 3.14, $\dot{v}_w^i$ is a decreasing function of

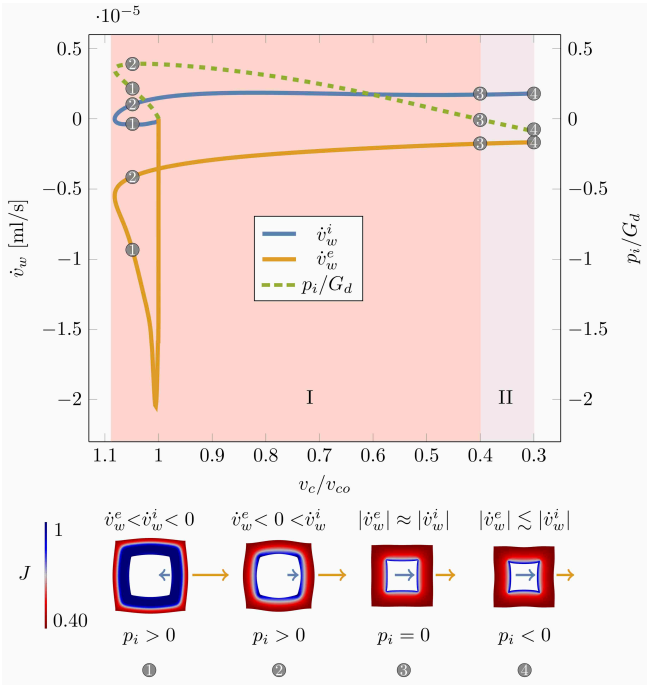

FIGURE 3.13: Top: Flow rates $\dot{v}_w^i$ (blue, solid) and $\dot{v}_w^e$ (yellow, solid) of water crossing the cavity boundary, and the external boundary, respectively; values are reported on the left vertical axis. Dimensionless pressure p_i/G_d (green, dashed) inside the cavity; values are reported on the right vertical axis. Bottom: Gel configurations corresponding to the four points highlighted on the above plot. The arrows show flow rates; coloring according to the gel-volume variation J. We set: $G_d = 10^7$ Pa, $h = 0.0025$ m, $l = 0.005$ m.

a_β and is lower for stiffer hydrogels (green lines) than for softer hydrogels (orange and blue lines); these values correspond to the instant $\bar{\tau}$ when, for each different sample, the cavity volume is half the initial size: $v_c(\bar{\tau})/v_{co} = 1/2$.

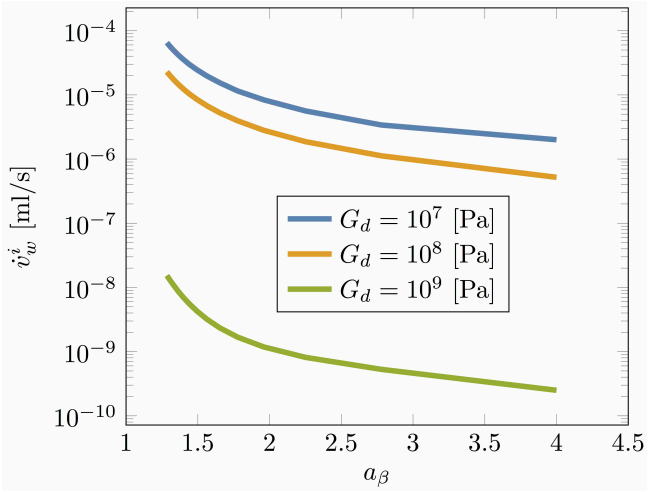

FIGURE 3.14: Semi-log plot of the flow rate through the boundary of the cavity $\dot{v}_w^i$, evaluated when $v_c/v_{co} = 1/2$, versus the surface ratio a_β. The three curves refer to different shear moduli, ranging from $G_d = 10^7$ Pa to $G_d = 10^9$ Pa (semi–logarithmic scale).

3.3.6 Elastic energy and stress

Finally, we discuss the evolution of two mechanical quantities, the elastic energy and the stress state, by comparing the behavior of gels having different shear moduli. During dehydration, a large part of elastic energy should be stored as a conse-

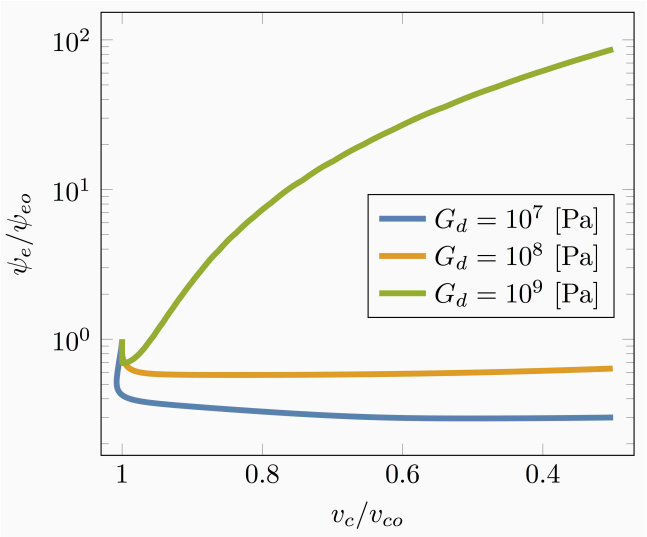

FIGURE 3.15: Dimensionless elastic energy ψ_e/ψ_{eo} versus v_c/v_{co} for different shear moduli spanning three orders of magnitude. We set: $h = 0.0025$ m, $l = 0.02$ m.

quence of the suction–effect deformation mode, that eventually yields a cavitation pressure inside the cavity[5]. In Fig. 3.15 we plot the evolution of the dimensionless elastic energy ψ_e/ψ_{eo}, with ψ_{eo} the elastic energy stored at the free-swollen state. We observe that, for a stiff material (green lines), the function ψ_e/ψ_{eo} is non–monotonic: at early times elastic energy decreases; then, at later times, it increases much more with respect to the previous loss. For softer hydrogels, the elastic energy behaves differently (orange and blue lines): most of its change happens at early times, with the consequence that the change of elastic energy during the process is much smaller with respect to the one seen for stiff gels.

To analyze the stress state, we focus on a beam-like portion of the gel's wall, that is, we consider a region at the center of a cube face, having length $(l - h)$ and cross section $h/2 \times h/2$ (see cartoon at bottom of Fig. 3.16). Denoted with $\mathbf{e}$ the direction of the longitudinal axis of the beam, we are interested in the longitudinal component $\sigma = \mathbf{T}\,\mathbf{e} \cdot \mathbf{e}$ of the Cauchy stress

$$\mathbf{T} = J_d^{-1}\mathbf{S}_d\,\mathbf{F}_d^T = \frac{G_d}{J_d}\mathbf{F}_d\,\mathbf{F}_d^T - p\,\mathbf{I}\,, \tag{3.3.58}$$

which is the stress component important for the bending. In Fig. 3.16, we plot the evolution of the dimensionless stress σ/G_d evaluated at a point of the external wall (solid lines), and of the internal wall (dashed lines). The stress analysis is interesting for two reasons. Firstly, it shows as stiff hydrogels (green) have a stress distribution in accordance with the suction–effect mode (stress is negative at outside, and positive at inside), whereas soft gels (orange lines) presents an inversion of the bending

[5]In Ref.[95], it has been noted as an array of cells, each undergoing a suction–effect deformation mode, exhibits a global bending deformation.

couple when deformation mode switches from the inflation–balloon (positive at outside, and negative at inside) to the suction–effect (negative at outside and positive at inside). Even softer hydrogels (blue lines) only presents bending stresses compatible with the inflation–balloon mode. Moreover, in these latter softer hydrogels, bending stress attains a very high values at early times.

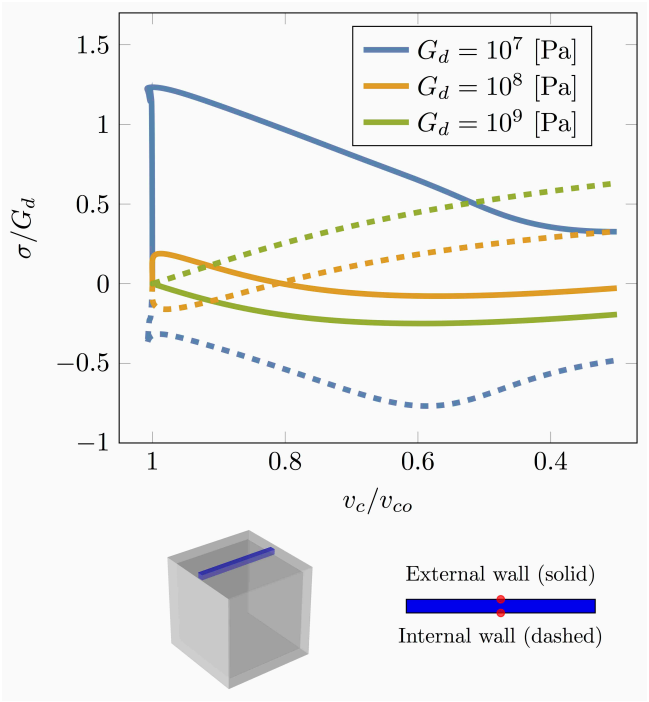

FIGURE 3.16: Top: Dimensionless bending stresses σ/G_d versus v_c/v_{co} for different shear moduli. Values taken at the external side (solid lines), and the internal side (dashed lines) of the cross section. Bottom: cartoon of the cubic sample with the beam-like region highlighted in blue (left), and the points used to evaluate the stress in red (right). We set: $h = 0.0025$ m, $l = 0.02$ m.

3.3.7 The inflation–balloon effect

At the best of our knowledge, the inflatable–balloon mode observed at early times has never been noted in the Literature. This phenomenon strongly depends on G_d, χ, μ_∞, β and the ratio T_c/t_c; in particular, by controlling T_c, the inflation effect can be enhanced or diminished. To quantify the effect of T_c/t_c and G_d, we fixed the aspect ratio $\beta = 0.125$ of the cubic sample, the external chemical potential $\mu_\infty = -2000$ J/mol, and we studied the dependence of the maximum inner pressure p_i^m, made dimensionless by G_d (see point 2 in Fig. 3.8), on T_c/t_c and on G_d. It is worth noting that, being μ_{ext} fixed, from equation (3.1.16) $J_o = J_o(G_d)$; thus, in the plot we report the values of J_o instead of G_d. Fig. 3.17a shows p_i^m/G_d versus J_o. The inflatable–balloon mode increases with J_o, and becomes appreciable when $J_o > 2$; moreover, the same effect is hampered for $T_c > t_c$ (yellow). Indeed, only when $T_c < t_c$ (blue), the water begins to outflow from the external boundary faster with respect to the water entering in the gel from the cavity: thus, the shrinking walls have to be stretched in order to wrap the water volume in the cavity which is still large. Fig. 3.17b shows p_i^m/G_d versus T_c/t_c. The curves show two regimes: for $T_c/t_c < 2 \cdot 10^{-1}$, pressure remains constant; for $T_c/t_c > 2 \cdot 10^1$ pressure decreases linearly

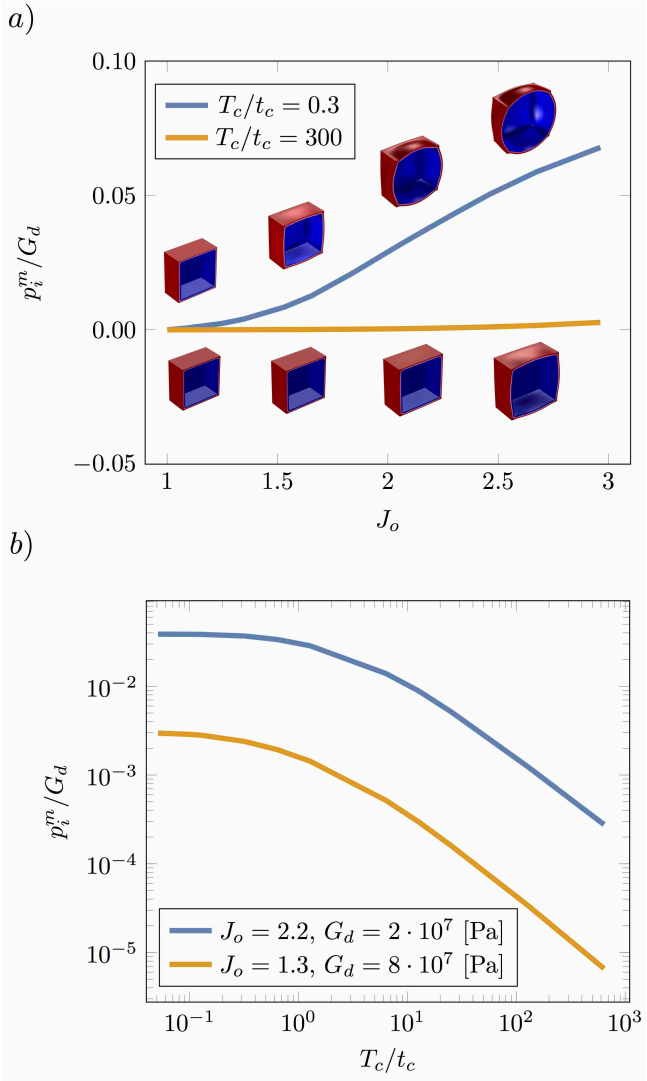

FIGURE 3.17: Inflatable–balloon mode. Top: Maximum dimensionless pressure p_i^m/G_d versus J_o at different ratios T_c/t_c (panel a). Bottom: Log-log plot of maximum dimensionless pressure p_i^m/G_d versus T_c/t_c at different J_o (panel b). We remember that $J_o = J_o(G_d)$; thus to each value of J_o there correspond a unique value of G_d; see Fig. 3.10, bottom.

(in a log-log plot). When $T_c/t_c > 10^2$, the maximum inner pressure is too low, and it is almost impossible to observe the inflatable-balloon mode. The dimensionless pressure p_i^m/G_d is higher for the softer gel (blue) than for stiffer ones (yellow); the same holds for the dimensional pressure p_i^m: at early times, $p_i^m \sim 6 \cdot 10^5$ Pa for the soft gel, and $p_i^m \sim 1.6 \cdot 10^5$ Pa for the stiff one.

3.3.8 Determinants for cavitation

We investigate how geometrical and material factors may trigger water cavitation, assuming $p_i = -10$ MPa as threshold for the phenomenon to happen. Through our numerical experiments, we discovered that shear modulus G_d, and slenderness parameter β are the main determinants in attaining cavitation.

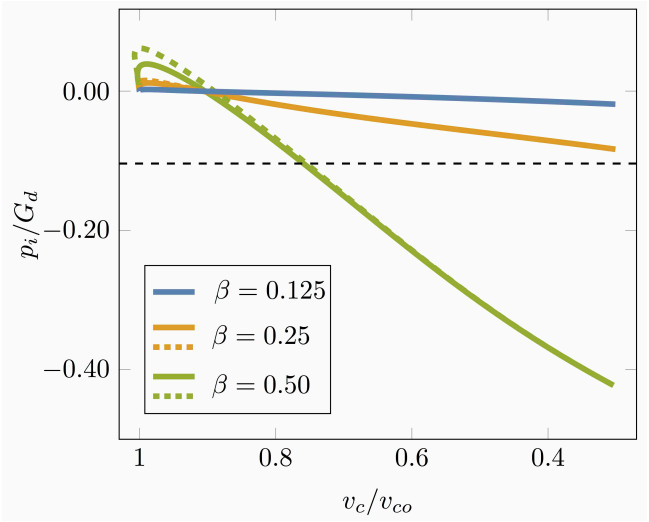

FIGURE 3.18: Dimensionless inner pressure p_i/G_d versus v_c/v_{co}, for different values of β and fixed $G_d = 10^8$ Pa. Solid lines are obtained with $h = 0.0025$ m and $l = (0.02\,\text{m}, 0.01\,\text{m}, 0.005\,\text{m})$, corresponding to $\beta = (0.125, 0.25, 0.50)$, respectively (blue, orange and green solid lines). Dashed lines are obtained with $l = 0.02$ m and $h = (0.005\,\text{m}, 0.01\,\text{m})$, corresponding to $\beta = (0.25, 0.50)$, respectively (orange and green dashed lines). The black dashed line represents the dimensionless pressure of water cavitation $p_c/G_d = -0.1$, with $G_d = 10^8$ Pa.

At first, we investigate the dependence on β with a constant $G_d = 10^8$ Pa. Fig. 3.18 shows dimensionless inner pressure p_i/G_d versus volume ratio v_c/v_{co}, for different values of β. We note that only the green curves, corresponding to $\beta = 0.5$ attain values below the dimensionless cavitation pressure (black, dashed). Cavitation should occur when the volume of the cavity has been reduced to about 70%. We also verified that more slender sample, with shear modulus $G_d = 10^7$ Pa cannot achieve cavitation pressure, as it is shown in Fig. 3.19 for $\beta = 0.125$ (the blue solid line always stays above the dashed blue line which marks the cavitation pressure threshold. Then, we investigate the dependence on G_d with a constant $\beta = 0.125$. Fig. 3.19 shows dimensionless inner pressure p_i/G_d versus volume ratio v_c/v_{co}, for different values of G_d, from $G_d = 10^7$ Pa to $G_d = 10^9$ Pa. The solid blue line represent the same case as the solid blue line of Fig. 3.18 (with a different scale of the vertical axis); this curve does not intersect the dashed blue line corresponding to the dimensionless cavitation pressure. On the contrary, both the green and orange solid lines, corresponding to higher G_d, intersect the cavitation pressure lines (orange and green dashed lines); for $G_d = 10^9$ Pa, cavitation pressure is achieved very soon, for v_c/v_{co} slightly less than 1. Finally, in Fig. 3.20, we present the result of our analyses with a contour plot of the inner pressure in the plane G_d, β; in Fig. 3.20 the iso-contour $p_i = -10$ MPa is highlighted by the arrow; such a contour plot may be interpreted as a phase diagram for cavitation to occur. We ran many numerical experiments to explore the space (β, G_d), and for each experiment we evaluated the inner pressure at $v_c/v_{co} = 0.3$, that is, at the maximum achievable value without self contact of hydrogels walls. Based on these pressure values, we interpolated iso–pressure lines; the contour at $p_i = -10$ MPa discriminate between a region where cavitation may occur and a region where it cannot.

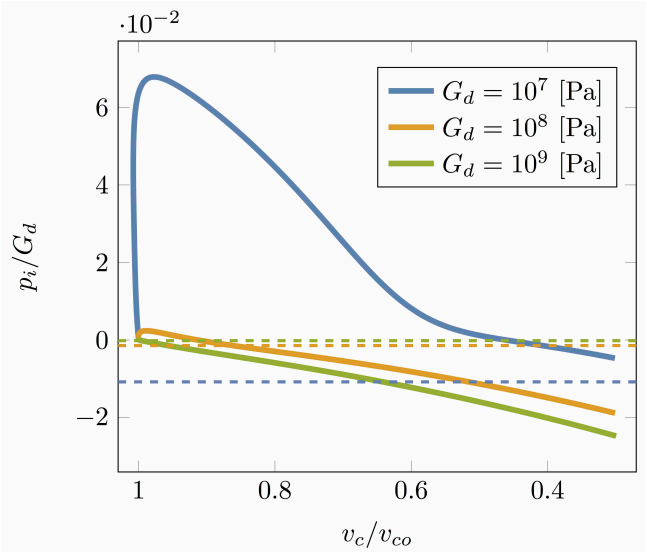

FIGURE 3.19: Dimensionless inner pressure p_i/G_d versus v_c/v_{co} for different values of G_d (solid lines). Dashed lines correspond to the dimensionless cavitation pressure for $G_d = 10^7$ Pa (blue), $G_d = 10^8$ Pa (green), $G_d = 10^9$ Pa (orange). We set: $h = 0.0025$ m, $l = 0.02$ m.

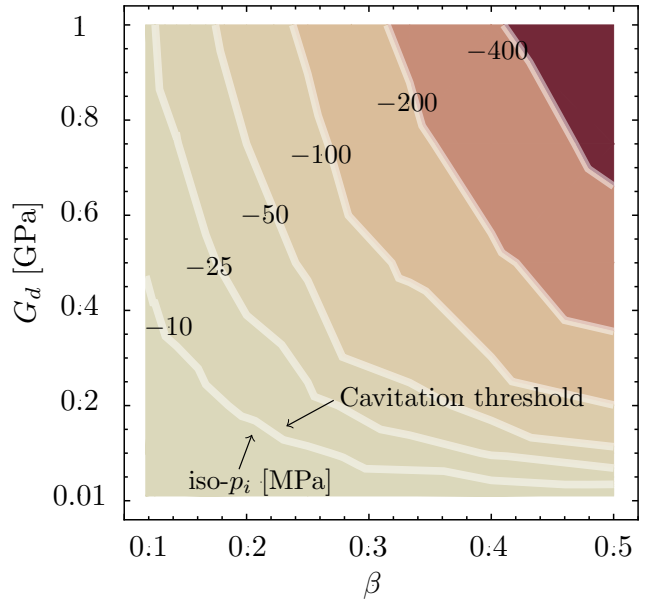

FIGURE 3.20: Phase diagram of cavity pressure. In the plane G_d, β, we highlight the isolines for the inner pressure p_i. The isoline $p_i = -10$ Mpa corresponds to the cavitation threshold: above this line, cavitation may occur. All the values of p_i have been evaluated at $v_c/v_{co} = 0.3$.

3.3.9 Dehydration under spherical symmetry

We discuss our ideal experiment, dehydration of a gel with a cavity filled with water, by considering a spherical sample. For a spherical geometry, this problem also allows for an analytical approximation based on the analysis developed in Ref.[100]. Therein, the phenomenon of hole formation in the interior of an elastic body in a state of tension has been studied and referred as cavitation, as it was common since

the '80 after the seminal paper by J.M. Ball cited as Ref.[101][6].

When dehydration preserves the condition of spherical symmetry, no inflatable–balloon mode is visible. Nevertheless, at early times, as already observed for the cubic sample, the inner pressure p_i increases, meanwhile the wall thickness decreases. Then, after achieving a maximum positive value, the pressure decreases to negative values, while the walls thicken.

It follows that, also for the spherical geometry, dehydration exhibits two phases, see Fig. 3.21. In particular, compare the top panels of Fig. s 3.12 and 3.21. These two phases, wall-thinning and wall-thickening, determine the so-called *breathing mode*, a non–monotonic deformation mode characteristic of cavities filled with water. In this case, the cavity reduces its size but retains the spherical shape [105]. We remark that the same phenomenon, a non–monotonic change of the wall thickness during dehydration, has been observed in our numerical experiments with cubic samples.

We propose an explicit solution of the dehydration problem by following the solution proposed in Ref.[100]. We consider a dry sphere having radius R_e, with a spherical cavity at its center of radius R_c. Under spherical symmetry conditions, the deformation of the sphere is described by the map $r(R)$ which delivers the actual radius r corresponding to the dry one R.

Our numerical experiments show that, both for the cubic and the spherical samples, the gel volume $v_g(t)$ remains constant during dehydration when $t \gg T_c$; we can write:

$$v_g(t)|_{t\gg T_c} \simeq \bar{J}_d\, v_{gd}\,, \quad \text{with } v_{gd} = \text{gel volume at dry state.} \tag{3.3.59}$$

Moreover, the value of $\bar{J}_d$ can be approximated by averaging the values of J_d imposed by the chemical boundary conditions: at $\partial\mathcal{B}_c$ we have $\mu = 0$ J/mol, and $J_d = J_o$; at $\partial_e\mathcal{B}_d$ we have $\mu = \mu_\infty$, and $J_d = 1$; it holds

$$\bar{J}_d = \frac{1 + J_o}{2}\,, \tag{3.3.60}$$

with the value of J_o controlled by the chemical potential through the equation (3.1.16). Equation (3.3.60) is the key to solve our problem; introducing the radial stretch λ_R and the hoop stretch λ_ϑ: we can write

$$\bar{J}_d = \lambda_R\, \lambda_\vartheta^2\,, \quad \text{with} \quad \lambda_R(R) = r'(R)\,, \quad \lambda_\vartheta(R) = \frac{r(R)}{R}\,. \tag{3.3.61}$$

Equations (3.3.61) yield an ODE that can be integrated explicitly:

$$r'(R)\,\left(\frac{r(R)}{R}\right)^2 = \bar{J}_d\,; \quad \text{boundary condition } r(R_c) = r_c\,. \tag{3.3.62}$$

The solution of (3.3.62) is the function

$$r(R) = (\, r_c^3 + \bar{J}_d\,(R^3 - R_c^3)\,)^{1/3}\,. \tag{3.3.63}$$

The hoop stretches at cavity and at the external boundary are

$$\lambda_c = \lambda_\vartheta(R_c) = \frac{r_c}{R_c}\,; \quad \lambda_e = \lambda_\vartheta(R_e) = \frac{r(R_e)}{R_e}\,. \tag{3.3.64}$$

[6]Successively, within the context of solid mechanics, cavitation has also been used as a synonymous for *discontinuous change of size* of an existing cavity in a solid, as in Refs. [102–104] which focus on a hydrogel sphere with a cavity.

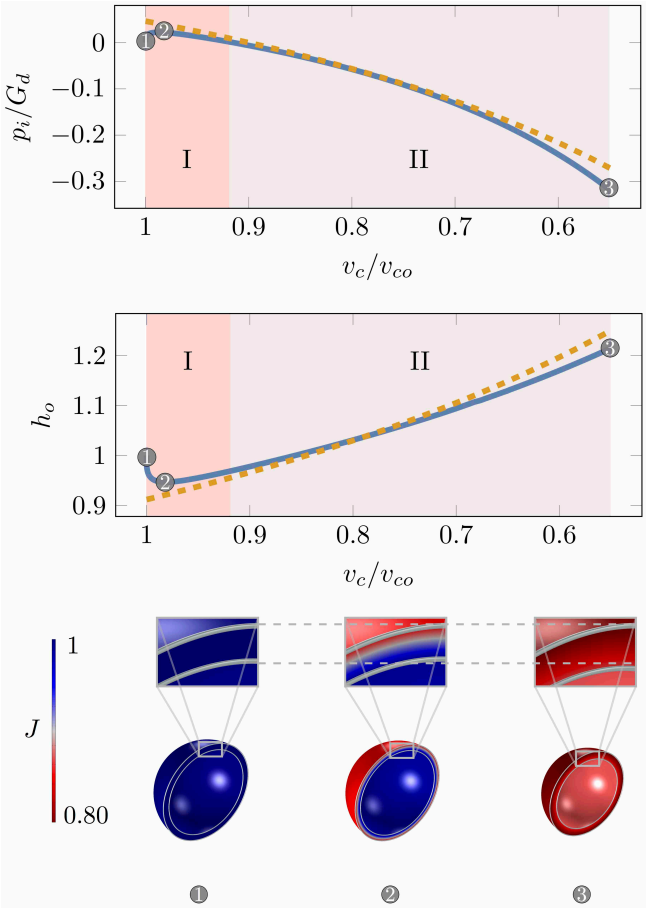

FIGURE 3.21: The breathing mode of a spherical cavity is represented in terms of the dimensionless pressure p_i/G_d (top), and of the dimensionless walls thickness h_o (central panel) versus v_c/v_{co}. Results from an approximate explicit analysis (dashed orange lines) and from numerical solutions (solid blue lines) are compared. The change in volume of the sphere walls is represented through a colour code related to J_d (bottom panel). The geometry of the dry sphere is fixed by the external R_e and internal radius R_c: $R_e = 0.01$m, and $R_c = 0.00875$m.

Then, given the elastic energy density per unit reference volume $\hat{W} = \hat{W}(\lambda_R, \lambda_\vartheta)$, the total potential energy of the sphere can be written as:

$$\mathcal{E} = \int_{R_c}^{R_e} 4\,\pi\, R^2 \hat{W}(\lambda_R, \lambda_\vartheta)\, dR - p_i\, 4\pi R_c^3 (\lambda_c - 1)\,, \tag{3.3.65}$$

Following Ref.[100], we assume a change of variable, $r/R = h$, and consider the elastic energy as a function of t:

$$\hat{W}(\lambda_R, \lambda_\vartheta) = \hat{W}\left(\frac{\bar{J}_d}{\lambda_\vartheta^2}, \lambda_\vartheta\right) = W(h)\,. \tag{3.3.66}$$

Moreover, from the change of variable, and from (3.3.62), we have

$$dt = \frac{\bar{J}_d - h^3}{t^2}\,\frac{dR}{R}\,, \quad R^3 = \frac{r_c^3 - \bar{J}_d\, R_c^3}{h^3 - \bar{J}_d}\,, \tag{3.3.67}$$

and we can use these relations to rewrite the first summand of (3.3.65) as an integral over h

$$\int_{R_c}^{R_e} 4\,\pi\,R^2\hat{W}(\lambda_R,\lambda_\vartheta)\,dR = 4\,\pi\,(r_c^3-\bar{J}_d\,R_c^3)\int_{\lambda_e}^{\lambda_c}\frac{h^2}{(h^3-J_d)^2}\,W(h)\,dh\,. \tag{3.3.68}$$

Then, integrating by parts, we obtain:

$$\begin{aligned}\mathcal{E} &= \frac{4\,\pi}{3}\,(r_c^3-\bar{J}_d\,R_c^3)\int_{\lambda_e}^{\lambda_c}\frac{W'}{(h^3-\bar{J}_d)}\,dh \\ &+ \frac{4\,\pi}{3}\,\left(R_e^3\,W(\lambda_e)-R_c^3\,W(\lambda_c)\right)-p_i\,4\,\pi\,R_c^3\,(\lambda_c-1)\,.\end{aligned} \tag{3.3.69}$$

Finally, from the stationary condition we obtain a formula for p_i

$$\frac{d\mathcal{E}}{dr_c}=0 \quad\Rightarrow\quad p_i=\lambda_c^2\int_{\lambda_e}^{\lambda_c}\frac{W'}{(h^3-\bar{J}_d)}\,dh\,. \tag{3.3.70}$$

For a Neo–Hookean elastic energy, we have

$$W(t)=\frac{G_d}{2}(\bar{J}_d{}^2h^{-4}+2\,h^2-3)\,. \tag{3.3.71}$$

Inserting (3.3.71) in (3.3.70) yields the inner pressure as a function of G_d, $\bar{J}_d$ (that is, the chemical boundary conditions), and the two hoop stretches λ_c , λ_e:

$$\frac{p_i}{G_d}=\frac{\lambda_c}{2}\left(\frac{\bar{J}_d+4\,\lambda_e^3}{\lambda_e^4}-\frac{\bar{J}_d+4\,\lambda_c^3}{\lambda_c^4}\right)\,. \tag{3.3.72}$$

Actually, $\bar{J}_d$, λ_e, and λ_c are not independent; as example, by using (3.3.63), we can write λ_e as a function of $\bar{J}_d$ and λ_c

$$\lambda_e=\bar{J}_d+\left(\frac{R_c}{R_e}\right)^3\,(\lambda_c^3-\bar{J}_d)\,. \tag{3.3.73}$$

It is worth introducing the cavity hoop-stretch $\tilde{\lambda}_c$, as measured with respect to the hoop stretch at the free-swollen state λ_{co}; it is given by

$$\tilde{\lambda}_c=\frac{r_c}{R_{co}}=\frac{\lambda_c}{\lambda_{co}}=\left(\frac{v_c}{v_{co}}\right)^{1/3}\,. \tag{3.3.74}$$

Thus, using (3.3.73) and (3.3.74), it is possible to rewrite (3.3.72) as a function of the free-swollen stretch of the cavity λ_{co}, and the volume ratio v_c/v_{co}:

$$\begin{aligned}\frac{p_i}{G_d} &= -\frac{1}{2}\left(\frac{v_c}{v_{co}}\right)^{1/3}\frac{\bar{J}_d+4\,\lambda_{co}^3\,(v_c/v_{co})}{\lambda_{co}^3(v_c/v_{co})}\,\lambda_{co} \\ &+ \frac{1}{2}\frac{5\,\bar{J}_d-4\,(\bar{J}_d-\lambda_{co}^3\,(v_c/v_{co}))\,(R_c/R_e)^3}{(\bar{J}_d-(\bar{J}_d-\lambda_{co}^3\,(v_c/v_{co}))\,(R_c/R_e)^3)^{4/3}}\,\lambda_{co}^2\,(v_c/v_{co})^{2/3}\,.\end{aligned} \tag{3.3.75}$$

Fig. 3.21, top panel, shows the dimensionless pressure p_i/G_d as evaluated by the explicit formula (3.3.75) (orange, dashed), and by numerical simulations (blue, solid),

for $\lambda_{co} = 1.077$ and $\bar{J}_d = 1.124$. The dimensionless thickness

$$h_o = \frac{r(R_e) - r_c}{(R_e - R_c)\lambda_{co}}, \tag{3.3.76}$$

is an important determinant of the breathing mode: Fig. 3.21 (middle) shows the non–monotonic behavior of h_o versus (v_c/v_{co}).

3.4 Growth and swelling of hydrogels

A further complication in hydrogels and generally in wood-like material is the presence of residual strains after hydration-dehydration cycles which are usually not taken in account in the modelling and which can significantly change the behavior of such material. For this reason, in this section, we aim at coupling the theory of swelling, describing the effects of solvent uptake in polymeric solids, with that of growing, describing the change of the relaxed state in a continuum body [106]. Basing on the hypotheses underlying the two theories, and using some key principles of continuum mechanics, we develop a chemo-mechanical model which describes the combined effects of swelling and growing in solids.

As swelling is often taken as synonymous with growth, we begin by framing our meaning of swelling and growth: for us, the two words relate to quite different physical phenomena. The swelling theory is the one put forth by Flory and Rehner [72] to describe the change in volume due to solvent uptake which is observed in many cross-linked polymer networks when they are immersed in a solvent bath; thus, swelling (or de-swelling) is always accompanied by an exchange of mass, the mass of solvent entering (or exiting from) the polymer. This theory has a long tradition, started with the seminal papers [107, 108], and later developed in [109]; it describes effectively volume transitions, see [110] for an informative review, and is based on the coupling of the mixing energy typical of polymer solutions, with the elastic energy for cross-linked polymers: the coupling is constitutive and relates the volume change of the polymer with the volume of solvent uptake or release. The state of the system can be controlled by the chemical potential of the solvent bath and the applied loads; it is important to note that any change of volume is accompanied by a change in both the mixing and the elastic part of the free energy [66, 68].

The theory can describe both steady states and time-evolutive processes; important examples of the former class are the homogeneous, stress-free, swollen states; for the latter, we cite the phenomena of differential swelling that appears during the solvent exchange, or the morphing exhibited by non-homogeneous gels, as studied in [111–114]; also non-isotropic swelling can be described within the same framework [115, 116]. We note that swelling theory cannot describe the emergence of residual stress (meant as permanent stress), as any possible stress state generated by swelling, vanishes upon de-swelling.

For growth we mean a quite different phenomenon, conceived beforehand any assumption on the exchange of mass: local changes of the ground state. The simplest example of such a growth is the thermal expansion in solids: a metal increases its volume upon heating, while no mass is exchanged; moreover, for a body which is homogeneous, unconstrained, and uniformly heated, no elastic energy is stored during the volume change. In this sense, heating does not change the ground state of the solid.

The aforementioned phenomena are best described as local changes of the zero-stress reference state, as presented in [117]; the theory of bulk growth is based on the multiplicative decomposition of the deformation gradient, [118, 119], and has been more recently augmented by a balance law for the remodelling actions, [120], a contribution we consider noteworthy. The theory of growth has also been used to describe remodelling of living tissues as in [121–123].

Growth endows the body manifold with a target metric, whose consequences on both compatibility, embedding, and morphing have been investigated [83, 124–126].

Contrary to the swelling theory, growth can describe quite well the emergence of residual stress; nevertheless, growth theory is still in its infancy, especially with regards to the role played by the remodelling actions, the Eshelby-like tensor and the time evolutive processes; an attempt in this direction may be found in [127].

Here, we aim at coupling the theory of swelling with that of growth on the basis of some key principles of continuum mechanics. The model herein presented can describe large deformations of solids where the volume variation is different from the volume of solvent which is exchanged, a phenomenon very common in complex polymers. An important class of materials exhibiting this phenomenon is wood; as example, uptake of solution with water and a low molecular weight polymer as polyethylene glycol induces bulking, a permanent swelling where wood retains part of its swollen state upon drying [10]. Bulking is caused by the deposition of extractives within wood cell walls when water evaporates, thus changing the relaxed state of cells.

We conclude our introduction by mentioning the theory of biphasic mixtures, which describes the interactions between a porous-permeable solid, and an interstitial fluid [128]. The model herein presented, describing a growing solid which is swollen by a fluid, may appear similar to the theory of biphasic mixtures; indeed, the model is quite different: a main difference is that the mixture theory describes the motion of all constituents, while our model describes only the motion of the solid, apart from the concentration of the fluid; another key difference is the augmented kinematics used to describe growth, which is not present in the mixture theory.

3.4.1 State variables for growth and swelling

Let $\mathcal{E}$ be the 3D Euclidean space, $V\mathcal{E}$ the associated translation space, $\mathbb{L}\mathtt{in}$ the space of double tensors on $V\mathcal{E}$, and $\mathcal{T}$ the time line. We assume the dry configuration of the body $\mathcal{B}_d$, an open set of $\mathcal{E}$, as reference configuration, and we denote with $X_d \in \mathcal{B}_d$ a material point of $\mathcal{B}_d$; in our model, the chemo-mechanical state of the body is described by a position-valued field f_d, a tensor-valued field $\mathbf{F}_g$, and a scalar field c_d

$$\begin{aligned} f_d &: \mathcal{B}_d \times \mathcal{T} \to \mathcal{E}\,, && \text{motion;} \\ \mathbf{F}_g &: \mathcal{B}_d \times \mathcal{T} \to \mathbf{Lin}\,, && \text{relaxed stance;} \\ c_d &: \mathcal{B}_d \times \mathcal{T} \to \mathcal{R}\,, && \text{solvent concentration.} \end{aligned} \tag{3.4.77}$$

The motion f_d is standard in mechanics: it gives the actual position $x = f_d(X_d, \tau)$ of a material point X_d at time τ; given a motion, we can define the displacement vector as $\mathbf{u}_d(X_d, \tau) = f_d(X_d, \tau) - X_d$.

Given any complete motion $(f_d, \mathbf{F}_g)$, we define the velocity pair $(\mathbf{v}, \mathbb{V})$, with $\mathbf{v} = \dot{\mathbf{u}}_d$, $\mathbb{V} = \dot{\mathbf{F}}_g\,\mathbf{F}_g^{-1}$, and the associated test velocities $(\tilde{\mathbf{v}}, \tilde{\mathbb{V}})$.

We denote with $\mathbf{F}_d = \nabla f_d$ the gradient of the motion; the set $\mathcal{B}_\tau = f_d(\mathcal{B}_d, \tau)$ describes the actual configuration of $\mathcal{B}_d$ at time τ. A field defined on $\mathcal{B}_d \times \mathcal{T}$ is called a *material field*; conversely, a field defined on $\mathcal{B}_\tau$ is called a *spatial field*.

The relaxed stance $\mathbf{F}_g$, or distortion, is meant to describe the volumetric growth, and deserves careful comments: following the idea from [117], growth is defined as a change in the zero-stress reference state. Thus, $\mathbf{F}_g$ defines, at each material point X_d, a stress-free distorted volume-element: to envision the notion of distortions, you may want to consider some volume elements attached to neighboring body points; after the action of a smooth field $\mathbf{F}_g$, the distorted volume elements are in a *relaxed state*, but in general, they are not compatible. To glue together the new volume elements, that is, to realize any actual configuration $\mathcal{B}_\tau$, a further deformation $\mathbf{F}_e$ is necessary, defined by:

$$\mathbf{F}_e = \mathbf{F}_d \, \mathbf{F}_g^{-1}, \quad \text{elastic deformation.} \tag{3.4.78}$$

Equation (3.4.78) represents the *Kröner-Lee* decomposition of the deformation gradient $\mathbf{F}_d$ originally introduced in [118, 119] to describe viscoplastic strains.

It follows the paramount difference between $\mathbf{F}_d$ and $\mathbf{F}_g$: the first tensor field is the gradient of a motion, that is, it implies the existence of a displacement field that realizes the configuration $\mathcal{B}_\tau$; the second one is not the gradient of any field, and in general a relaxed configuration cannot be conceived, not even locally; a review on compatibility issues can be found in [126].

Moreover, it is worth saying that distortions have a two-fold nature: a kinematical one, as they add 9 further degrees of freedom, independent from the motion f_d; a dynamical one, as they describe a zero-stress state of the body elements. We quote verbatim from [120] "$\mathbf{F}_g$ cannot even be conceived without the standard notion of stress and some constitutive information on it." Thus, the use of the term ground state, that here anticipates the specification of a free energy, calls attention to the fact the distortions do not change the value of the free-energy density of body elements.

The key volume measures are the reference volume element $dV_d(X_d)$, the relaxed element $dV_g(X_d, \tau)$ and the actual element $dv(x, \tau)$; given the Jacobians

$$J_d = \det\mathbf{F}_d \,, \; J_g = \det\mathbf{F}_g \,, \; J_e = \det\mathbf{F}_e = J_d \, J_g^{-1} \,, \tag{3.4.79}$$

the three volume elements are related by:

$$dV_g = J_g \, dV_d \,, \quad dv = J_d \, dV_d = J_e \, dV_g \,; \tag{3.4.80}$$

we note that the second formula involves a change of variable

$$dv(\underbrace{f_d(X_d, \tau)}_{x}, \tau) = J_d(X_d, \tau) \, dV_d(X_d) \,. \tag{3.4.81}$$

Finally, we describe c_d: it represents the chemical state variable, and measures the solvent content per unit of dry volume: $[c_d] = \text{mol/m}^3$. We can alternatively consider different solvent concentrations: introduced the elementary amount of solvent dc, we may write

$$dc = c_d \, dV_d = c_g \, dV_g = c \, dv \,. \tag{3.4.82}$$

with

$$\begin{aligned} &c(x, \tau) && \text{concentration per unit of actual volume;} \\ &c_g(X_d, \tau) && \text{concentration per unit of relaxed volume;} \end{aligned} \tag{3.4.83}$$

All these concentrations are related by standard pull back formulas for scalar densities: from (3.4.80) it follows

$$\begin{aligned} c_d(X_d,\tau) &= c_g(X_d,\tau)\, J_g(X_d,\tau)\,, \\ c_d(X_d,\tau) &= c(\underbrace{f_d(X_d,\tau)}_{x},\tau)\, J_d(X_d,\tau)\,; \end{aligned} \tag{3.4.84}$$

as in (3.4.81), the second formula contains a change of variables, which is usually written in short as $c_d = c_m\, J_d$, with $c_m = c \circ f_d$, the material description of the spatial field c.

Introduced the molar volume of the solvent Ω, that is, the parameter describing the volume occupied by one mole of solvent, $[\Omega] = \mathrm{m}^3/\mathrm{mol}$, it follows that we can gauge the elementary solvent volume by using the different densities c_d, c_g, or c, as follows

$$dV_{sol} = \Omega\, c_d\, dV_d = \Omega\, c_g\, dV_g\,, \quad dv_{sol} = \Omega\, c\, dv\,. \tag{3.4.85}$$

Thus, the total volume of solvent contained in our body can be evaluated by an integral on $\mathcal{B}_d$ or $\mathcal{B}_\tau$:

$$\int_{\mathcal{B}_d} \Omega\, c_d\, dV_d = \int_{\mathcal{B}_d} \Omega\, c_g\, dV_g = \int_{\mathcal{B}_\tau} \Omega\, c\, dv\,. \tag{3.4.86}$$

The cartoon in Fig. 3.22 shows the action of the three tensor maps $\mathbf{F}_d$, $\mathbf{F}_g$, and $\mathbf{F}_e$ on the volume elements. Our key constitutive assumption, to be discussed later, is that the volume change J_e is only due to solvent uptake or release, that is, the actual volume element dv is the sum of the relaxed one dV_g, plus the solvent contribution dV_{sol}; this hypothesis implies an important chemo-mechanical coupling.

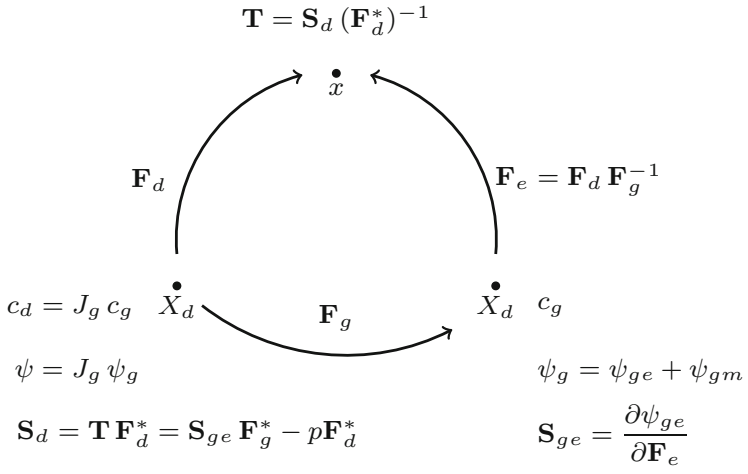

FIGURE 3.22: The free energies are given as densities per unit relaxed volume. The reference stress $\mathbf{S}_d$ and the stress $\mathbf{T}$ are densities per unit of reference and actual volume, respectively; they are related by the adjugate $\mathbf{F}_d^*$. The energetic part of the stress $\mathbf{S}_{ge}$, defined as the derivative of the energy ψ_{ge} with respect to $\mathbf{F}_e$, is a density per unit relaxed volume.

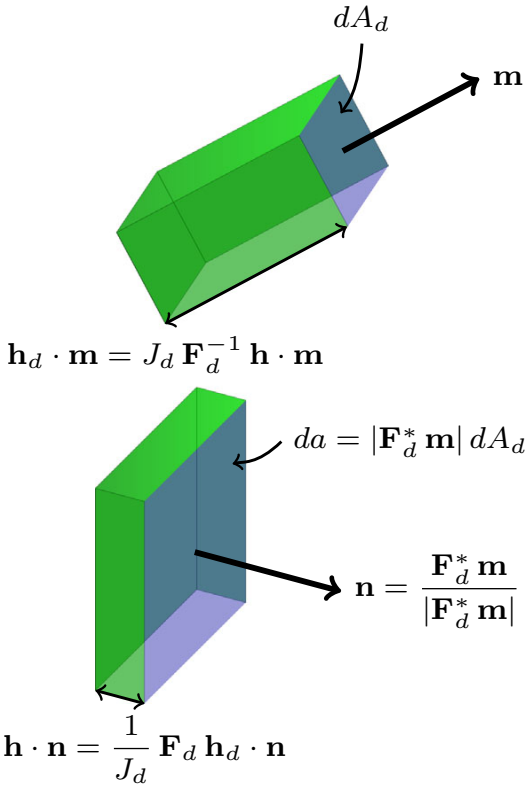

FIGURE 3.23: Geometrical interpretation of dry-reference and actual fluxes. The top and bottom parallelepipeds share the same elementary volume: $\mathbf{h}_d \cdot \mathbf{m}\, dA_d = \mathbf{h} \cdot \mathbf{n}\, da$; such volume measures the moles per second crossing the surfaces dA_d (top) or da (bottom).

3.4.2 Balance laws

Our model has three state variables: two of them concern mechanics, the motion f_d, and the growth $\mathbf{F}_g$, while the third one, the solvent concentration c_d, is a chemical variable. Thus, the model has three balance laws: the balances of working for both motion and growth, and the balance of solvent mass. It is of the essence to remark that the assumption of $\mathbf{F}_g$ as state variable demands for a proper balance law, an important point that is often missed, and that is clearly stated in [120].

Balance of solvent mass

Introduced the molar mass of the solvent $\mathbf{M}$, that is, the mass of one mole of solvent, $[\mathbb{M}]$ =Kg/mol, we may gauge the mass of the solvent contained in $\mathbf{M}_d$ by the integrals:

$$\text{Solvent Mass} = \int_{B_d} \mathbf{M}\, c_d\, dV_d = \int_{B_\tau} \mathbf{M}\, c\, dv\,. \tag{3.4.87}$$

Being $\mathcal{M}$ constant, the time-rate of the solvent mass involves only the concentration c_d; thus, the balance of solvent can be stated as follows: for any part $\mathcal{P}_\tau \subset \mathcal{B}_\tau$ of the body, the time-rate of solvent moles equals the solvent source $q = q(x, \tau)$ at the boundary $\partial\mathcal{P}_\tau$, with q a molar source per unit surface, $[q] = \text{mol}/(\text{m}^2\ \text{s})$:

$$\frac{\partial}{\partial \tau} \int_{\mathcal{P}_\tau} c\, dv = \int_{\partial \mathcal{P}_\tau} q\, da\,, \quad \forall\, \mathcal{P}_\tau \subset \mathcal{B}_\tau\,, \tag{3.4.88}$$

with da the surface element on $\partial\mathcal{B}_\tau$. The boundary source q can be represented in terms of a *molar flux* $\mathbf{h} = \mathbf{h}(x,\tau)$, ($[\mathbf{h}] = \text{mol}/(\text{m}^2\,\text{s})$), a vector-valued quantity such that $q = -\mathbf{h}\cdot\mathbf{n}$, with $\mathbf{n}$ the normal at $\partial\mathcal{P}_\tau$; being $\mathbf{n}$ the outward normal, $-\mathbf{h}\cdot\mathbf{n} > 0$ implies an inward flux. Both left and right terms of (3.4.88) can be pulled back on the dry-reference part $\mathcal{P}_d$:

$$\begin{aligned}\frac{\partial}{\partial t}\int_{\mathcal{P}_\tau} c\,dv &= \int_{\mathcal{P}_\tau}(\dot{c} + c\,\text{div}v)\,dv = \int_{\mathcal{P}_d}\dot{c}_d\,dV_d\,, \\ \int_{\partial\mathcal{P}_\tau}\mathbf{h}\cdot\mathbf{n}\,da &= \int_{\partial\mathcal{P}_d}\mathbf{h}_d\cdot\mathbf{m}\,dA_d = \int_{\mathcal{P}_d}\text{div}\mathbf{h}_d\,dV_d\,,\end{aligned} \tag{3.4.89}$$

with dA_d the surface element on $\partial\mathcal{B}_d$, $\mathbf{m}$ its outward normal, and $\mathbf{h}_d = \mathbf{h}_d(X_d,\tau)$ the molar flux gauged on the dry-reference state (the pull back of $\mathbf{h}$), defined by

$$\mathbf{h}_d = J_d\,\mathbf{F}_d^{-1}\,\mathbf{h}_m\,, \quad \text{with } \mathbf{h}_m = \mathbf{h}\circ f\,. \tag{3.4.90}$$

It follows that $\mathbf{h}\cdot\mathbf{n}\,da$ and $\mathbf{h}_d\cdot\mathbf{m}\,dA_d$ represent the same elementary flux rate, measured in mol/s, see Fig. (3.23). To the flux $\mathbf{h}_d$ it is associated a boundary source q_d per unit dry-reference area, given by $q_d = -\mathbf{h}_d\cdot\mathbf{m}$.

It follows from (3.4.88, 3.4.90) the balance law of solvent mass in strong, or differential form, written on the dry-reference configuration, which has to be supplemented by initial and boundary conditions:

$$\begin{aligned}&\dot{c}_d = -\text{div}\mathbf{h}_d, \text{on } \mathcal{B}_d\times\mathcal{T}\,, && \text{balance of solvent mass;}\\ &-\mathbf{h}_d\cdot\mathbf{m} = q_d, \text{on } \partial_h\mathcal{B}_d\times\mathcal{T}\,, && \text{flux at boundary } \partial_h\mathcal{B}_d;\\ &c_d = \bar{c}_d, \text{on } \partial_c\mathcal{B}_d\times\mathcal{T}\,, && \text{solvent at boundary } \partial_c\mathcal{B}_d;\\ &c_d = c_{do}, \text{on } \mathcal{B}_d\times\{0\}\,, && \text{initial conditions;}\end{aligned} \tag{3.4.91}$$

here $\partial_h\mathcal{B}_d$ and $\partial_c\mathcal{B}_d$ represent the portions of the boundary where it is controlled the flux, or the solvent concentration, respectively.

Some remarks

- It is worth introducing here the chemical potential μ, a scalar-valued quantity measuring the molar energy, that is, the energy-density per mole: $[\mu]$=J/mol; its proper definition will be given in the next section devoted to the Constitutive Prescriptions. The product $\mu\,q$ is a power-density per unit area:

$$[\mu\,q] = \frac{\text{J}}{\text{mol}}\,\frac{\text{mol}}{\text{s}\,\text{m}^2} = \frac{\text{W}}{\text{m}^2}\,. \tag{3.4.92}$$

  It represents the chemical power-density associated to the boundary source q, and can be equivalently gauged by the product $\mu\,q_d$, a power-density per unit dry-reference area:

$$\mu\,q\,da = \mu\,q_d\,dA_d\,. \tag{3.4.93}$$

- It is quite difficult, if not impossible, to control the solvent concentration $\bar{c}_d$ at the boundary; usually, we can control the external chemical potential μ^e, and the pressure p^e of the environment. It follows that the boundary condition

$(3.4.91)_3$ is superseded by an implicit equation relating c_d to μ^e. This equation will be soon derived from an appropriate representation formula for the free energy, see $(3.4.116)_2$.

Balance of working

In mechanics, *power* is the fundamental integral quantity, and balance equations are naturally expressed in integral form in terms of *virtual power*, or *working*. The working is a continuous, linear, real-valued functional on the space of test velocities $(\tilde{\mathbf{v}}, \tilde{\mathbb{V}})$; it is usually splitted additively into an *inner* working $\mathcal{P}_i$, an *outer* working $\mathcal{P}_e$, and the working done by inertia forces $\mathcal{P}^{ine}$. Following [120], we assume

$$\begin{aligned} \mathcal{P}_i(\tilde{\mathbf{v}}, \tilde{\mathbb{V}}) &:= \int_{\mathcal{B}_d} (-\mathbf{S} \cdot \nabla \tilde{\mathbf{v}} + \mathbb{C} \cdot \tilde{\mathbb{V}}) \, dV_d \,, \\ \mathcal{P}_e(\tilde{\mathbf{v}}, \tilde{\mathbb{V}}) &:= \int_{\mathcal{B}_d} (\mathbf{b} \cdot \tilde{\mathbf{v}} + \mathcal{B} \cdot \tilde{\mathbb{V}}) \, dV_d + \int_{\partial \mathcal{B}_\tau} \mathbf{t} \cdot \tilde{\mathbf{v}} \, da \,. \end{aligned} \tag{3.4.94}$$

The inner working involves the reference stress tensor $\mathbf{S}$ (aka, first Piola-Kirchhoff stress), and the tensor $\mathbb{C}$ representing the inner remodelling action; the outer working involves the bulk force vector $\mathbf{b}$, the boundary load $\mathbf{t}$, and the outer remodelling action $\mathbb{B}$. It holds $[\mathbf{S}] = [\mathbb{C}] = [\mathbb{B}] = [\mathbf{t}] = \mathrm{J/m^3}$=Pa, $[\mathbf{b}] = \mathrm{N/m^3}$. Neglecting the inertial working, the *balance principle* states that, at each time, and for any test velocity, the total working must be null, that is:

$$0 = \mathcal{P}_i(\tilde{\mathbf{v}}, \tilde{\mathbb{V}}) + \mathcal{P}_e(\tilde{\mathbf{v}}, \tilde{\mathbb{V}}) \,, \quad \forall \, \tilde{\mathbf{v}} \,, \tilde{\mathbb{V}} \,. \tag{3.4.95}$$

It is worth noting that the two principles previously mentioned, the Balance of Mass and the Balance of Working are very different from each other; in particular, the second one involves the power, a notion which is not present in the first one. Mechanical and chemical power will be confronted within the Dissipation Principle, to be presented in the next section.

Standard localization arguments applied on (3.4.95), yield the following balance of forces

$$0 = \mathrm{div}\mathbf{S} + \mathbf{b} \,, \quad \text{on } \mathcal{B}_d \,; \quad \mathbf{S}\,\mathbf{m} = \mathbf{t} \,, \quad \text{on } \partial \mathcal{B}_d \,, \tag{3.4.96}$$

and balance of remodelling actions

$$0 = \mathbb{C} + \mathbb{B} \,, \quad \text{on } \mathcal{B}_d \,, \tag{3.4.97}$$

which have to be supplemented by initial conditions on $\mathbf{u}_d$, $\mathbf{F}_g$, and kinematics boundary conditions on $\mathbf{u}_d$.

The stress $\mathbf{T}$ (aka, Cauchy stress) is related to the reference stress $\mathbf{S}$ by the standard relation $\mathbf{S} = \mathbf{T}_m \, \mathbf{F}_d^*$, with $\mathbf{T}_m = \mathbf{T} \circ f_d$, where with the notation $\mathbf{A}^*$ we mean the adjugate of $\mathbf{A} \in \mathbb{L}\mathtt{in}$: $\mathbf{A}^* = (\det \mathbf{A}) \, \mathbf{A}^{-T}$.

Some remarks

- The inner working does not contain actions dual to $\tilde{\mathbf{v}}$: these kind of inner actions are ruled out by the principle of frame indifference; this is not true for the inner remodelling actions.

- To keep our growth theory as simple as possible, yet not trivial, the inner working does not contain actions dual to $\nabla\tilde{\mathbb{V}}$; for this reason, there are neither boundary remodelling actions, nor boundary conditions on such kind of actions.

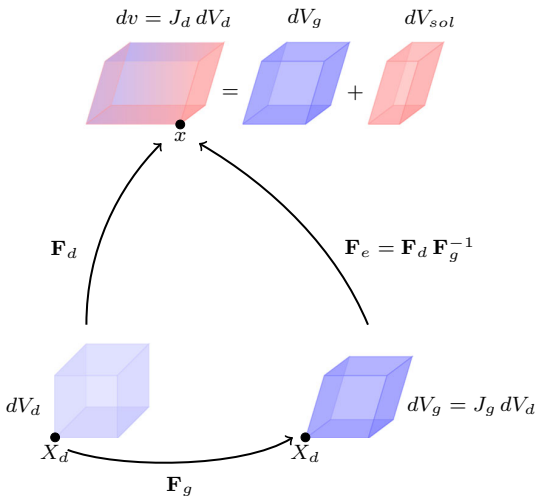

FIGURE 3.24: Consider a dry volume-element dV_d at X_d; the growth $\mathbf{F}_g$ defines the relaxed volume-element dV_g at X_d, while the solvent uptake swells dV_g to the actual volume $dv = J_e\, dV_g = J_d\, dV_d$, sitting at x. The change in volume from dV_g to dv is entirely due to the added volume of solvent: $dv = dV_g + dV_{sol}$.

3.4.3 Constitutive prescriptions

We shall pose the following constitutive assumptions and derive their consequences:

- Volume change from relaxed volume dV_g to the actual one dv is only due to solvent uptake or release;
- The free energy is the sum of an elastic term plus a chemical one;
- The elastic energy has to be a function of the elastic strain $\mathbf{F}_e$;
- The chemical energy is a function of the ratio dV_g/dv;
- Dissipation is only related to the solvent flux and to the remodelling actions.

We note that the three balance laws (3.4.91, 3.4.96, 3.4.97) are not coupled; two important couplings shall arise as consequence of the constitutive recipes: the chemo-mechanical coupling between c_d and J_d, and the Eshelbian coupling between $\mathbb{C}$ and $\mathbf{S}$.

Volumetric constraint

A key assumption in the classical theory of swelling says that the volume change from the dry state to the wet one is entirely due to solvent uptake [109]; using our notation: $dv = J_d\, dV_d = dV_d + dV_{sol}$.

The previous assumption must be rephrased to account for growth, as now the solvent volume-element dV_{sol} must be considered as a volume that is added to the relaxed volume-element dV_g. Thus, the volumetric constraint has the following form:

the actual volume-element dv is the sum of the relaxed volume-element dV_g, plus the solvent volume-element dV_{sol}:

$$dv = J_e\, dV_g = dV_g + dV_{sol} = (1 + \Omega\, c_g)\, dV_g\,. \tag{3.4.98}$$

It is worth noting that this assumption does not supersede the multiplicative composition $J_e = J_d / J_g$, but has to be paired with it: this implies

$$\begin{aligned} J_e &= 1 + \Omega\, c_g = 1 + \Omega\, \frac{c_d}{J_g} = \hat{J}_e(c_d, J_g)\,, \\ J_d &= J_e\, J_g = J_g + \Omega\, c_d = \hat{J}_d(c_d, J_g)\,. \end{aligned} \tag{3.4.99}$$

Thus, the volumetric constraint relates the Jacobian J_d, a mechanical quantity, to the solvent concentration c_d and to the growth Jacobian J_g; more important, it implies a coupling between our balance laws. It is worth noting that, being the relaxed volume a dry volume, $J_e \geq 1$, and thus $J_d \geq J_g$; the case $J_e = 1$ corresponds to the growth of an (elastically) incompressible material, with no solvent uptake. Moreover, from (3.4.99), it follows that we can measure the solvent volume-element with the difference between J_d and J_g:

$$dV_{sol} = \Omega\, c_d\, dV_d = (J_d - J_g)\, dV_d\,. \tag{3.4.100}$$

We now define the *solid volume fraction* ϕ, a scalar-valued function measuring pointwise the ratio between the elementary relaxed-volume dV_g occupied by the body, and the actual elementary volume dv:

$$\phi = \frac{dV_g}{dv} = \frac{1}{J_e} = \frac{J_g}{J_d} \quad \Rightarrow \quad \phi = \frac{J_g}{J_g + \Omega\, c_d}\,, \tag{3.4.101}$$

that is, $\phi = \phi(J_e) = \phi(c_d, J_g)$ may be considered as a function of J_e, or of the state variables c_d, $\mathbf{F}_g$. Let us note that ϕ ranges in $(0, 1)$, according to:

$$\begin{aligned} &\text{no solvent} && \Leftrightarrow \quad J_e = 1 && \Leftrightarrow \quad \phi = 1\,; \\ &\frac{\text{solvent}}{\text{solid}} \to \infty && \Leftrightarrow \quad J_e \to \infty && \Leftrightarrow \quad \phi \to 0\,. \end{aligned} \tag{3.4.102}$$

Free energy

We assume the free-energy density per unit of relaxed-volume ψ_g, $[\psi_g]$ =J/m^3, to be the sum of the elastic energy ψ_{ge}, and of the solid–solvent mixing energy ψ_{gm}; moreover, we assume the elastic energy to be a function of the right Cauchy-Green strain $\mathbf{C}_e = \mathbf{F}_e^T\, \mathbf{F}_e$, and the mixing energy to depend on the volume fraction ϕ, that can be represented in terms of the state variables through (3.4.101); we have:

$$\psi_g(\mathbf{C}_e, c_d, J_g) = \psi_{ge}(\mathbf{C}_e) + \psi_{gm}(c_d, J_g)\,,\ J_e = \hat{J}_e(c_d, J_g)\,. \tag{3.4.103}$$

The free-energy density ψ per unit of reference-volume is then given by

$$\psi(\mathbf{C}_e, c_d, J_g) = J_g\, \psi_g(\mathbf{C}_e, c_d, J_g)\,, \quad J_e = \hat{J}_e(c_d, J_g)\,. \tag{3.4.104}$$

It is important to remark that the volumetric constraint must be included in the definition of the energy; to account for it, we relax (3.4.104) by adding a term which

enforces equation $(3.4.99)_2$:

$$\psi_r(\mathbf{C}_e, c_d, J_g, p) = \psi(\mathbf{C}_e, c_d, J_g) - p\,[J_d - \hat{J}_d(c_d, J_g)]\,. \tag{3.4.105}$$

The pressure p represents the reaction to the volumetric constraint: it maintains the volume change due to displacement, $J_d = \det \mathbf{F}_d$, equals to $J_d = \hat{J}_d(c_d, J_g)$, which is due to both growth and solvent uptake.

The function ψ_r is called the Lagrangian function associated to the energy ψ, while p is the Lagrangian multiplier which measures the sensitivity of the minimum energy to a change in the constraint. The key features of ψ, or ψ_r, are the followings:

1. ψ is a density per unit volume of the dry polymer;
2. the elastic contribution hampers swelling;
3. the mixing contribution favors swelling;
4. the volumetric constraint (3.4.98) implies that any elastic change of volume J_e is due to uptake or release of solvent.

Dissipation principle

The dissipation principle that we enforce, based on [129] and the successive developments for the growth theory [120], and the swelling theory [66], deals with the actual external power, that is, the outer power expended along actual velocities $(\mathbf{v}, \mathbb{V}, \dot{c}_d)$; in our model the outer power is the sum of a mechanical power $\mathcal{P}_{e_{mech}}$ and a chemical one $\mathcal{P}_{e_{chem}}$. Let $d\mathcal{P}_e$ denote the elementary working; the working balance (3.4.95) yields a relation between the outer and the inner mechanical power, that is

$$\begin{aligned} d\mathcal{P}_{e_{mech}}(\mathbf{v}, \mathbb{V}) &= -d\mathcal{P}_{i_{mech}}(\mathbf{v}, \mathbb{V}) \\ &= (\mathbf{S} \cdot \dot{\mathbf{F}}_d - \mathbb{C} \cdot \mathbb{V})\, dV_d\,. \end{aligned} \tag{3.4.106}$$

Analogously, the balance of solvent mass (3.4.91) yields a relation between the flux $\mathbf{h}_d$ and the concentration rate $\dot{c}_d$, thus

$$\begin{aligned} d\mathcal{P}_{e_{chem}}(\dot{c}_d) &= \mu\, q_d\, dA_d = -\mu\, \mathbf{h}_d \cdot \mathbf{m}\, dA_d \\ &= -\mathrm{div}(\mu\, \mathbf{h}_d)\, dV_d \\ &= -(\mu\, \mathrm{div}\mathbf{h}_d + \mathbf{h}_d \cdot \nabla\mu\,)\, dV_d \\ &= (\mu\, \dot{c}_d - \mathbf{h}_d \cdot \nabla\mu\,)\, dV_d\,. \end{aligned} \tag{3.4.107}$$

Let us note that both $\mathcal{P}_{e_{mech}}$ and $\mathcal{P}_{e_{chem}}$ may contain, by definition, boundary densities; our goal is to represent them as volume densities, so that they can be added to the energy density. To do so, we must consider elementary quantities, and use the divergence theorem to transform surface densities into volume ones, as done in equating $(3.4.107)_1$ to $(3.4.107)_2$.

The dissipation principle states that, along any realizable process $\tau \mapsto (f_d, Fb_g, c_d)$, the time rates of the elementary free energy $\psi\, dV_d$ must be less or equal than the elementary outer-working expended along the same process:

$$\begin{aligned} \frac{\partial}{\partial t}(\psi(\mathbf{C}_e, \mathbf{F}_g, c_d)\, dV_d) &\leq d\mathcal{P}_e(\mathbf{v}, \mathbb{V}, \dot{c}_d) \\ &= d\mathcal{P}_{e_{mech}}(\mathbf{v}, \mathbb{V}) + d\mathcal{P}_{e_{chem}}(\dot{c}_d)\,. \end{aligned} \tag{3.4.108}$$

We can now write the local form of the dissipation principle by inserting (3.4.106) and (3.4.107) into (3.4.108), and dropping the volume element dV_d; by using the relaxed energy (3.4.105), we have

$$\dot{\psi}_r(\mathbf{C}_e, \mathbf{F}_g, c_d, p) \leq \mathbf{S} \cdot \dot{\mathbf{F}}_d - \mathbb{C} \cdot \mathbb{V} + \mu\, \dot{c}_d - \mathbf{h}_d \cdot \nabla \mu\,, \tag{3.4.109}$$

From (3.4.104), it follows

$$\dot{\psi}_r = \dot{J}_g\, \psi_g + J_g\, \dot{\psi}_g - p\,(\dot{J}_d - \dot{\hat{J}}_d) - \dot{p}\,(J_d - \hat{J}_d)\,. \tag{3.4.110}$$

To ease the evaluation of the energy rate $\dot{\psi}_r$, we list some useful formulas

$$\begin{aligned} &\dot{\psi}_{ge} = \frac{\partial \psi_{ge}}{\partial \mathbf{C}_e} \cdot \dot{\mathbf{C}}_e\,, \quad \dot{\psi}_{gm} = \frac{\partial \psi_{gm}}{\partial c_d}\, \dot{c}_d + \frac{\partial \psi_{gm}}{\partial J_g}\, \dot{J}_g\,, \\ &\dot{J}_d = \mathbf{F}_d^* \cdot \dot{\mathbf{F}}_d\,, \quad \dot{J}_g = \mathbf{F}_g^* \cdot \dot{\mathbf{F}}_g = J_g\, \mathbf{I} \cdot \mathbb{V}\,, \\ &\dot{\mathbf{C}}_e = 2\,\mathrm{sym}\,\mathbf{F}_e^T\, \dot{\mathbf{F}}_e = 2\,\mathrm{sym}\,\mathbf{F}_e^T\,(\dot{\mathbf{F}}_d\, \mathbf{F}_g^{-1} - \mathbf{F}_e\, \mathbb{V})\,, \end{aligned} \tag{3.4.111}$$

By collecting homologous terms, there follows three different contributions to the power expenditure, plus the volumetric constraint

$$\begin{aligned} \dot{\psi}_r \;=\; & \underbrace{\left(2\,\mathbf{F}_e\, \frac{\partial \psi_{ge}}{\partial \mathbf{C}_e}\, \mathbf{F}_g^* - p\, \mathbf{F}_d^*\right)}_{\mathbf{S}_d \text{ (reference stress)}} \cdot \dot{\mathbf{F}}_d \\ & + \underbrace{\left(J_g\, \frac{\partial \psi_{gm}}{\partial c_d} + p\Omega\right)}_{\mu_d \text{ (chemical potential)}}\, \dot{c}_d \\ & + \underbrace{J_g \left[\left(\psi_g + J_g\, \frac{\partial \psi_{gm}}{\partial J_g} + p\right) \mathbf{I} - 2\,\mathbf{C}_e \frac{\partial \psi_{ge}}{\partial \mathbf{C}_e}\right]}_{\mathbb{E} \text{ (Eshelbian coupling)}} \cdot \mathbb{V} \\ & - \underbrace{(J_d - \hat{J}_d)}_{\text{constraint}}\, \dot{p}\,. \end{aligned} \tag{3.4.112}$$

The previous representation of the energy rate prompts us with three constitutive relations involving all the three state variables, plus the pressure: one for the reference stress $\mathbf{S}_d = \mathbf{S}_d(\mathbf{F}_e, \mathbf{F}_g, p)$, with:

$$\mathbf{S}_d = 2\,\mathbf{F}_e\, \frac{\partial \psi_{ge}}{\partial \mathbf{C}_e}\, \mathbf{F}_g^* - p\, \mathbf{F}_d^*\,; \tag{3.4.113}$$

a second one for the chemical potential $\mu_d = \mu_d(\mathbf{F}_g, c_d, p)$:

$$\mu_d = J_g\, \frac{\partial \psi_{gm}}{\partial c_d} + p\Omega\,; \tag{3.4.114}$$

and a last one for the Eshelby tensor $\mathbb{E} = \mathbb{E}(\mathbf{F}_d, \mathbf{F}_g, c_d, p)$:

$$\mathbb{E} = J_g \left[\left(\psi_g + J_g\, \frac{\partial \psi_{gm}}{\partial J_g} + p\right) \mathbf{I} - 2\,\mathbf{C}_e \frac{\partial \psi_{ge}}{\partial \mathbf{C}_e}\right]. \tag{3.4.115}$$

It is worth defining the energetic part of both $\mathbf{S}_d$ and μ_b: we write

$$\mathbf{S}_d = \mathbf{S}_e(\mathbf{C}_e, \mathbf{F}_g) - p\,\mathbf{F}_d^*\,, \quad \mu_d = \mu_c(c_d, J_g) + p\,\Omega\,, \tag{3.4.116}$$

with

$$\begin{aligned} &\mathbf{S}_e(\mathbf{C}_e, \mathbf{F}_g) = 2\,\mathbf{F}_e\,\frac{\partial\,\psi_{ge}}{\partial\mathbf{C}_e}\,\mathbf{F}_g^*\,, \quad [\mathbf{S}] = \frac{\mathrm{J}}{\mathrm{m}^3} = \mathrm{Pa}\,; \\ &\mu_c(c_d, J_g) = J_g\,\frac{\partial\,\psi_{gm}}{\partial c_d}\,, \qquad\quad [\mu] = \frac{\mathrm{J}}{\mathrm{mol}} = \frac{\mathrm{Pa\ m}^3}{\mathrm{mol}}\,. \end{aligned} \tag{3.4.117}$$

By assuming the volumetric constraint to be identically satisfied, we can rewrite the inequality (3.4.109) as

$$(\mathbf{S}_d - \mathbf{S}) \cdot \dot{\mathbf{F}}_d + (\mu_d - \mu)\,\dot{c}_d + (\mathbb{E} + \mathbb{C}) \cdot \mathbb{V} + \mathbf{h}_d \cdot \nabla\mu \leq 0\,. \tag{3.4.118}$$

This last representation of the dissipation principle reveals that power can be dissipated in four different ways; by assuming that no dissipation is involved with the first two summands, we have $\mathbf{S} = \mathbf{S}_d$, and $\mu = \mu_d$.

We can now give to the Eshelby tensor (3.4.115) a more useful representation; being

$$\psi_{gm} = \psi_{gm}(\phi) = \psi_{gm}(\phi(J_e)) = \psi_{gm}(\phi(c_d, J_g))\,, \tag{3.4.119}$$

we can compute time rates as follows

$$\dot{\psi}_{gm} = \frac{\partial\psi_{gm}}{\partial J_e}\,\dot{J}_e = \frac{\partial\psi_{gm}}{\partial c_d}\,\dot{c}_d + \frac{\partial\psi_{gm}}{\partial J_g}\,\dot{J}_g\,. \tag{3.4.120}$$

From (3.4.99), we have

$$\frac{\partial\psi_{gm}}{\partial J_e}\,\dot{J}_e = \frac{\partial\psi_{gm}}{\partial J_e}\,\frac{\Omega}{J_g}\,\left(\dot{c}_d - c_d\,\frac{\dot{J}_g}{J_g}\right)\,; \tag{3.4.121}$$

eventually, a comparison with (3.4.120) yields

$$\frac{\partial\psi_{gm}}{\partial c_d} = \frac{\Omega}{J_g}\,\frac{\partial\psi_{gm}}{\partial J_e}\,, \quad \frac{\partial\psi_{gm}}{\partial J_g} = -\frac{\Omega\,c_d}{J_g^2}\,\frac{\partial\psi_{gm}}{\partial J_e}\,. \tag{3.4.122}$$

Inserting this last result into (3.4.115), we can split $\mathbb{E}$ into the sum of a mechanical and a chemical contribution

$$\mathbb{E} = \mathbb{E}_{mech} + \mathbb{E}_{chem}\,, \tag{3.4.123}$$

with

$$\begin{aligned} &\mathbb{E}_{mech} = \psi_e\,\mathbf{I} - \mathbf{F}_e^T\,\mathbf{S}_d\,\mathbf{F}_g^T\,, \quad \psi_e = J_g\,\psi_{ge}\,; \\ &\mathbb{E}_{chem} = (\psi_m - c_d\,\mu_d)\,\mathbf{I}\,, \quad \psi_m = J_g\,\psi_{gm}\,. \end{aligned} \tag{3.4.124}$$

The two summands are coupled through the pressure p which is present in both $\mathbf{S}_d$ and μ_d. The dissipation inequality (3.4.118) reduces to

$$(\mathbb{E} + \mathbb{C}) \cdot \mathbb{V} + \mathbf{h}_d \cdot \nabla\mu \leq 0\,, \tag{3.4.125}$$

to be satisfied for any realizable process $\tau \mapsto (\mathbf{F}_g, c_d)$. The (reduced) dissipation inequality (3.4.125) has to be interpreted as a rule dictating the admissible constitutive

assumptions for the dissipation, that is, for the sum $\mathbb{E} + \mathbb{C}$ and for the flux $\mathbf{h}_d$. To satisfy this inequality, we assume two simple constitutive rules

$$\begin{aligned} \mathbb{E} + \mathbb{C} &= -\mathbf{M}\,\mathbb{V}\,, \\ \mathbf{h}_d &= -\mathbf{D}_d\,\nabla\,(\,\mu_c(c_d) + p\,\Omega\,)\,, \end{aligned} \tag{3.4.126}$$

with the mobility $\mathbf{M}$ and the diffusivity $\mathbf{D}_d = \mathbf{D}_d(\mathbf{F}_d, c_d)$, two positive-definite tensors; dimensional analysis implies

$$[\mathbf{M}] = \frac{\mathrm{J\,s}}{\mathrm{m}^3}\,, \quad [\mathbf{D}_d] = \frac{\mathrm{mol}}{\mathrm{s}}\,\frac{\mathrm{mol}}{\mathrm{J}}\,\frac{1}{\mathrm{m}} = \frac{\mathrm{mol}^2\,\mathrm{s}}{\mathrm{kg\,m}^3}\,. \tag{3.4.127}$$

Growth and swelling processes have their own characteristic times τ_g and τ_s, respectively, which can be estimated by the following ratios

$$\tau_g = \frac{\|\mathbf{M}\|}{\|\mathbb{E}\|}\,, \quad \tau_s = \frac{l^2}{\|\mathbf{D}\|}\,\frac{c_d}{R\,T}\,, \tag{3.4.128}$$

with l a characteristic length, and $\|\cdot\|$ a suitable norm on $\mathbb{L}\mathtt{in}$; the estimate for τ_s is based on the hypothesis that diffusion of solvent is proportion to the solvent concentration, that is, the more the solvent, the larger the diffusion.

3.4.4 Growth & swelling dynamics

We summarize our findings by writing the equations which govern the evolutive process of a growing and swelling body. Our problem consists in finding the process $\tau \to (f_d, \mathbf{F}_g, c_d)$ that satisfies on $\mathcal{B}_d \times \mathcal{T}$ the following balance equations

$$\begin{aligned} 0 &= \operatorname{div}(\mathbf{S}_e(\mathbf{C}_e, \mathbf{F}_g) - p\,\mathbf{F}_g^*) + \mathbf{b}\,, \\ \mathbb{M}\,\mathbb{V} &= \mathbb{B}_o - \mathbb{E}_o(f_d, \mathbf{F}_g, c_d)\,, \\ \dot{c}_d &= \operatorname{div}[\mathbf{D}\,\nabla(\mu(c_d, J_g) + \Omega\,p)]\,, \end{aligned} \tag{3.4.129}$$

plus the boundary conditions on $\partial\mathcal{B}_d \times \mathcal{T}$

$$\begin{aligned} &(\mathbf{S}_e(\mathbf{C}_e, \mathbf{F}_g) - p\,\mathbf{F}_d^*)\mathbf{m} = \mathbf{t} && \text{load control;} \\ &f_d = \bar{f}_d, && \text{position control;} \\ &\mathbf{D}\,\nabla(\mu(c_d, J_g) + \Omega\,p)\cdot\mathbf{m} = q_d && \text{flux control;} \\ &\mu_c(c_d, J_g) + \Omega\,p = \mu_{\text{ext}} && \text{concentration control;} \end{aligned} \tag{3.4.130}$$

and the initial conditions on $\mathcal{B}_d \times \{0\}$

$$\begin{aligned} &f_d = f_{do} && \text{initial position;} \\ &\mathbf{F}_g = \mathbf{F}_{go} && \text{initial relaxed stance;} \\ &c_d = c_{do}, && \text{initial solvent concentration.} \end{aligned} \tag{3.4.131}$$

Some remarks

- As regards balance equations (3.4.129), time derivatives appear only in $(3.4.129)_{2,3}$; thus, for the first equation time is just a scalar parameter, and what is solved is a sequence of stationary problems parametrized by time. Nonetheless, the whole system of three equation describes the time evolving phenomenon of growth and swelling, when inertia forces are neglected.
- The characteristic times of growth and swelling may be very different from each other; for $\tau_s << \tau_g$ the evolutive phenomenon which is described is very close to the standard swelling. Conversely, for $\tau_s >> \tau_g$, growth is prevailing.
- As far as the boundary conditions (3.4.130), loads and displacements cannot be assigned simultaneously on the same portion of $\partial\mathcal{B}_d$; the same holds for fluxes and solvent concentration.
- As previously noticed, the control of the solvent concentration is done by controlling both the external chemical potential μ_{ext}, and the boundary load $\mathbf{t}$, whose value influences the osmotic pressure p. A simple and common case is when the boundary load is a pressure, $\mathbf{t} = -p_{ext}\,\mathbf{F}_d^*\mathbf{m}$; it follows that we may interpret the boundary condition $(3.4.130)_4$ as an implicit control of c_d through μ_{ext} and p_{ext}.
- Both $\mathbf{M}$ and $\mathbb{B}$ have to be identified with experiments. For $\mathbf{M}$, the only constitutive restriction is that it has to be positive definite; for $\mathbb{B}$ there are not constitutive restrictions.
- Our final, and important, remark is that this theory can describe phenomena where actual volume change are larger or smaller than the volume of solvent uptaken; this behavior is typical of many complex polymers (as example, wood, just to cite one).

Flory-Rehner energy

We assume the Flory-Rehenr free energy, proposed to describe the interaction between a solvent and a polymer matrix [109]. The elastic energy is Neo-hookean, a common and simple choice for soft materials:

$$\psi_{ge}(\mathbf{C}_e) = \frac{1}{2}G_d\ (\mathbf{C}_e\cdot\mathbf{I}-3)\ , \quad [G_d] = \mathrm{J/m^3}\,. \tag{3.4.132}$$

From (3.4.132, 3.4.113), it follows the representation for $\mathbf{S}_d$

$$2\,\mathbf{F}_e\,\frac{\partial\psi_{ge}}{\partial\mathbf{C}_e} = G\,\mathbf{F}_e \quad \Rightarrow \quad \mathbf{S}_d = G\,\mathbf{F}_e\,\mathbf{F}_g^* - p\,\mathbf{F}_d^*\,. \tag{3.4.133}$$

or, defined the strain $\mathbf{C}_g = \mathbf{F}_g^T\,\mathbf{F}_g$,

$$\mathbf{S}_d = G\,J_g\,\mathbf{F}_d\,\mathbf{C}_g^{-1} - p\,\mathbf{F}_d^*\,. \tag{3.4.134}$$

We note the $\mathbf{C}_g$ represents a *target metric* [124–126], that is, if the body realizes a motion such that $\mathbf{F}_d = \mathbf{F}_g$, then $\mathbf{C}_e = \mathbf{I}$, and $\psi_{ge} = 0$.

What is peculiar of gel models is the representation formula for the mixing energy ψ_{gm}; here we assume the *Flory-Huggins* mixing energy [107, 108], defined as the

sum of an entropic plus an enthalpic term, both depending on ϕ. Being $\phi = 1/J_e$, we may represent the mixing energy in terms of J_e as follows:

$$\psi_{gm}(J_e) = \frac{R\,T}{\Omega}\,h(J_e)\,, \quad [h] = 1\,, \tag{3.4.135}$$

with

$$h(J_e) = \underbrace{(J_e - 1)\,\ln\Big(\frac{J_e - 1}{J_e}\Big)}_{\text{entropic}} + \underbrace{\chi(T)\,\frac{J_e - 1}{J_e}}_{\text{enthalpic}}\,. \tag{3.4.136}$$

Here R is the universal gas constant, T the absolute temperature; the mixing energy has only two chemical parameters; apart form Ω, already introduced, we have the polymer-solvent disaffinity χ, a non dimensional quantity, $[\chi]$=1, possibly depending on the temperature. The parameter χ is specific of each solvent-polymer pair, and represents the dis-affinity between polymer and solvent:

$$\begin{aligned} \text{high } \chi \quad &\Rightarrow \quad \text{solvent is expelled (de-swelling);} \\ \text{low } \chi \quad &\Rightarrow \quad \text{solvent is attracted (swelling).} \end{aligned} \tag{3.4.137}$$

Being $[RT]$ =J/mol, we have $[RT/\Omega]$ =J/m^3, that is, the ratio $R\,T/\Omega$ has the same role for the chemical energy as that of the shear modulus G for the elastic energy. We also note that (3.4.135) implies:

$$\begin{aligned} \phi = 1/J_e \text{ high (more polymer)} \quad &\Rightarrow \quad \text{low enthalpy;} \\ \phi = 1/J_e \text{ low (more solvent)} \quad &\Rightarrow \quad \text{low entropy.} \end{aligned} \tag{3.4.138}$$

The energy $\psi_{gm}(J_e)$ is monotone decreasing for $\chi \in (0, 1/2)$: for such a range, solvent uptake is always favorable; for $\chi > 1/2$, $\psi_{gm}(J_e)$ has a minimum in between $(1, +\infty)$, that is, for $\phi \in (0, 1)$. From (3.4.117, 3.4.135), we have

$$\mu_c = R\,T\,\left[\log\left(\frac{c_d\,\Omega}{J_g + c_d\,\Omega}\right) + \frac{J_g\,(J_g + c_d\,\Omega + \chi\,J_g)}{(J_g + c_d\,\Omega)^2}\right]\,. \tag{3.4.139}$$

Once the constitutive prescription for μ_c has been obtained by (3.4.117), that is, through the derivative of ψ_{gm} with respect to c_d, we can use (3.4.99) to represent it as function of J_e as follows

$$\mu_c = \mu_c(J_e) = R\,T\,\left[\log\left(\frac{J_e - 1}{J_e}\right) + \frac{\chi + J_e}{J_e^2}\right]\,. \tag{3.4.140}$$

Growth or swelling

The classical swelling model as in [66] is recovered by assuming $\mathbf{F}_g \equiv \mathbf{I}$, thus nullifying equation (3.4.129)$_2$. The growth model as in [120] is recovered with $J_e \equiv 1$, an assumption that describes an elastically incompressible material: it yields $c_d \equiv 0$, and equation (**??**)$_3$ is void; moreover, both the chemical energy and the chemical part of the Eshelby tensor are null. The following scheme summarizes the two cases; see

also Fig. 3.25:

$$
\begin{aligned}
&\text{Swelling: } \mathbf{F}_g \equiv \mathbf{I} \quad \Rightarrow \quad \begin{cases} \mathbf{F}_e = \mathbf{F}_d\,; \\ J_e = J_d = 1 + \Omega\, c_d\,; \\ \mathbb{V} = 0\,, \text{ no remodelling actions;} \end{cases} \\
&\text{Growth: } J_e \equiv 1 \quad \Rightarrow \quad \begin{cases} J_d = J_g\,; \\ c_d = 0 \;\Rightarrow\; \psi_{gm} = \mathbb{E}_{chem} = 0\,; \\ \dot{c}_d = 0\,, \text{ no solvent diffusion.} \end{cases}
\end{aligned}
\tag{3.4.141}
$$

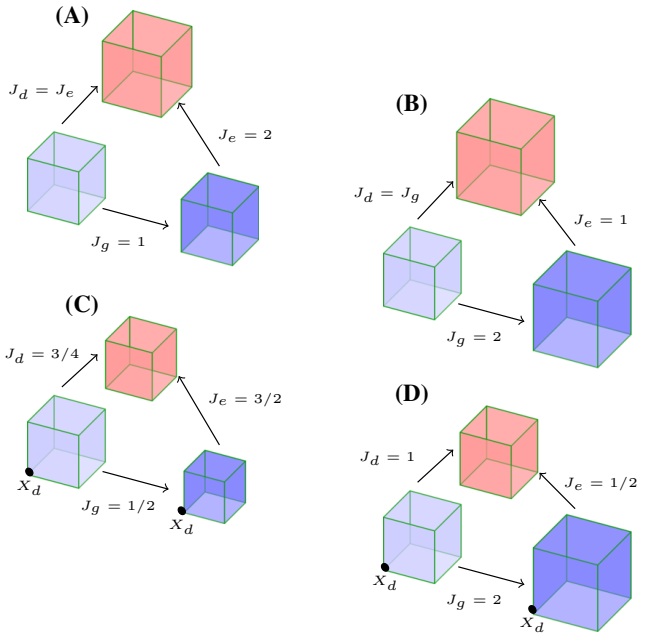

FIGURE 3.25: Different cases of swelling and growth with a cartoon of the different volume-elements: dry volume is light blue, relaxed volume is dark blue, and actual volume is red. A) With $\mathbf{F}_g \equiv \mathbf{I}$, we have the standard Flory-Rehner model of swelling: the actual change in volume J_d is entirely due to solvent uptake. B) With $J_e \equiv 1$, we have the growth model for incompressible materials: the actual change in volume J_d is entirely due to growth. C) Growth yields a reduction of relaxed volume which is not compensated by swelling: the actual volume is smaller than the volume of absorbed solvent. D) This case is ruled out of our theory as $J_e < 1$; in fact, also the relaxed volume is dry, and no solvent can be expelled from it.

3.4.5 Steady states

A solid may growth and swell; within our model, the final state is regulated by the external chemical potential, the applied loads, and the remodelling actions.

The system (3.4.129), under the request $\dot{c}_d = \mathbb{V} = 0$, describes steady states, that is constant in time. To discuss a simple instance of a steady state, we assume no bulk forces, $\mathbf{b} = 0$, and $(\mathbf{F}_d, \mathbf{F}_g, p)$ to be homogeneous; thus, we have to solve the

following system

$$\begin{aligned} &\mathbf{S}_d = G_d\,\mathbf{F}_e\,\mathbf{F}_g^* - p\,\mathbf{F}_d^* = \mathbf{T}\,\mathbf{F}_d^*\,, \\ &\mu_d = \mu_c(J_e) + \Omega\,p = \mu_{\text{ext}}\,, \\ &\mathbb{E} = \mathbb{E}(\mathbf{F}_d, \mathbf{F}_g, p) = \mathbb{B}\,, \end{aligned} \tag{3.4.142}$$

with $\mathbf{T}$ the homogeneous stress state induced by the boundary loads, μ_{ext} the chemical potential of the environment, and $\mathbb{B}$ the outer remodelling action. It is worth noting that, thanks to the volumetric constraint (3.4.99), instead of the state variable c_d, it appears in the system the pressure p.

Free swelling and growing

We consider a solid $\mathcal{B}_d$ with no loads, and with an external chemical potential equal to μ_{ext}. Homogeneous states, with isotropic growth and swelling, are characterized by the following hypotheses:

$$\begin{aligned} &\text{null stress:} && \mathbf{T} = 0\,, \\ &\text{homogeneous chemical potential:} && \mu_c(J_e) + p\,\Omega = \mu_{\text{ext}}\,, \\ &\text{spherical deformation:} && \mathbf{F}_d = \lambda_d\,\mathbf{I} = J_d^{1/3}\,\mathbf{I}\,, \\ &\text{spherical growth:} && \mathbf{F}_g = \lambda_g\,\mathbf{I} = J_g^{1/3}\,\mathbf{I}\,, \end{aligned} \tag{3.4.143}$$

and the state of the system can be represented in the (J_d, J_g) plane. Using (3.4.143), we can solve $(3.4.142)_1$ for p

$$\mathbf{S}_d = \lambda_d\,(G_d\,\lambda_g - \lambda_d\,p)\,\mathbf{I} = 0 \quad \Rightarrow \quad p = G_d\,J_e^{-1/3}\,, \tag{3.4.144}$$

and use this result to rewrite $(3.4.142)_{2,3}$ as a system of two scalar equations for J_d and J_g (being $J_e = J_d\,J_g^{-1}$)

$$\begin{aligned} &\mu_c(J_e) + \Omega\,G_d\,J_e^{-1/3} = \mu_{\text{ext}}\,, \\ &\mathbb{E}_{chem}(J_d, J_g) + \mathbb{E}_{mech}(J_d, J_g) = \mathbb{B}\,, \end{aligned} \tag{3.4.145}$$

where, given (3.4.143), it holds

$$\begin{aligned} \mathbb{E}_{chem} &= G_d\,(J_d - J_g)\left[\epsilon_{cm}\,\frac{\chi\,(J_e - 1) - J_e}{J_e^2} - J_e^{-1/3}\right]\mathbf{I}\,; \\ \mathbb{E}_{mech} &= G_d\,\frac{3}{2}\,J_g\,(J_e^{2/3} - 1)\,\mathbf{I}\,, \quad \text{with} \quad \epsilon_{cm} = \frac{R\,T}{\Omega\,G_d}\,. \end{aligned} \tag{3.4.146}$$

The parameter ϵ_{cm} in $\mathbb{E}_{chem}$ represents the ratio between the chemical energy and the elastic one; being $R = 8.314$ J/(mol K), for a typical solvent such as alcohol ($\Omega \simeq 6 \times 10^{-5}$ m^3/mol) at $T = 293$ K, we have $R\,T/\Omega \simeq 4.06 \times 10^7$ J/m^3. If follows that for soft materials $\epsilon_{cm} >> 1$, while for hard materials $\epsilon_{cm} << 1$.

We can use system (3.4.145) to find the steady state (J_d, J_g) corresponding to the pair $(\mu_{\text{ext}}, \mathbb{B})$: at first, given the external chemical potential μ_{ext}, we solve equation $(3.4.145)_1$ for J_e; then, given the remodelling force $\mathbb{B}$, and using the previous result, we solve equation $(3.4.145)_2$ for J_g, or J_d. We note that steady growth, $\mathbb{V} \equiv 0$, can be realized also also with $\mathbb{B} \equiv 0$ and $\mathbb{E}_{mech} = -\mathbb{E}_{chem}$.

Fig.3.26A shows the isolines μ_{ext} (red) and $\mathbb{B}$ (blue), while Fig.3.26B shows the isolines J_g (red) and J_d (blue) in the plane $(\mu_{\text{ext}}, \mathbb{B})$; as already noticed, the states above the line $J_d = J_g$ are unattainable: this line denotes relaxed and dry states, corresponding to $\mu_{\text{ext}} = -\infty$ and $\mathbb{B} = 0$.

Both panels of Fig.3.26 contains five states labelled from 1 (dry-reference) to 5, representing two noteworthy behaviors: the horizontal path $1 \to 2 \to 3$ is a swelling without growth, and volume change is entirely due to solvent uptake; the vertical path $1 \to 4 \to 5$ represents a solvent uptake which is compensated exactly by growth, thus producing a null change of the actual volume. Another interesting fea-

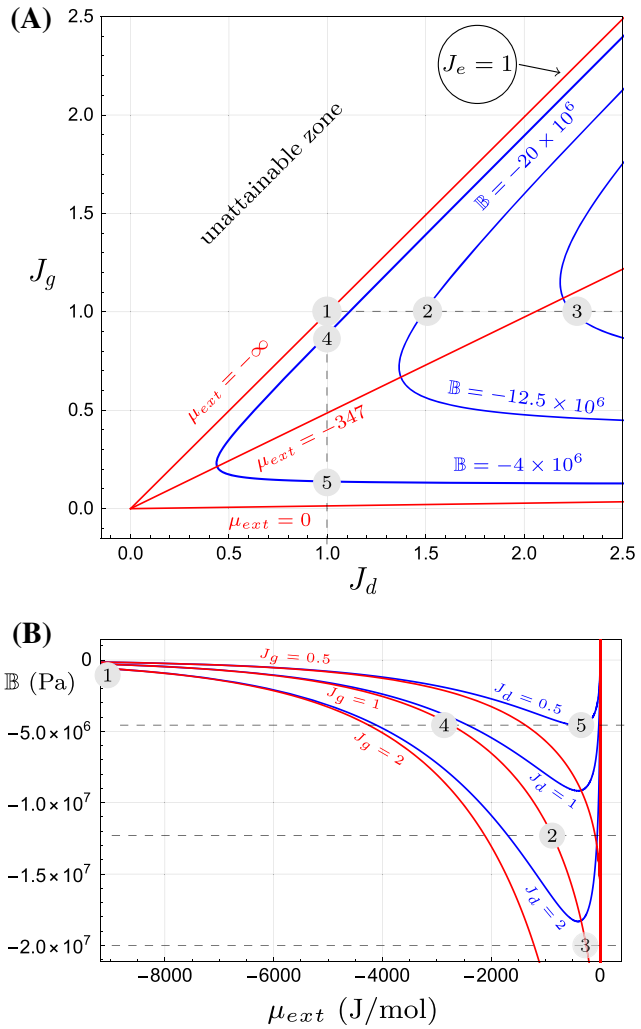

FIGURE 3.26: (A) Isolines μ_{ext} (red) and $\mathbb{B}$ (blue) in the (J_d, J_g) plane; points $1 \sim 5$ represent different states: 1 corresponds to the dry-reference; 2 and 3 to swelling without growth, that is, to a volume change entirely due to solvent uptake; 4 and 5 to a growth (in this case, a volume reduction) which compensates exactly the solvent uptake. As already noticed, the states above the line $J_d = J_g$ are unattainable: this line denotes relaxed and dry states, corresponding to $\mu_{\text{ext}} = -\infty$. (B) Paths of iso-swelling and iso-growing processes in the plane $(\mu_{\text{ext}}, \mathbb{B})$; the same states $1 \sim 5$ of panel (A) are also reported here. Results are obtained with $R = 8.314$ J/(mol K), $T = 293$ K, $\Omega = 6 \times 10^{-5}$ m^3/mol, $G_d = 10^4$ Pa.

ture is shown in Fig.3.27; from (3.4.100), it follows that $J_d - J_g$ measures the solvent

volume per unit of dry-reference volume. Thus, by comparing states in the plane (J_d, J_g), it is quite easy to compute the volume of solvent which enter or exit the body: any state change along a line parallel to the line $J_d = J_e$ yields no solvent variation; any state change along a line orthogonal to the line $J_d = J_e$ yields maximum solvent variation, with uptake in the direction of decreasing J_g, and release in the opposite direction. Let $(J_d, J_g)_i$, $i = 1, 2$, be two different states, and let θ be the angle between the vector $\mathbf{a} = (J_d, J_g)_2 - (J_d, J_g)_1$ and the horizontal direction; we have

$$J_{d2} - J_{d1} = \|\mathbf{a}\| \cos\theta\,, \quad J_{g2} - J_{g1} = \|\mathbf{a}\| \sin\theta\,; \tag{3.4.147}$$

it follows

$$V_s = \frac{dV_{sol2} - dV_{sol1}}{dV_d} = \|\mathbf{a}\| \left(\cos\theta - \sin\theta\right), \tag{3.4.148}$$

where dV_{soli} is the elementary solvent volume of state $(J_d, J_g)_i$, and V_s the solvent-volume difference between the two states. For $\theta = \pi/4 = \pi/4 + \pi$ we do not have exchange of solvent; maximum expulsion and absorption of solvent are obtained on $\theta = 3/4\,\pi$ and $\theta = 7/4\,\pi$, respectively. Fig.3.27 shows the amount of solvent volume which is involved when considering as initial state a swollen state $J_d = 2$, $J_g = 1$. Fig.3.28 contains a zoom of the bottom-right quadrant of Fig.3.27, and shows

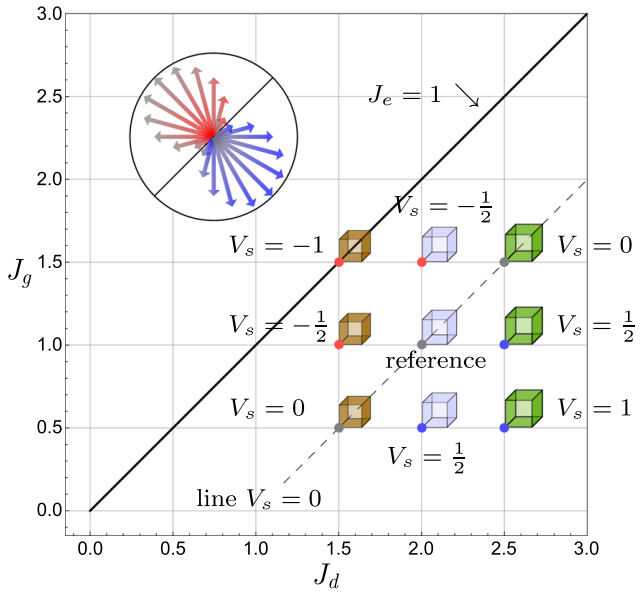

FIGURE 3.27: Nine different states on the (J_d, J_g) plane. We assume the swollen state $J_d = 2, J_g = 1$ as reference, and we evaluate the change in solvent content for the other eight states with respect to this reference. You may notice that states having the same volume (those aligned along vertical columns) may have different values of V_s. Formula (3.4.148) is represented by the circle at top left; arrows length denotes the magnitude of V_s, while red and blue colors indicate solvent expulsion, and absorption, respectively.

an example of bulking, that is, a permanent volume growth: a solid, after a process of swelling and drying, retains some of its swollen volume. Given a reference state (1), we may consider solvent uptake with swelling up to state (2); then, upon drying, the process ends at state (3), when the same amount of solvent which has been absorbed leaves the solids. The increase of J_d, that is, of actual volume, from (1) to (3)

is due to growth. Any state along the line $V_s = 0$ contains the same amount of solvent contained in the reference; thus, any state along this line may represent a final stage of bulking, with different degrees of permanent growth. Bulking is a typical phenomenon observed in wood [10]. Our model represents a proposal to merge the

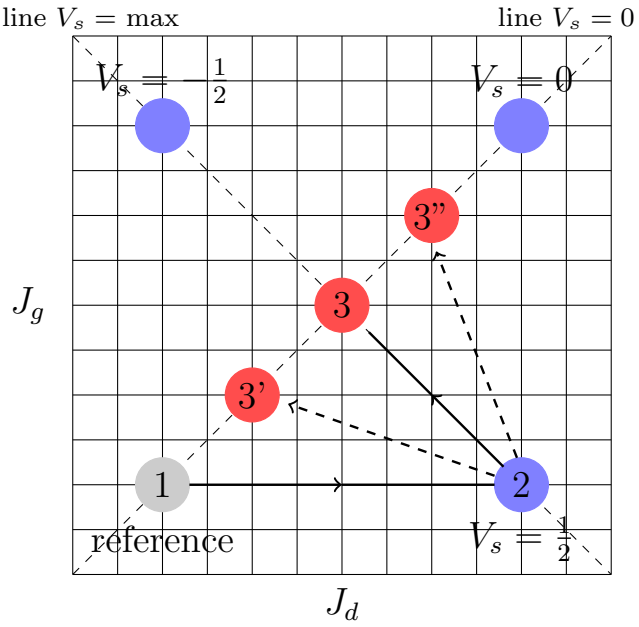

FIGURE 3.28: Any path from the swollen reference (1) to a state along the line $V_s = 0$ (3, 3′, 3″) represents a bulking, that is, the final volume upon drying is larger than than the initial volume prior to swelling. As example, solvent uptake from 1 to 2 is equal to the solvent release from 2 to 3 (or 2 to 3′, or 2 to 3″).

theory of swelling, related to solvent uptake, with the notion of growth as change in the zero-stress reference state. The remodelling actions, the associated balance law, and the chemo-mechanical coupling which governs the evolution of the system have a primary role in this model. A key feature of this model is the ability to describe some interesting aspects of volume deformations; as example, the actual volume change of solids can be greater or smaller than volume of the solvent which is exchanged, an important class of phenomena that is observed very often. As example, such phenomena are typical of cellulosic materials: here, the change of moisture content yields noticeable change of volume, which in general, is not equal to the mass of the solvent exchanged. Another important phenomenon for wood is bulking, mentioned in the introduction; in such a case there is the need to describe the permanent change of volume that arises upon cycles of wetting and drying. Our proposal is to model bulking as a change of the ground state of woods cells, a change that is driven by the chemo-mechanical coupling between solvent uptake and growth.

Future directions are the identification of ad-hoc remodelling actions capable of describing some selected experimental results; in particular, we seek for constitutive prescriptions for both the mobility $\mathbf{M}$ and the outer action $\mathbb{B}$, relating the chemistry of the pair solvent-solid, to the dynamics of growth and swelling. Other interesting issues which are worth investigating are the anisotropic growth, and the compatibility of growth.

Chapter 4

Conclusions

Smart materials and the transformation of energy are central topics in many scientific fields. A complete understanding of such materials and the efficiency of the energy conversion will play a primary role in the future development of the society. In this context, the present work contributes for a more complete understanding of such materials, theoretically, numerically and experimentally. Some issues of theoretical models of smart materials are investigated in detail, such as the role of plane state assumptions in not homogeneous piezoelectric solids. Moreover, the performances of a piezoelectric sheet immersed in a fluid flow are studied. An optimal load resistance is found and it depends on the inlet fluid velocity. Experimental results were compared with a complex numerical model which involves the physics of fluids, solids and electrostatics.

Hydrogels and the control of their shape, which may be used to realize innovative actuators, are investigated through a numerical model and verified with some analytical formula. Moreover, in this thesis, two high power mechanisms are presented: a first high power mechanism which is realized through the competition between an adhesion energy and an elastic energy, and a second high power mechanism which was observed in nature and uses a change of phase to realize the power leverage. Finally, it is presented a model which couples the theory of swelling, describing the effects of solvent uptake in polymeric solids, with that of growing, describing the change of the relaxed state in a continuum body. This phenomenon often occurs in wood-like materials which today are used for different applications in engineering such an autonomous shading system.

List of Publications

1. **M. Curatolo**, M. La Rosa, P. Prestininzi.

   On the validity of plane state assumptions in the bending of bimorph piezoelectric cantilevers, *Journal of Intelligent Material Systems and Structures* (accepted), (2019).

2. **M. Curatolo**

   Effective negative swelling of hydrogel-solid composites *Extreme Mechanics Letters*, (2018).

   Doi:10.1016/j.eml.2018.10.010

3. **M. Curatolo**, M. La Rosa, P. Prestininzi.

   Energy harvesting in a fluid flow using piezoelectric materials, Proc. European COMSOL Conference, Lausanne, Switzerland (2018).

4. **M. Curatolo**, P. Nardinocchi.

   Swelling-induced bending and pumping in homogeneous thin sheets. *Journal of Applied Physics*, (2018).

   Doi:10.1063/1.5043580

5. **M. Curatolo**, P. Nardinocchi, L. Teresi.

   Driving water cavitation into a hydrogel cavity. *Soft Matter*, (2018).

   Doi:10.1039/C8SM00100F

6. **M. Curatolo**, S. Gabriele, L. Teresi.

   Swelling and Growth: a Constitutive Framework for Active Solids. *Meccanica*, (2017).

   Doi: 10.1007/s11012-017-0629-x.

Bibliography

[1] Alper Erturk and Daniel J Inman. *Piezoelectric energy harvesting*. John Wiley & Sons, 2011.

[2] Henry A Sodano, Daniel J Inman, and Gyuhae Park. "A review of power harvesting from vibration using piezoelectric materials". In: *Shock and Vibration Digest* 36.3 (2004), pp. 197–206.

[3] Shashank Priya and Daniel J Inman. *Energy harvesting technologies*. Vol. 21. Springer, 2009.

[4] JD Adams et al. "Nanowatt chemical vapor detection with a self-sensing, piezoelectric microcantilever array". In: *Applied Physics Letters* 83.16 (2003), pp. 3428–3430.

[5] Sebastian Pobering and Norbert Schwesinger. "A Novel Hydropower Harvesting Device". In: *International Conference on MEMS, NANO and Smart Systems(ICMENS)*. Vol. 00. Aug. 2004, pp. 480–485. DOI: 10.1109/ICMENS.2004.14. URL: doi.ieeecomputersociety.org/10.1109/ICMENS.2004.14.

[6] JM McCarthy et al. "Fluttering energy harvesters in the wind: A review". In: *Journal of Sound and Vibration* 361 (2016), pp. 355–377.

[7] Huseyin Dogus Akaydin, Niell Elvin, and Yiannis Andreopoulos. "Energy harvesting from highly unsteady fluid flows using piezoelectric materials". In: *Journal of Intelligent Material Systems and Structures* 21.13 (2010), pp. 1263–1278.

[8] Santiago Orrego et al. "Harvesting ambient wind energy with an inverted piezoelectric flag". In: *Applied Energy* 194 (2017), pp. 212–222.

[9] Masao Doi. "Gel Dynamics". In: *J. Phys. Soc. Jpn.* 78.5 (2009), p. 052001. DOI: 10.1143/JPSJ.78.052001. URL: http://jpsj.ipap.jp/link?JPSJ/78/052001/.

[10] Alfred Joaquim Stamm. "Wood and cellulose science." In: *Wood and cellulose science.* (1964).

[11] Paul Calvert. "Hydrogels for soft machines". In: *Advanced materials* 21.7 (2009), pp. 743–756.

[12] Marianne E Harmon, Mary Tang, and Curtis W Frank. "A microfluidic actuator based on thermoresponsive hydrogels". In: *Polymer* 44.16 (2003), pp. 4547–4556.

[13] Chiara Vailati et al. "An autonomous shading system based on coupled wood bilayer elements". In: *Energy and Buildings* 158 (2018), pp. 1013–1022.

[14] Gabriel Lippmann. "Principe de la conservation de l'électricité, ou second principe de la théorie des phénomènes électriques". In: *J. Phys. Theor. Appl.* 10.1 (1881), pp. 381–394.

[15] JJ Allen and AJ Smits. "Energy harvesting eel". In: *Journal of fluids and structures* 15.3-4 (2001), pp. 629–640.

[16] Steven R Anton and Henry A Sodano. "A review of power harvesting using piezoelectric materials (2003–2006)". In: *Smart materials and Structures* 16.3 (2007), R1.

[17] S P? Beeby, M J? Tudor, and NM White. "Energy harvesting vibration sources for microsystems applications". In: *Measurement science and technology* 17.12 (2006), R175.

[18] P Muralt, RG Polcawich, and S Trolier-McKinstry. "Piezoelectric thin films for sensors, actuators, and energy harvesting". In: *MRS bulletin* 34.9 (2009), pp. 658–664.

[19] Heung Soo Kim, Joo-Hyong Kim, and Jaehwan Kim. "A review of piezoelectric energy harvesting based on vibration". In: *International journal of precision engineering and manufacturing* 12.6 (2011), pp. 1129–1141.

[20] Johan Lidman et al. *Apparatus for determining the actual status of a piezoelectric sensor in a medical implant*. US Patent 6,829,507. 2004.

[21] J McLaughlin et al. "Piezoelectric sensor determination of arterial pulse wave velocity". In: *Physiological measurement* 24.3 (2003), p. 693.

[22] Hisao Fukunaga, Ning Hu, and Fu-Kuo Chang. "Structural damage identification using piezoelectric sensors". In: *International journal of solids and structures* 39.2 (2002), pp. 393–418.

[23] Nam-Trung Nguyen and Thai-Quang Truong. "A fully polymeric micropump with piezoelectric actuator". In: *Sensors and Actuators B: Chemical* 97.1 (2004), pp. 137–143.

[24] Jan G Smits. "Piezoelectric micropump with three valves working peristaltically". In: *Sensors and Actuators A: Physical* 21.1-3 (1990), pp. 203–206.

[25] Nesbitt W Hagood, Walter H Chung, and Andreas Von Flotow. "Modelling of piezoelectric actuator dynamics for active structural control". In: *Journal of Intelligent Material Systems and Structures* 1.3 (1990), pp. 327–354.

[26] Yoshikazu Takahashi and Masahiko Suzuki. *Piezoelectric ink jet printer using laminated piezoelectric actuator*. US Patent 5,402,159. 1995.

[27] S Adhikari, MI Friswell, and DJ Inman. "Piezoelectric energy harvesting from broadband random vibrations". In: *Smart Materials and Structures* 18.11 (2009), p. 115005.

[28] A Mehmood et al. "Piezoelectric energy harvesting from vortex-induced vibrations of circular cylinder". In: *Journal of Sound and Vibration* 332.19 (2013), pp. 4656–4667.

[29] Michael Peigney and Dominique Siegert. "Piezoelectric energy harvesting from traffic-induced bridge vibrations". In: *Smart Materials and Structures* 22.9 (2013), p. 095019.

[30] Geffrey K Ottman et al. "Adaptive piezoelectric energy harvesting circuit for wireless remote power supply". In: *IEEE Transactions on power electronics* 17.5 (2002), pp. 669–676.

[31] Henry A Sodano, Daniel J Inman, and Gyuhae Park. "Comparison of piezoelectric energy harvesting devices for recharging batteries". In: *Journal of intelligent material systems and structures* 16.10 (2005), pp. 799–807.

[32] Jayant Sirohi and Inderjit Chopra. "Fundamental understanding of piezoelectric strain sensors". In: *Smart Structures and Materials 1999: Smart Structures and Integrated Systems*. Vol. 3668. International Society for Optics and Photonics. 1999, pp. 528–543.

[33] Meiling Zhu, Emma Worthington, and James AK Njuguna. "Analyses of power output of piezoelectric energy-harvesting devices directly connected to a load resistor using a coupled piezoelectric-circuit finite element method". In: (2009).

[34] Alper Erturk and Daniel J Inman. "An experimentally validated bimorph cantilever model for piezoelectric energy harvesting from base excitations". In: *Smart materials and structures* 18.2 (2009), p. 025009.

[35] Mourad Elhadrouz, Tarak Ben Zineb, and Etienne Patoor. "Constitutive law for ferroelastic and ferroelectric piezoceramics". In: *Journal of intelligent material systems and structures* 16.3 (2005), pp. 221–236.

[36] Chad M Landis. "Fully coupled, multi-axial, symmetric constitutive laws for polycrystalline ferroelectric ceramics". In: *Journal of the Mechanics and Physics of Solids* 50.1 (2002), pp. 127–152.

[37] Paola Nardinocchi, Matteo Pezzulla, and Luca Placidi. "Thermodynamically based multiphysic modeling of ionic polymer metal composites". In: *Journal of Intelligent Material Systems and Structures* 22.16 (2011), pp. 1887–1897.

[38] Marco Rossi and Thomas Wallmersperger. "Thermodynamically consistent three-dimensional electrochemical model for polymeric membranes". In: *Electrochimica Acta* 283 (2018), pp. 1323–1338.

[39] Alper Erturk and Daniel J Inman. "Issues in mathematical modeling of piezoelectric energy harvesters". In: *Smart Materials and Structures* 17.6 (2008), p. 065016.

[40] Alper Erturk et al. "Effect of strain nodes and electrode configuration on piezoelectric energy harvesting from cantilevered beams". In: *Journal of Vibration and Acoustics* 131.1 (2009), p. 011010.

[41] Reinhard Lerch. "Simulation of piezoelectric devices by two-and three-dimensional finite elements". In: *IEEE transactions on ultrasonics, ferroelectrics, and frequency control* 37.3 (1990), pp. 233–247.

[42] Senthil S Vel and RC Batra. "Analysis of piezoelectric bimorphs and plates with segmented actuators". In: *Thin-Walled Structures* 39.1 (2001), pp. 23–44.

[43] Abdulhakim Almajid, Minoru Taya, and Steven Hudnut. "Analysis of out-of-plane displacement and stress field in a piezocomposite plate with functionally graded microstructure". In: *International Journal of Solids and Structures* 38.19 (2001), pp. 3377–3391.

[44] HJ Xiang and ZF Shi. "Static analysis for multi-layered piezoelectric cantilevers". In: *International Journal of Solids and Structures* 45.1 (2008), pp. 113–128.

[45] Horacio Sosa. "Plane problems in piezoelectric media with defects". In: *International Journal of Solids and Structures* 28.4 (1991), pp. 491–505.

[46] Marc S Weinberg. "Working equations for piezoelectric actuators and sensors". In: *Journal of Microelectromechanical Systems* 8.4 (1999), pp. 529–533.

[47] Ronald Krueger et al. "Comparison of 2D finite element modeling assumptions with results from 3D analysis for composite skin-stiffener debonding". In: *Composite Structures* 57.1-4 (2002), pp. 161–168.

[48] S Timoshenko and JN Goodier. "Theory of elasticity. 1951". In: *New York* 412 (), p. 108.

[49] MA Meyers and K. K. Chawla. *Mechanical behavior of materials*. Cambridge University Press, 2008.

[50] Shunong Jiang et al. "Performance of a piezoelectric bimorph for scavenging vibration energy". In: *Smart Materials and Structures* 14.4 (2005), p. 769.

[51] HP Hu, ZJ Cui, and JG Cao. "Performance of a piezoelectric bimorph harvester with variable width". In: *Journal of Mechanics* 23.3 (2007), pp. 197–202.

[52] J-H Park et al. "Tensile test of lead zirconate titanate (PZT)/Platinum (Pt) thin film". In: *Materialwissenschaft und Werkstofftechnik* 42.5 (2011), pp. 478–484.

[53] Michele Curatolo and Luciano Teresi. "The Virtual Aquarium: Simulations of Fish Swimming". In: Proceedings of the European COMSOL Conference, 2015.

[54] Michele Curatolo and Luciano Teresi. "Modeling and simulation of fish swimming with active muscles". In: *Journal of theoretical biology* 409 (2016), pp. 18–26.

[55] Jean Donea et al. "Arbitrary Lagrangian–Eulerian Methods". In: *Encyclopedia of Computational Mechanics Second Edition* (2017), pp. 1–23.

[56] Alan M Winslow. "Numerical solution of the quasilinear Poisson equation in a nonuniform triangle mesh". In: *Journal of Computational Physics* 135.2 (1997), pp. 128–138.

[57] NA Kong et al. "Resistive impedance matching circuit for piezoelectric energy harvesting". In: *Journal of Intelligent Material Systems and Structures* 21.13 (2010), pp. 1293–1302.

[58] Toyoichi Tanaka. "Collapse of gels and the critical endpoint". In: *Physical Review Letters* 40.12 (1978), p. 820.

[59] T Tanaka and ST Sun. "T. Tanaka, ST Sun, Y. Hirokawa, S. Katayama, J. Kucera, Y. Hirose, and T. Amiya, Nature (London) 325, 796 (1987)." In: *Nature (London)* 325 (1987), p. 796.

[60] Michele Curatolo et al. "Transient instabilities in the swelling dynamics of a hydrogel sphere". In: *Journal of Applied Physics* 122.14 (2017), p. 145109.

[61] Mitsuhiro Shibayama and Toyoichi Tanaka. "Volume phase transition and related phenomena of polymer gels". In: *Responsive gels: volume transitions I*. Springer, 1993, pp. 1–62.

[62] Shengqiang Cai and Zhigang Suo. "Mechanics and chemical thermodynamics of phase transition in temperature-sensitive hydrogels". In: *Journal of the Mechanics and Physics of Solids* 59.11 (2011), pp. 2259 –2278. ISSN: 0022-5096. DOI: https://doi.org/10.1016/j.jmps.2011.08.008. URL: http://www.sciencedirect.com/science/article/pii/S0022509611001670.

[63] Z Liu and P Calvert. "Multilayer hydrogels as muscle-like actuators". In: *Advanced Materials* 12.4 (2000), pp. 288–291.

[64] Andreas Richter et al. "Influence of volume phase transition phenomena on the behavior of hydrogel-based valves". In: *Sensors and Actuators B: Chemical* 99.2-3 (2004), pp. 451–458.

[65] Andreas Richter et al. "Micropumps operated by swelling and shrinking of temperature-sensitive hydrogels". In: *Lab on a Chip* 9.4 (2009), pp. 613–618.

[66] A. Lucantonio, P. Nardinocchi, and L. Teresi. "Transient analysis of swelling-induced large deformations in polymer gels". In: *Journal of the Mechanics and Physics of Solids* 61.1 (2013), pp. 205 –218. ISSN: 0022-5096. DOI: http://dx.doi.org/10.1016/j.jmps.2012.07.010. URL: http://www.sciencedirect.com/science/article/pii/S0022509612001548.

[67] Alessandro Lucantonio et al. "Buckling dynamics of a solvent-stimulated stretched elastomeric sheet". In: *Soft Matter* 10 (16 2014), pp. 2800–2804. DOI: 10.1039/C3SM52941J. URL: http://dx.doi.org/10.1039/C3SM52941J.

[68] Wei Hong et al. "A theory of coupled diffusion and large deformation in polymeric gels". In: *Journal of the Mechanics and Physics of Solids* 56.5 (2008), pp. 1779 –1793. ISSN: 0022-5096. DOI: http://doi.org/10.1016/j.jmps.2007.11.010. URL: http://www.sciencedirect.com/science/article/pii/S0022509607002244.

[69] Wei Hong, Zishun Liu, and Zhigang Suo. "Inhomogeneous swelling of a gel in equilibrium with a solvent and mechanical load". In: *International Journal of Solids and Structures* 46.17 (2009), pp. 3282 –3289. ISSN: 0020-7683. DOI: http://dx.doi.org/10.1016/j.ijsolstr.2009.04.022. URL: http://www.sciencedirect.com/science/article/pii/S0020768309001899.

[70] Jiaping Zhang et al. "A finite element method for transient analysis of concurrent large deformation and mass transport in gels". In: *Journal of Applied Physics* 105.9 (2009), p. 093522. DOI: 10.1063/1.3106628. eprint: http://dx.doi.org/10.1063/1.3106628. URL: http://dx.doi.org/10.1063/1.3106628.

[71] Shawn A. Chester and Lallit Anand. "A coupled theory of fluid permeation and large deformations for elastomeric materials". In: *Journal of the Mechanics and Physics of Solids* 58.11 (2010), pp. 1879 –1906. ISSN: 0022-5096. DOI: http://dx.doi.org/10.1016/j.jmps.2010.07.020. URL: http://www.sciencedirect.com/science/article/pii/S0022509610001493.

[72] P J. Flory and J. Rehner. "Statistical Mechanics of Cross-Linked Polymer Networks I. Rubberlike Elasticity". In: *J Chem Phys* 11.11 (1943), pp. 512–520.

[73] P J. Flory and J. Rehner. "Statistical Mechanics of Cross-Linked Polymer Networks II. Swelling". In: *J Chem Phys* 11.11 (1943), pp. 521–526.

[74] Aleksey D Drozdov et al. "Constitutive equations for the kinetics of swelling of hydrogels". In: *Mechanics of Materials* 102 (2016), pp. 61–73.

[75] E.N.M. Cirillo, P. Nardinocchi, and G. Sciarra. "Temperature-driven volume transition in hydrogels: Phase-coexistence and interface localization". In: *International Journal of Non-Linear Mechanics* 81.Supplement C (2016), pp. 115 –121. ISSN: 0020-7462. DOI: https://doi.org/10.1016/j.ijnonlinmec.2016.01.005. URL: http://www.sciencedirect.com/science/article/pii/S0020746216000068.

[76] Teunis van Manen, Shahram Janbaz, and Amir A Zadpoor. "Programming the shape-shifting of flat soft matter". In: *Materials Today* (2017).

[77] A. Lucantonio, P. Nardinocchi, and M. Pezzulla. "Swelling-induced and controlled curving in layered gel beams". In: *Proceedings of the Royal Society A: Mathematical, Physical and Engineering Science* 470.2171 (2014). DOI: 10.1098/rspa.2014.0467. eprint: http://rspa.royalsocietypublishing.org/content/470/2171/20140467.full.pdf+html.

[78] Paola Nardinocchi and Eric Puntel. "Unexpected hardening effects in bilayered gel beams". In: *Meccanica* 52.14 (2017), pp. 3471–3480.

[79] P Nardinocchi and E Puntel. "Swelling-induced wrinkling in layered gel beams". In: *Proc. R. Soc. A* 473.2207 (2017), p. 20170454.

[80] Paola Nardinocchi, Matteo Pezzulla, and Luciano Teresi. "Anisotropic swelling of thin gel sheets". In: *Soft Matter* 11 (8 2015), pp. 1492–1499. DOI: 10.1039/C4SM02485K. URL: http://dx.doi.org/10.1039/C4SM02485K.

[81] Douglas P Holmes et al. "Bending and twisting of soft materials by non-homogenous swelling". In: *Soft Matter* 7.11 (2011), pp. 5188–5193.

[82] Anupam Pandey and Douglas P. Holmes. "Swelling-induced deformations: a materials-defined transition from macroscale to microscale deformations". In: *Soft Matter* 9 (23 2013), pp. 5524–5528. DOI: 10.1039/C3SM00135K. URL: http://dx.doi.org/10.1039/C3SM00135K.

[83] Shahaf Armon et al. "Geometry and Mechanics in the Opening of Chiral Seed Pods". In: *Science* 333.6050 (2011), pp. 1726–1730. DOI: 10.1126/science.1203874. eprint: http://www.sciencemag.org/content/333/6050/1726.full.pdf. URL: http://www.sciencemag.org/content/333/6050/1726.abstract.

[84] Matteo Pezzulla et al. "Geometry and mechanics of thin growing bilayers". In: *Soft matter* 12.19 (2016), pp. 4435–4442.

[85] Michele Curatolo, Paola Nardinocchi, and Luciano Teresi. "Driving water cavitation in a hydrogel cavity". In: *Soft matter* 14.12 (2018), pp. 2310–2321.

[86] Alessandro Lucantonio, Giuseppe Tomassetti, and Antonio DeSimone. "Large-strain poroelastic plate theory for polymer gels with applications to swelling-induced morphing of composite plates". In: *Composites Part B: Engineering* 115 (2017), pp. 330–340.

[87] P Nardinocchi and E Puntel. "Finite bending solutions for layered gel beams". In: *International Journal of Solids and Structures* 90 (2016), pp. 228–235.

[88] Matteo Pezzulla et al. "Morphing of geometric composites via residual swelling". In: *Soft Matter* 11 (29 2015), pp. 5812–5820. DOI: 10.1039/C5SM00863H. URL: http://dx.doi.org/10.1039/C5SM00863H.

[89] Leonid Ionov. "Hydrogel-based actuators: possibilities and limitations". In: *Materials Today* 17.10 (2014), pp. 494–503.

[90] Parag R. Gogate and Aniruddha B. Pandit. "Engineering design methods for cavitation reactors II: Hydrodynamic cavitation". In: *AIChE Journal* 46.8 (2000), pp. 1641–1649. ISSN: 1547-5905. DOI: 10.1002/aic.690460815. URL: http://dx.doi.org/10.1002/aic.690460815.

[91] A. I. Nesterenko and Yu. S. Berlizov. "The possibility of cracking hydrocarbons with cavitation. A quantitative energy assessment". In: *Chemistry and Technology of Fuels and Oils* 43.6 (2007), pp. 515–518. ISSN: 1573-8310. DOI: 10.1007/s10553-007-0089-4. URL: https://doi.org/10.1007/s10553-007-0089-4.

[92] Jessica A Zimberlin et al. "Cavitation rheology for soft materials". In: *Soft Matter* 3.6 (2007), pp. 763–767.

[93] Santanu Kundu and Alfred J Crosby. "Cavitation and fracture behavior of polyacrylamide hydrogels". In: *Soft Matter* 5.20 (2009), pp. 3963–3968.

[94] Olivier Vincent et al. "Birth and Growth of Cavitation Bubbles within Water under Tension Confined in a Simple Synthetic Tree". In: *Phys. Rev. Lett.* 108 (18 2012), p. 184502. DOI: 10.1103/PhysRevLett.108.184502. URL: https://link.aps.org/doi/10.1103/PhysRevLett.108.184502.

[95] X. Noblin et al. "The Fern Sporangium: A Unique Catapult". In: *Science* 335.6074 (2012), pp. 1322–1322. ISSN: 0036-8075. DOI: 10.1126/science.1215985. eprint: http://science.sciencemag.org/content/335/6074/1322.full.pdf. URL: http://science.sciencemag.org/content/335/6074/1322.

[96] Aimée Sakes et al. "Shooting Mechanisms in Nature: A Systematic Review". In: *PLOS ONE* 11.7 (July 2016), pp. 1–46. DOI: 10.1371/journal.pone.0158277. URL: https://doi.org/10.1371/journal.pone.0158277.

[97] C. Llorens et al. "The fern cavitation catapult: mechanism and design principles". In: *Journal of The Royal Society Interface* 13.114 (2016). ISSN: 1742-5689. DOI: 10.1098/rsif.2015.0930. eprint: http://rsif.royalsocietypublishing.org/content/13/114/20150930.full.pdf.

[98] Thibault Bertrand et al. "Dynamics of Swelling and Drying in a Spherical Gel". In: *Phys. Rev. Applied* 6 (6 2016), p. 064010. DOI: 10.1103/PhysRevApplied.6.064010. URL: http://link.aps.org/doi/10.1103/PhysRevApplied.6.064010.

[99] A. Lucantonio, P. Nardinocchi, and H. A. Stone. "Swelling dynamics of a thin elastomeric sheet under uniaxial pre-stretch". In: *Journal of Applied Physics* 115.8, 083505 (2014), pp. –. DOI: http://dx.doi.org/10.1063/1.4866576. URL: http://scitation.aip.org/content/aip/journal/jap/115/8/10.1063/1.4866576.

[100] S. Biwa. "Cavitation in finite elasticity with surface energy effects". In: *International Journal of Non-Linear Mechanics* 41.9 (2006), pp. 1084 –1094. ISSN: 0020-7462. DOI: https://doi.org/10.1016/j.ijnonlinmec.2006.11.001. URL: http://www.sciencedirect.com/science/article/pii/S0020746206000990.

[101] John Ball. "Discontinuous equilibrium solutions and cavitation in nonlinear elasticity". In: *Philosophical Transactions of the Royal Society of London A: Mathematical, Physical and Engineering Sciences* 306.1496 (1982), pp. 557–611. ISSN: 0080-4614. DOI: 10.1098/rsta.1982.0095. eprint: http://rsta.royalsocietypublishing.org/content/306/1496/557.full.pdf.

[102] Fernando P Duda, Angela C Souza, and Eliot Fried. "A theory for species migration in a finitely strained solid with application to polymer network swelling". In: *Journal of the Mechanics and Physics of Solids* 58.4 (2010), pp. 515–529.

[103] Huiming Wang and Shengqiang Cai. "Drying-induced cavitation in a constrained hydrogel". In: *Soft Matter* 11 (6 2015), pp. 1058–1061. DOI: 10.1039/C4SM02652G. URL: http://dx.doi.org/10.1039/C4SM02652G.

[104] Huiming Wang and Shengqiang Cai. "Cavitation in a swollen elastomer constrained by a non-swellable shell". In: *Journal of Applied Physics* 117.15 (2015), p. 154901. DOI: 10.1063/1.4918278. eprint: http://dx.doi.org/10.1063/1.4918278. URL: http://dx.doi.org/10.1063/1.4918278.

[105] Shengqiang Cai et al. "Osmotic collapse of a void in an elastomer: breathing, buckling and creasing". In: *Soft Matter* 6 (22 2010), pp. 5770–5777. DOI: 10.1039/C0SM00451K. URL: http://dx.doi.org/10.1039/C0SM00451K.

[106] Michele Curatolo, Stefano Gabriele, and Luciano Teresi. "Swelling and growth: a constitutive framework for active solids". In: *Meccanica* 52.14 (2017), pp. 3443–3456.

[107] Maurice L Huggins. "Solutions of long chain compounds". In: *The Journal of chemical physics* 9.5 (1941), pp. 440–440.

[108] Paul J Flory. "Thermodynamics of high polymer solutions". In: *The Journal of chemical physics* 10.1 (1942), pp. 51–61.

[109] Masao Doi. *Introduction to polymer physics*. Oxford university press, 1996.

[110] Kenji Urayama and Toshikazu Takigawa. "Volume of polymer gels coupled to deformation". In: *Soft Matter* 8 (31 2012), pp. 8017–8029. DOI: 10.1039/C2SM25359C. URL: http://dx.doi.org/10.1039/C2SM25359C.

[111] Eran Sharon, Michael Marder, and Harry L Swinney. "Leaves, flowers and garbage bags: making waves". In: *American Scientist* 92.3 (2004), pp. 254–261.

[112] Marcelo A Dias, James A Hanna, and Christian D Santangelo. "Programmed buckling by controlled lateral swelling in a thin elastic sheet". In: *Physical Review E* 84.3 (2011), p. 036603.

[113] Myunghwan Byun, Christian D. Santangelo, and Ryan C. Hayward. "Swelling-driven rolling and anisotropic expansion of striped gel sheets". In: *Soft Matter* 9 (34 2013), pp. 8264–8273. DOI: 10.1039/C3SM50627D. URL: http://dx.doi.org/10.1039/C3SM50627D.

[114] Alessandro Lucantonio, Luciano Teresi, and Antonio DeSimone. "Continuum theory of swelling material surfaces with applications to thermo-responsive gel membranes and surface mass transport". In: *Journal of the Mechanics and Physics of Solids* 89 (2016), pp. 96–109.

[115] P. Nardinocchi, M. Pezzulla, and L. Teresi. "Steady and transient analysis of anisotropic swelling in fibered gels". In: *Journal of Applied Physics* 118.24, 244904 (2015). DOI: http://dx.doi.org/10.1063/1.4938737. URL: http://scitation.aip.org/content/aip/journal/jap/118/24/10.1063/1.4938737.

[116] P. Nardinocchi and L. Teresi. "Actuation performances of anisotropic gels". In: *Journal of Applied Physics* 120.21 (2016), p. 215107. DOI: 10.1063/1.4969046. eprint: http://dx.doi.org/10.1063/1.4969046. URL: http://dx.doi.org/10.1063/1.4969046.

[117] Edward K Rodriguez, Anne Hoger, and Andrew D McCulloch. "Stress-dependent finite growth in soft elastic tissues". In: *Journal of biomechanics* 27.4 (1994), pp. 455–467.

[118] Ekkehart Kröner. "Allgemeine kontinuumstheorie der versetzungen und eigenspannungen". In: *Archive for Rational Mechanics and Analysis* 4.1 (1959), p. 273.

[119] Erastus H Lee. "Elastic-plastic deformation at finite strains". In: *Journal of applied mechanics* 36.1 (1969), pp. 1–6.

[120] Antonio DiCarlo and Sara Quiligotti. "Growth and balance". In: *Mechanics Research Communications* 29.6 (2002), pp. 449–456.

[121] Larry A Taber and Daniel W Eggers. "Theoretical study of stress-modulated growth in the aorta". In: *Journal of theoretical biology* 180.4 (1996), pp. 343–357.

[122] Paola Nardinocchi and Luciano Teresi. "On the active response of soft living tissues". In: *Journal of Elasticity* 88.1 (2007), pp. 27–39.

[123] D Ambrosi and F Guana. "Stress-modulated growth". In: *Mathematics and mechanics of solids* 12.3 (2007), pp. 319–342.

[124] Efi Efrati et al. "Spontaneous buckling of elastic sheets with a prescribed non-Euclidean metric". In: *Physica D: Nonlinear Phenomena* 235.1-2 (2007), pp. 29–32.

[125] Eran Sharon and Efi Efrati. "The mechanics of non-Euclidean plates". In: *Soft Matter* 6.22 (2010), pp. 5693–5704.

[126] P Nardinocchi, L Teresi, and V Varano. "The elastic metric: a review of elasticity with large distortions". In: *International Journal of Non-Linear Mechanics* 56 (2013), pp. 34–42.

[127] Manuela Minozzi et al. "Growth-induced compatible strains". In: *Mathematics and Mechanics of Solids* 22.1 (2017), pp. 62–71.

[128] Gerard A Ateshian. "Mixture theory for modeling biological tissues: illustrations from articular cartilage". In: *Biomechanics: Trends in Modeling and Simulation*. Springer, 2017, pp. 1–51.

[129] Bernard D Coleman and Walter Noll. "The thermodynamics of elastic materials with heat conduction and viscosity". In: *Archive for rational mechanics and analysis* 13.1 (1963), pp. 167–178.